MODELING OF AN EVAPORATION-CONDENSATION TYPE AEROSOL GENERATOR FOR SYNTHESIS OF SEMICONDUCTOR NANOCRYSTALS

A THESIS SUBMITTED TO
THE GRADUATE SCHOOL OF NATURAL AND APPLIED SCIENCES
OF
MIDDLE EAST TECHNICAL UNIVERSITY

BY

ZEYNEP BIRCE REYHAN

IN PARTIAL FULFILLMENT OF THE REQUIREMENTS
FOR
THE DEGREE OF MASTER OF SCIENCE
IN
CHEMICAL ENGINEERING

APRIL 2024

Approval of the thesis:

MODELING OF AN EVAPORATION-CONDENSATION TYPE AEROSOL GENERATOR FOR SYNTHESIS OF SEMICONDUCTOR NANOCRYSTALS

submitted by **ZEYNEP BIRCE REYHAN** in partial fulfilment of the requirements for the degree of **Master of Science** i**n Chemical Engineering, Middle East Technical University** by,

Prof. Dr. Naci Emre Altun
Dean, Graduate School of **Natural and Applied Sciences** _____

Prof. Dr. Yusuf Uludağ
Head of the Department, **Chemical Engineering** _____

Assist. Prof. Dr. Necip Berker Üner
Supervisor, **Chemical Engineering, METU** _____

Examining Committee Members:

Prof. Dr. Yusuf Uludağ
Chemical Engineering, METU _____

Assist. Prof. Dr. Necip Berker Üner
Chemical Engineering, METU _____

Assoc. Prof. Dr. Emre Büküşoğlu
Chemical Engineering, METU _____

Assoc. Prof. Dr. Harun Koku
Chemical Engineering, METU _____

Assoc. Prof. Dr. Barbaros Çetin
Mechanical Engineering, Bilkent University _____

Date: 22.04.2024

I hereby declare that all information in this document has been obtained and presented in accordance with academic rules and ethical conduct. I also declare that, as required by these rules and conduct, I have fully cited and referenced all material and results that are not original to this work.

Name Last name: Zeynep Birce Reyhan

Signature:

ABSTRACT

MODELING OF AN EVAPORATION-CONDENSATION TYPE AEROSOL GENERATOR FOR SYNTHESIS OF SEMICONDUCTOR NANOCRYSTALS

Reyhan, Zeynep Birce
Master of Science, Chemical Engineering
Supervisor: Assist. Prof. Dr. Necip Berker Üner

April 2024, 107 pages

III-V semiconductors are one of the most capable class of materials for optoelectronic and photonic applications due to their air-stability and tunability with direct bandgaps spanning between 0.35 and 6 eV. Gas-phase routes constitute a viable pathway for producing III-V nanocrystals. In gas phase, these crystals can be made to be ligand-free, which is crucial for electronic applications. However, most gas-phase routes require vapor-phase precursors, which are very expensive, highly toxic, and pyrophoric. A straightforward way of producing the required elemental precursors involves using an evaporation-condensation generator (ECG), which is usually in the form of a tubular furnace. There is a need for an ECG that can provide a stable aerosol output with high mass yield. In this study, mathematical modeling and simulations of an ECG was done with the incorporation of momentum, heat, and mass transport, along with aerosol dynamics. Antimony, an important constituent of various III-V compounds, was taken as the test material. Following the experimental results on an ECG configuration that was demonstrated to work at reduced pressure, an ECG was simulated to operate at 6 Torr with varying gas flow rates using computational fluid dynamics (CFD). After the model for simulating the transport phenomena was completed, a comprehensive aerosol dynamics model was derived, and important elements of the aerosol model was incorporated in CFD analysis. Results obtained for the mass flow rate of the aerosol and the yield of the generator were compared with experimental results, indicating order-of-magnitude agreement.

ÖZ

YARI İLETKEN NANOKRİSTALLERİN SENTEZİ İÇİN BUHARLAŞMA-YOĞUŞMA TİPİ AEROSOL JENERATÖRÜNÜN MODELLENMESİ

Reyhan, Zeynep Birce
Yüksek Lisans, Kimya Mühendisliği
Tez Yöneticisi: Dr. Öğr. Üyesi Necip Berker Üner

Nisan 2024, 107 sayfa

III-V yarı iletken malzemeler hava stabiliteleri ve 0.35 ile 6 eV ayarlanabilir bant aralıkları sayesinde optoelektronik ve fotonik uygulamalar için elverişli malzemelerdir. Bu malzemelerin nanokristal olarak üretilmesinde gaz fazında sentez alternatif bir yöntem olarak kullanılmaktadır. Gaz fazında sentez bu nanokristaller elektronik uygulamalarda istenmeyen ligandlar olmadan üretilebilir. Ancak çoğu gaz fazında sentez metodu buhar fazında öncüler gerektirir ve bunlar pahalı, yüksek toksisiteye sahip ve piroforik kimyasallardır. Bu kristallerin gaz fazında üretimi için en basit yöntem tüp fırın şeklinde olan buharlaşma-yoğuşma jeneratörlerini (BYJ) kullanmaktır. Sabit kütlesel aerosol akışına ve yüksek verime sahip BYJ'ye ihtiyaç vardır. Bu projede BYJ için tüm taşınım olayları ve aerosol dinamiği matematiksel olarak modellenip ve simüle edilmiştir. Çeşitli III-V bileşiklerinin önemli bir parçası olan Antimon elementi bu sistem için test materyali olarak kullanılmıştır. Deneysel verilerle kanıtlanmış, atmosferik basınçta çalışan yüksek verimli BYJ sistemini baz alarak düşük basınçta (6 Torr) ve farklı gaz akış hızlarında çalışacak bir BYJ bilgisayar destekli akışkanlar mekaniği kullanarak simüle edilmiştir. Matematiksel model tamamlandıktan sonra sistem tüm taşınım olayları, yüzey büyümesi ve yoğuşma mekanizmaları için simüle edilmiştir. Aerosol kütlesel akış hızı ve jeneratör verimi deneysel sonuçlar ile karşılaştırılmış olup, mertebe bazında uyum göstermiştir.

Scientia Dux Vitae Certissimus

ACKNOWLEDGMENTS

In this three-year journey I have been supported by many through their never-ending support, patience and generosity for whenever I needed help with anything. Firstly, I would like to thank my thesis advisor Asst. Prof. Necip Berker Üner for his guidance, support and most importantly for his patience. His mentorship and expertise have been instrumental through this study, and I am so grateful to have taken this journey with him.

I would like to thank my friends who have been there for me whenever I needed them whether it was to let loose or actually sit down and work. I would like to thank especially to the following to express my gratitude; Öykü Somalı, Koray Tarakçı and Oğuzhan Coşğun for all their love and support, their friendship means the world to me. I would also like to thank Assoc. Prof. Dr. Güneş Kibar for her personal support and love, without her encouragement and support it would have been a lot harder to finish this thesis.

I am deeply grateful to İlkin Kürkçüoğlu for entering my life and assuming the role of my godmother, especially during times when my family is distant. My appreciation knows no bounds for the precious moments shared with both İlkin Kürkçüoğlu and Şenol Kürkçüoğlu. Every moment spent together, even in simple conversation, has been enriching, and I am profoundly thankful for the privilege of knowing you both.

Most importantly, my family. I am eternally thankful for my mother, Hale Tamer Ulla for her unwavering love, sacrifices, unconditional support, and guidance me. Her resilience, unconditional love and wisdom shaped the person I am today. I dedicate this thesis to her with my deepest appreciation and love. My aunt, Handan Tamer, is the reason that I walked the academic path, and I am so thankful that she pushed me in this direction when I was a child. My grandmother, Sevim Tamer; there are no words to express my gratitude for the love and support you've given me sacrifices you made for me. My step-father, Azmat Ulla, I am grateful for all the

support you’ve given me throughout the years, starting from way back when you first helped me with my physics work in high school. Finally, my beloved pets; Mocha and Loki. Their presence has been a constant source of comfort and solace during long hours of study and research. Their unconditional affection and playful spirits have brightened even the darkest of days, reminding me to take breaks and enjoy the simple pleasures in life. I am endlessly thankful for their silent support and unwavering loyalty, which have brought warmth and light to my journey.

This work is funded by ODTÜ BAP, the project ID: 11095

TABLE OF CONTENTS

ABSTRACT v

ÖZ vi

ACKNOWLEDGMENTS viii

TABLE OF CONTENTS x

LIST OF TABLES xiii

LIST OF FIGURES xiv

CHAPTERS

1. INTRODUCTION 1

1.1 Semiconductor Nanocrystals 2

1.2 SNC Production Methodologies 4

1.2.1 Liquid Phase Synthesis 4

1.2.2 Gas Phase Synthesis 5

1.3 Aerosol Synthesis 7

1.3.1 Limitations of ECGs 9

1.4 Scope of the Thesis 13

2. COMPUTATIONAL PROCEDURE AND THE DEVELOPMENT OF THE AEROSOL MODEL 15

2.1 Model Geometries in COMSOL 16

2.2 Material Equations and Parameters 18

2.2.1 Argon 18

2.2.2 Antimony 19

2.2.3 Fused Silica Parameters 22

2.3 Simulation Details 23
2.3.1 Structural and Operational Parameters 23
2.3.2 Equations of Momentum Transport 24
2.3.3 Equations of Heat Transfer in Solids and Fluids 27
2.3.4 Equations of Mass Transfer 31
2.4 Solution of Multiphysics Equations 33
3. VAPOR TRANSPORT 37
3.1 Momentum Transfer 37
3.2 Heat Transfer 42
3.3 Vapor transport 46
3.4 Artificial Nucleation 50
4. AEROSOL DYNAMICS 57
4.1 General Dynamics Equation 57
4.2 Lognormal Model of GDE 59
4.2.1 Advection Term 61
4.2.2 Surface Growth Term 62
4.2.3 Diffusion Term 64
4.2.4 Coagulation Term 68
4.2.5 Thermophoresis Term 69
4.2.6 Hatch-Choate Equations 70
4.2.7 GDE in Moment Form 71
4.2.8 Implementation of Aerosol Model into COMSOL 73
5. CONCLUSIONS AND FUTURE WORK 79
6. REFERENCES 81

APPENDICES

A. Combustion Boat Photos 89

B. Analysis of the Entrance Region 91

C. On Predicting the Transport Properties of Antimony Vapor 95

D. Photos of a Quartz Tube Used in a Furnace-Type ECG 97

E. Use of Step Functions in Modeling Conditional and Transitional Processes . 99

F. Boundary Conditions for Transport Equations 103

G. Mesh Independence and the Numerical Conservation of Mass 105

H. Reducing the Particle Diffusion Coefficient to Power-Law Form..... 107

LIST OF TABLES

TABLES

Table 2.1. Physical constants of argon 19

Table 2.2. Physical properties and constants of antimony 20

Table 2.3. Equations describing the vapor pressure of solid antimony 20

Table 2.4. Physical constants of fused silica 22

Table 2.5. Structural parameters of the furnace and the combustion boat 23

Table 2.6. Operational parameters of the system 24

Table 3.1. Mass flow rates and yield of Sb vapor for two argon flow rates 49

Table 3.2. Mass flow rates and yield for two argon flow rates of Sb with a diffusion transition size of 50 mm 55

Table 4.1. Coefficients for Equation 4.72 where there is only surface growth ... 74

Table 4.2. Coefficients for Equation 4.72 for surface growth and condensation 74

Table B1. Boundary conditions for the inlet system 92

Table F1. Boundary conditions for momentum, heat and mass transport 104

Table G1. Mesh independence and mass conservation data for 500 sccm flow of Ar for vapor 105

LIST OF FIGURES

FIGURES

Figure 1.1: Number of articles on semiconductor nanocrystals past year 2000 [7] 1

Figure 1.2: Transmission electron microscope images of CdTe quantum dots [10] 3

Figure 1.3: Energy bands in bulk semiconductors and quantum dots 4

Figure 1.4: Working principle of an ECG 8

Figure 1.5: Simplified versions of the designs proposed by Singh et al 10

Figure 1.6: Simplified schematic of the design proposed by Wegner et al 10

Figure 1.7: Change in aerosol mass flow as a function of time in a tubular furnace ECG 12

Figure 2.1. 3D schematic of the model domain 16

Figure 2.2. 2D schematic of the model domain 17

Figure 2.3. Vapor pressure of antimony predicted by the equations listed in Table 2.3 21

Figure 2.4. Boundaries for fluid flow 26

Figure 2.5. Temperature profile example of a tubular furnace used as an ECG [76] 29

Figure 2.6. Boundaries for heat transport 31

Figure 2.7. Boundaries for mass transport 32

Figure 2.8. Adaptive triangular mesh in the system 34

Figure 2.9. Physics coupling in the simulation 35

Figure 3.1. Flow map in the ECG 38

Figure 3.2. Effect of Sb amount in the boat to gas flow 39

Figure 3.3. Velocity profiles in the vertical plane 40

Figure 3.4. Velocity profiles in the horizontal plane 41

Figure 3.5. Variation of convective heat transfer coefficient around the outlet tube for 200 and 500 sccm flow 43

Figure 3.6. Ratio of radiative flux to convective flux at the outlet tube for 200 and 500 sccm flow 44

Figure 3.7. Temperature profile on the outlet tube for 500 sccm flow 44

Figure 3.8. Temperature flow map in the ECG for 500 sccm flow 45

Figure 3.9. Concentration distribution map of Sb vapor under 200 and 500 sccm flow rate 47

Figure 3.10. Sb vapor concentration averaged over the y-dimension as a function of flow rate 48

Figure 3.11. Transition from vapor diffusion to particle diffusion under 500 sccm flow at the central axis, plotted as a function of the transition zone width, X 52

Figure 3.12. $\frac{u}{D}$map of the system with the transition size of 50 mm 53

Figure 3.13. Concentration distribution of Sb with the transition size of 50 mm 54

Figure 4.1. Boundaries for stabilized diffusion coefficient equation 75

Figure 4.2. Saturation ratio and nucleation rate distribution maps for 500 sccm flow rate 77

Figure 4.3. Flow maps of M_0 and M_1 for 500 sccm flow rate 78

Figure A1. Combustion boat filled with Sb before and after the operation. 89

Figure B1. Flow map in the entrance region 92

Figure B2. Temperature field in the entrance region. 93

Figure D1. Part of the quartz tube located in the furnace of an ECG [62] 97

Figure D2. Outlet of the quartz tube located in an ECG [62] 98

Figure E1. Unit step function. 99

Figure E2. Unit Heaviside step functions. 100

Figure F1. Boundaries of the system 103

CHAPTER 1

INTRODUCTION

Synthesis of nanometer-sized CdS crystallites as a colloid by the Brus team in 1983 paved way for a new class of materials [1]. The size-dependent optoelectronic properties of CdS resulted in the development of II-VI semiconductor nanocrystals (SNC), colloquially called quantum dots. Due to quantum confinement and the resulting shift from bulk to molecular properties, SNCs have adjustable optoelectronic properties, which eventually resulted in many applications spanning from lighting, displays, solar cells, and biological imaging agents [2-5]. This technological development was the product of an intense research effort, as visualized in Figure 1.1. The birth of SNCs are accepted to have planted the seeds on nanoscience and early efforts in the field were rewarded with the Nobel Prize in Chemistry in 2023 [6].

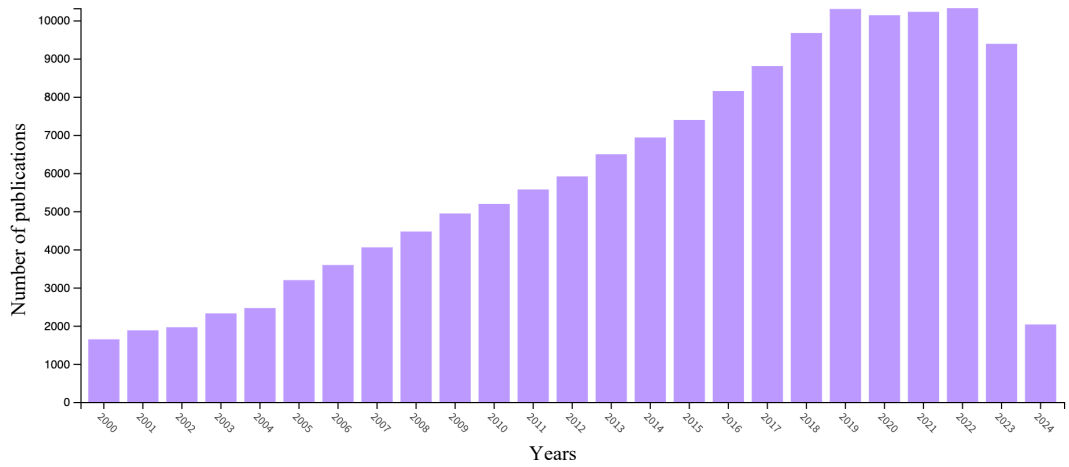

Figure 1.1: Number of articles on semiconductor nanocrystals past year 2000 [7]. Taken from Scopus database.

SNCs are divided mainly into types II-IV, III-V, and IV-VI based on the groups of the constituent elements. For different types, synthesis procedures vary,

and for some III-V SNCs, established methods of synthesis are not yet present. As this work focuses on the development of a synthesis tool for the gas phase SNC synthesis, existing production methodologies for SNCs will be presented below, but first, SNCs and their properties will be slightly more elaborated.

1.1 Semiconductor Nanocrystals

Semiconductor nanocrystals are particles that exhibit size dependent optoelectronic properties. They are usually within the size range of 1 to 100 nanometers and are considered as the transition materials between small molecules and large crystals [8]. Due to the presence of a band structure for electrons, the properties of SNCs fall between those of insulators and conductors, just like that of a bulk semiconductor. However, at very small crystal sizes, the quantum confinement effect is observed, which creates a diversion from bulk semiconductor properties. The quantum confinement theory is based on the electron-hole pairs, called excitons, in which the electron and the hole are separated by a fundamental distance called the exciton Bohr radius, which depends on the parameters of the bulk crystal structure [9]. When the radius of a crystallite is close to exciton Bohr radius, the band structure is perturbed, leading to a change in the band gap [9]. For SNCs of type II-VI, III-V and IV-VI with direct bandgaps, this means that as long as the particle size is on the order of the Bohr radius, changing size would yield a different band structure, therefore a different band gap, and subsequently different optoelectronic properties, resulting in the utilization of these materials in multiple application areas [9]. For II-VI SNCs, desired particle sizes are usually less than 10 nm. An example of II-VI SNCs is shown in Figure 1.2.

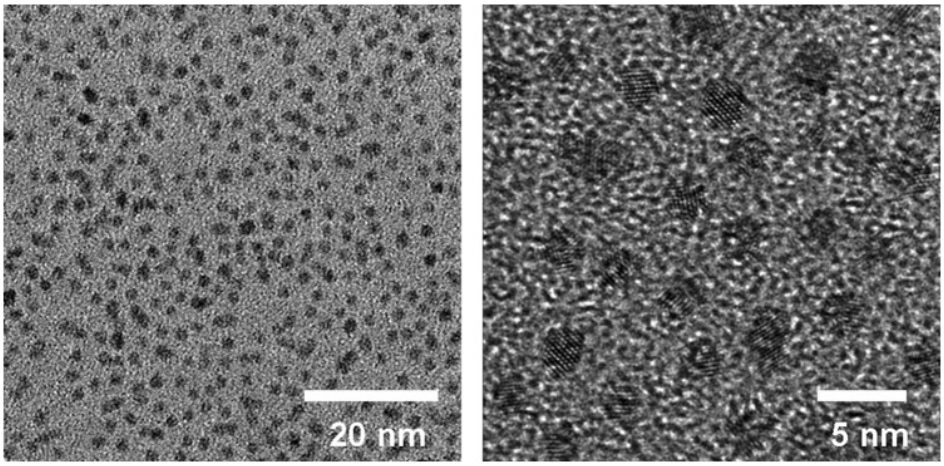

Figure 1.2: Transmission electron microscope images of CdTe quantum dots [10]. The quantum dots shown here are produced by a colloidal route (*vide infra*).

The size of the crystal and the band gap are inversely proportional to each other. As pictured in Figure 1.3, the band gap is smaller in a large SNC compared to a small SNC, and it usually increases approximately linearly down to 1 nm. Therefore, upon a direct electronic transition from the conductance band to valence band, the energy is emitted as light, and the light emitted from a larger SNC is of lower energy and correspondingly, has longer wavelength. This property makes SNCs useful in light-emitting diodes (LEDs) and other light sources, where a broad emission spectrum can be extracted from the colloidal ensemble of a single material, but with different sizes. The tunability of light emission makes SNCs valuable in other color specific applications such as displays, biological imaging and tracking [4, 11]. Another important aspect to consider is the surface area-to-volume ratio of SNCs. For SNCs, this ratio is very high (ranging from 10^8 to 6×10^{10} for particles between 1 and 100 nm respectively) and, therefore they are seen as promising for photocatalytic applications [12-14].

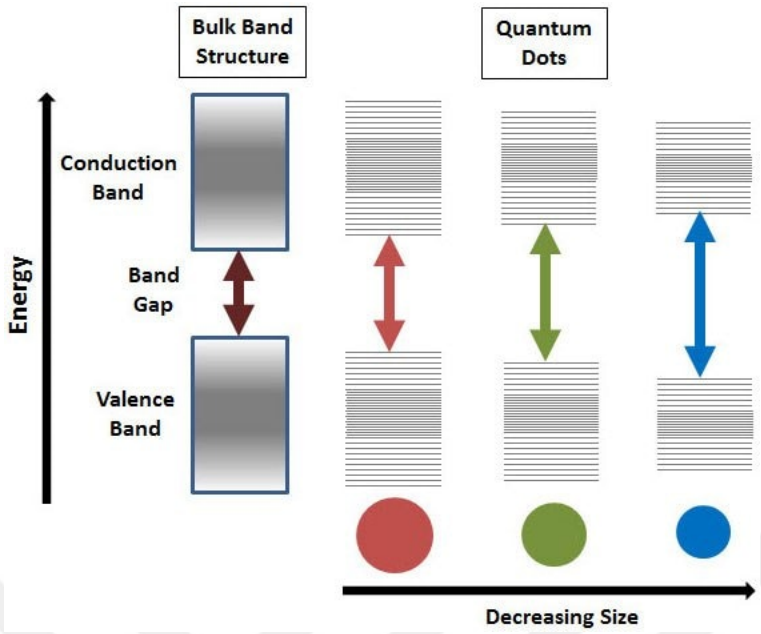

Figure 1.3: Energy bands in bulk semiconductors and quantum dots. Reprinted from [15]

1.2 SNC Production Methodologies

The importance of small size and size control requires deliberate synthesis methods for the production of SNCs. These methods are classified into two according to the medium in which they are formed: liquid and gas phase synthesis. Some of the major approaches related to these methods are briefly summarized below, along with their advantages and disadvantages.

1.2.1 Liquid Phase Synthesis

Colloidal synthesis involves dissolution of the precursors, which are metal salts or organometallic compounds, in a solvent and then manipulating the system either physically or chemically to produce the SNCs [16, 17]. This method is most prominent for its ability to produce highly monodisperse SNCs of groups II-IV and IV-VI with controllable size and shapes. A popular example for the colloidal production is the colloidal heat-up method that is most commonly used to produce

the CdTe and similar II-VI SNCs [18]. In this method a Cd salt and a thiol, which acts as a stabilizer, are added to the flask and the pH of the system is altered via drop-wise addition of NaOH. Then, H_2Te gas, which is extremely toxic, is bubbled through the flask and the system is heated up to 100 ℃ with continuous stirring. The SNCs start to form as soon as the H_2Te is introduced to the system [18].

Another widely employed colloidal method that does not include gaseous reagents is the hot injection method. A solution containing the precursor elements, called a precursor solution, is added to a reaction mixture maintained at a high temperature. The precursors react rapidly to form the SNCs which then grow as the system cools [19].

The advantages of liquid phase synthesis are easy control of the size and shapes of the nanoparticles under low temperature conditions, relatively short operation times, high yield, highly accessible equipment and reagents, adjustable surface functionality of the nanoparticles, and control over their physical properties [10, 20]. On the other hand, liquid phase synthesis has some disadvantages as well. The industrial applicability of the liquid phase synthesis is limited due to their low productivity. Moreover, the final product is wet and it contains organic ligands, which are undesirable in electronic applications [21, 22].

1.2.2 Gas Phase Synthesis

This synthesis route involves formation of a solid material from a gaseous phase and subsequent deposition or collection. Generally, synthesis is achieved through either a form of physical vapor deposition (PVD) or chemical vapor deposition (CVD). In PVD, solid metal is vaporized and condensed onto a substrate, and in CVD, solid material is formed via reaction in the gas phase [23]. Generic PVD or CVD systems are usually designed for the synthesis of films, therefore, these systems require modification. An example for such a PVD process is laser ablation. In this method, the decomposition of a solid precursor occurs by photochemical

processes, evaporation or pyrolysis when a laser beam is applied [24]. The advantage of this process is that it can produce highly crystalline materials from metal or metal oxide precursors, even for high refractory materials. However, the high concentration of small clusters produced via this process leads to agglomerates, resulting in larger particles and a wide size distribution, which are undesired, and the process has low yield and high operational costs due to requirement of a high-vacuum chamber and a powerful laser [25, 26].

An example to a CVD-like process is the vapor precursor-based synthesis. This method utilizes vapor- or sometimes gas-phase precursors of desired metals, such as pnictides or metalorganic compounds. First, homogenous nucleation is induced either by high temperature, e.g. flame or a tube furnace [27], or by introducing reactive species, such as free electrons in a plasma [28], and thus in-flight particle growth can be sustained continuously. This method has high production rates, however, it usually suffers from the production of highly polydisperse agglomerates [29]. Plasmas can approach the size control provided by colloidal methods with narrow distributions [30], however, specific gas phase precursors are required. Although many precursors that can enable high-purity materials are available [31], most of these compounds are either pyrophoric and/or toxic [21]. For example, III-V stibnide SNCs are compound semiconductors that involve antimony from group V. One of the most prominent materials of the class, gallium antimonide (GaSb), can be used in short-wave infrared range detectors [32], thermophotovoltaic and solar cells [33], single-hole transistors [34]. The gas phase precursor of Sb for making GaSb SNCs is antimony trihydride (SbH_3), commonly known as stibine [35], which is a pnictogen hydride. It is an extremely flammable gas that will disperse in the air and react with air readily, and it has a very high toxicity with a recommended maximum exposure limit of 0.1 ppm as determined by US National Institute for Occupational Safety and Health [36]. An alternative type of precursor that provides very high purity and removes the dangers of using toxic precursors is the elemental aerosol. If the aerosol of the desired element can be

generated, some reactors, such as plasma, can utilize this type of a precursor to make SNCs [37- 39] .

1.3 Aerosol Synthesis

Utilization of an aerosol precursor requires continuous and stable generation of the desired aerosol with desired flow rate and particle size. There are two major methods of producing aerosols, i) nebulizers and sprays, ii) evaporation-condensation generators.

Nebulization or pneumatic atomization can be used to create aerosols by utilizing pressurized carrier gas and a particle suspension [40, 41]. The nebulizer is essentially a nozzle in which a carrier gas is flown through an orifice, which has a side arm inlet downstream. This arm is connected to the reservoir that contains the particle suspension. Downstream of the orifice, vacuum is created, and solution is drawn from the reservoir where it meets with the jet of the carrier gas. At this gas-liquid mixing region, the suspension is broken into small droplets, which are then carried with the gas, forming the aerosol. In general, polydisperse aerosols with particle size ranging from 1-10 μm is created [42].

If dry powders of the desired aerosolized material are available, nebulizers can produce aerosols from most colloid solutions in simple fashion. However, the large sizes produced and the polydispersity of the aerosol may require size separation, such as a cascade impactor, so that a narrower particle size range can be extracted. Such a strategy decreases the mass throughput. Another important problem with the utilization of nebulizers is that the output is wet, and it needs to be dried, which creates problems in aerosol purity. Solvents that come out of such an aerosol source are usually tolerated in spray pyrolysis, where a spray nozzle provides high-throughput aerosol supply [27]. However, the presence of the solvents generally limit the class of materials that can be synthesized to oxides only [43, 44].

A dry alternative to nebulizers and sprays is the evaporation-condensation generator (ECG). The general working principle of ECGs involve the evaporation of high-purity solid or liquid material via heating, and then cooling to form the particles [45]. A simple schematic of the working principle and the mechanisms involved in the particle production by ECGs are shown in Figure 1.4.

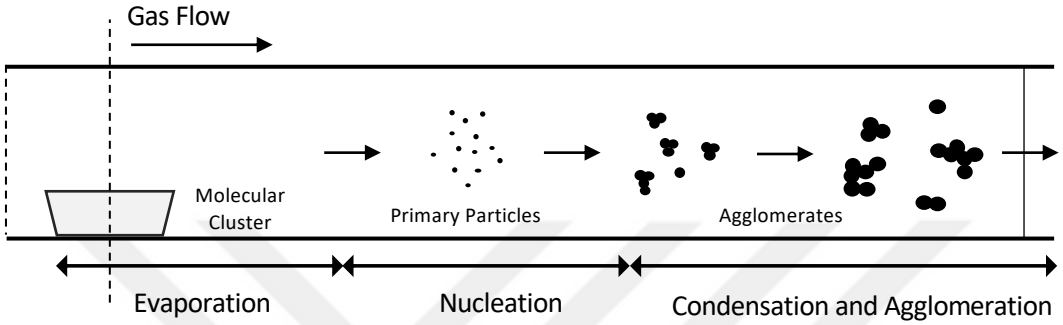

Figure 1.4: Working principle of an ECG. Adapted from [46].

The solid or the liquid with sufficiently high volatility is placed in a refractory and inert container and then it is evaporated. After evaporation, molecular clusters are formed due to kinetic equilibrium [47] and with the subsequent cooling of the system, growth is favored. Once the primary particles reach a critical nucleus size, nucleation is accepted to have occurred due to the production of stable primary particles [48]. Further growth is then caused by condensation, which can be assisted by agglomeration as well [47]. Condensation refers to vapor molecules depositing on the primary particles and agglomeration refers to particles sticking to each other upon collisions, forming larger particles. These agglomerates can sinter to some extent and spheroidal particles can be produced, akin to a coagulation process in colloids [47]. The overall process is named homogenous nucleation and the homogeneity refers to the fact that the solid particle formation occurs from the supersaturated vapor without the presence of another substrate [49]. ECGs are used in various areas such as drug delivery, catalysis, and nanoparticle synthesis [50, 51]. These generators are simple to build and they are flexible since aerosols of different materials, concentrations and particle sizes can be obtained [52].

1.3.1 Limitations of ECGs

Although the operation of an ECG is simple, this type of generators has a few disadvantages that limit their performance, especially when used for SNC synthesis. These can be listed as i) low mass yield, ii) time varying output and iii) long start-up and shut-down times

1.3.1.1 Low Yield

The most important problem that needs to be taken into consideration in ECGs is the low-yield problem. During particle formation, a large part of the vapor and some of the particle's deposit on the walls of the generator through diffusion, reducing the mass throughput. The ratio of this throughput to the amount of mass evaporated in the generator, is mass yield, and values are generally low, on the order of 10% or lower [37, 52]. This creates a problem in using high-purity elements, such as indium and silver. To solve this problem, ECGs with modified feed flow configurations have been developed in literature.

Two prominent experimental studies in the literature to improve the yield are conducted by Singh et. al [52] and Wegner et al. [37]. The simplified schematics of these studies are illustrated in Figure 1.5 and Figure 1.6 respectively. In both studies, the introduction of additional flow inlets was admitted into and ECG with the aim of reducing the residence times during particle formation and to narrow the residence time distribution, so that uniform particles with high yield can be synthesized. Increasing local flow velocities were therefore employed to reduce the diffusion time.

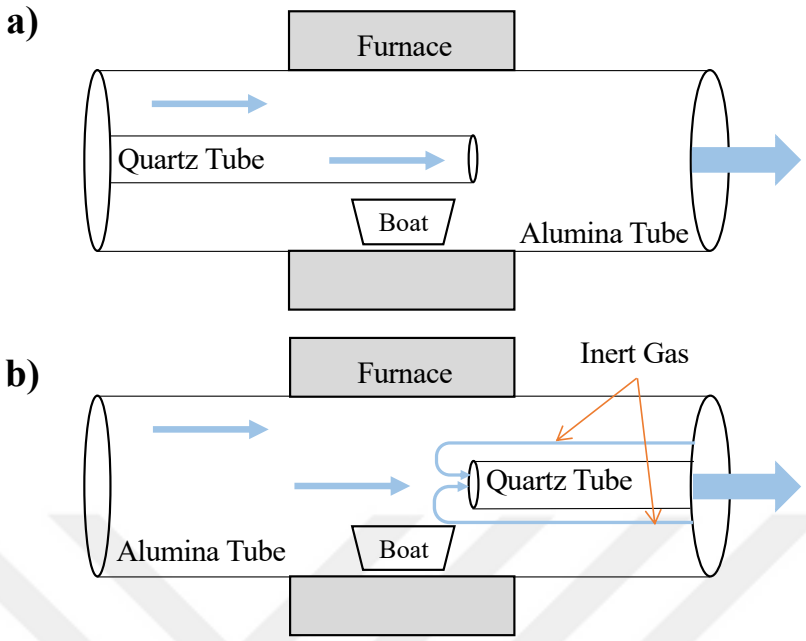

Figure 1.5: Simplified versions of the designs proposed by Singh et al. [52]. a) Quartz tube after the boat design b) Quartz tube as outlet design. Blue arrows indicate the flow of the carrier gas for both cases.

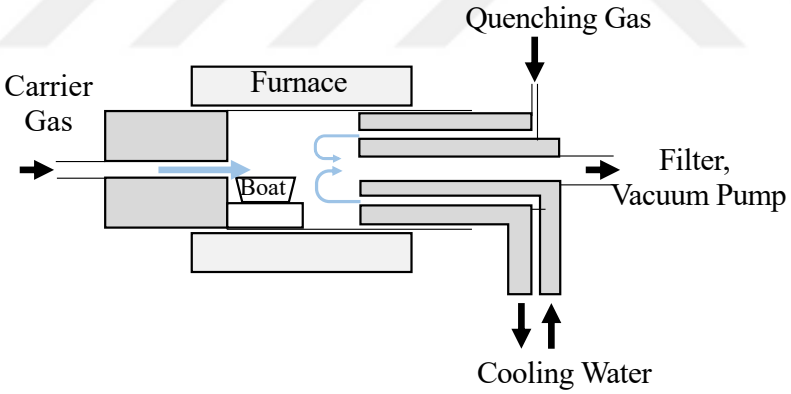

Figure 1.6: Simplified schematic of the design proposed by Wegner et al. [53]. Large blue arrow indicates the flow of the carrier gas and the curved blue lines indicate the flow of the quenching gas.

Both of the aforementioned studies are experimental and case specific. Singh et al evaporated indium and Wegener et al evaporated bismuth, and the applicability of their results for different materials and for different operational conditions is not apparent. This specificity can also be observed from commercially available

generators. For example, the GRIMM 7860 is an ECG that only works for evaporating tungsten oxide [54], whereas the TSI 3475 can only generate aerosols from waxes [55]. A broader market analysis also indicates that a generator that can generate aerosols of metals and semi-metals and is suitable for SNC synthesis is not available.

The homogenous nucleation process in ECGs has a large parameter space and involves multiple growth mechanisms. It was hypothesized that the parameter space and the design can be manipulated to improve the yield, mass flow rate, shape and size distribution, as demonstrated by Singh et al and Wegener et al [52, 53]. However, a general modeling framework that can predictively design a flexible generator with the desired performance characteristics is not yet available. In literature, several models have been developed to predict the results of this evaporation condensation process [56-59]. However, the problem with these models is that they do not account for all the physics taking place in the system. The aerosol dynamics in the system includes advection, condensation, diffusion, coagulation, and thermophoresis.

In a laminar flow reactor, Pratsinis and Kim studied aerosol dynamics due to coagulation and wall losses due to diffusion and thermophoresis, but nucleation and condensation were omitted [57]. Panda and Pratsinis modeled nucleation, condensation and coagulation, but neglected the wall losses and diffusive terms [58]. Kalani and Christofides studied nucleation and coagulation, but wall losses, diffusion and condensation was not included [56]. Terry et al. has modeled nucleation and diffusion without wall losses, coagulation and condensation [59]. It appears that in literature, the transport phenomena of an ECG along with the aerosol dynamics (i.e. particle formation mechanisms embedded in the mass transport) has not been simultaneously modeled, and it is not clear which mechanisms play a role in the low yields observed in experiments.

1.3.1.2 Time Varying Output

The aerosol mass flow rate in the ECGs tend to decrease with time which is due to the fact that as the amount of evaporating material decreases in the boat, the mass transfer resistance increases and the net evaporation flux decreases. Consequently, the mass output decreases with time. In Figure 1.7, mass flow measurements for a tubular furnace that acted as an ECG are shown. The tubular furnace produced an antimony aerosol, but due to the dynamics described above, a net decrease in aerosol mass flow rate was observed over the course of 20 minutes [37]. Such a trend is problematic for SNC synthesis since a shift in precursor supply rate would change the stoichiometry of the produced material as well.

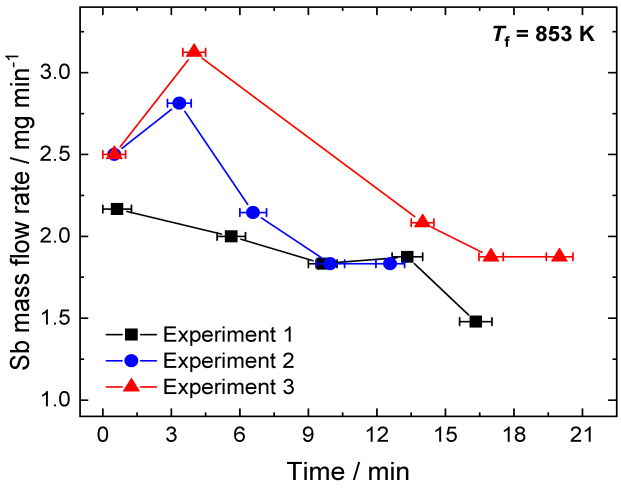

Figure 1.7: Change in aerosol mass flow as a function of time in a tubular furnace ECG. Aerosol was elemental antimony and the temperature of the furnace, T_f, was equal to 850 K [37].

The time variance of the mass output can be overcome by temperature programming of the ECG. Increasing temperature would increase vapor pressure, which would consequently increase the evaporation flux, hence the total mass output. However, to develop a general temperature program for an ECG, physics of the system must be studied in detail. Mathematical modeling is ideal to elucidate the

functional dependencies related to the time-varying output and the development of a general temperature ramp.

1.3.1.3 Long Heating and Cooling Times

Custom built ECGs are usually tube furnaces. These furnaces take long times to heat up and cool down due to their size and the materials used within. The boat that holds the evaporation source can be filled again only when the system fully cools down to room temperature to avoid air exposure and potential oxidation, which results in long waiting times before and after synthesis. The long heat-up and cool-down periods are due to the thermal mass of the insulating materials in tube furnaces. Such furnaces are heated by heating elements embedded in refractory bricks, which are made to locally arrest the heat due to low thermal diffusivities. Therefore, large furnaces are inconvenient, and smaller furnace sizes which are usually not commercially available would be preferred. However, the size of the generator should still be large enough to provide adequate evaporation surface and temperature uniformity. Therefore, the size of the generator is an important parameter for practical and efficient ECG operation.

1.4 Scope of the Thesis

For gas-phase synthesis of SNCs, aerosol precursors can provide a sustainable route with high purity in the synthesized material. For synthesis, the evaporation-condensation generator (ECG) is favorable for its dry output and suitability for low-vapor pressure precursors. However, the design and operation procedures of a high-yield ECG that has stable output, short start-up times and extensive material compatibility are lacking in literature. This thesis aims to develop a preliminary modeling framework that can elucidate the transport phenomena and the resulting aerosol dynamics that occurs in such a generator. With the framework, gas sweeping methods to improve yield can be designed. In addition, temperature

programming of the generator for a steady-output operation can be computationally established. Furthermore, analysis of the temperature gradients in the generator would allow shrinking the size of the generator, which would consequently reduce start-up times.

In this study, a low-pressure ECG, which was configured akin to a tube furnace, was computationally investigated. The reason for conducting a study at low pressure stems from two reasons. First, aerosol precursors are exceptionally suitable for low-pressure plasma reactors since these aerosols vaporize in the plasma and create a highly supersaturated vapor [60], which is highly reactive and can be used to make SNCs [37-39] or films composed of SNCs [61]. Second, experimental results and observation for the operation of such an ECG during synthesis of GaSb SNCs is available [37, 62].

The ECG was studied by computational fluid dynamics (CFD) through the use of COMSOL Multiphysics® version 5.6. In Chapter 2, model setup is explained in detail, where coupled fluid flow, heat transfer and mass transfer equations were developed for elemental Sb vaporizing and dispersing in the ECG. Chapter 3 summarizes the results of the calculations which yield the flow, temperature, and vapor concentration fields. Calculations were performed to include the effects of ambient cooling, temperature-dependent properties, and vapor losses due to deposition. To simulate the aerosol output, a general lognormal aerosol model was derived from the general dynamic equation in Chapter 4. Preliminary calculations were carried out by implementing the aerosol model into the transport phenomena framework and results were compared with the benchmark experiments reported in literature. Chapter 5 concludes the thesis and gives recommendations on future work.

CHAPTER 2

COMPUTATIONAL PROCEDURE AND THE DEVELOPMENT OF THE AEROSOL MODEL

The necessity for the development of a mathematical model that can predict the yield and mass flow rates of evaporation-condensation generators was outlined in the previous chapter. This chapter is dedicated to the development of a model that simulates fluid flow, heat transfer and mass transfer in an evaporation-condensation generator. In the following subchapters, the steps taken to set up the simulation of an existing experimental study are described.

The model is developed using COMSOL Multiphysics ® version 5.6, which is a commercial software for computational fluid dynamics (CFD). Total of three software modules; laminar flow, heat transfer in solids and fluids, and mass transfer in dilute systems are configured at steady-state. The materials employed in the system are, argon as the carrier gas, antimony as the metal to be vaporized, fused silica as the walls of a tube inserted into a furnace, and alumina as the combustion vessel. The model is a representation of an existing experimental study conducted by Uner & Thimsen in 2020 [37]. The dimensions of the generator and the experimental results of this study are available; therefore, the model was developed with the aims of replicating some of the experimental results. In other words, the work by Uner & Thimsen [37] is the benchmark of this modeling study and will be called as so in the remaining portion of this work.

2.1 Model Geometries in COMSOL

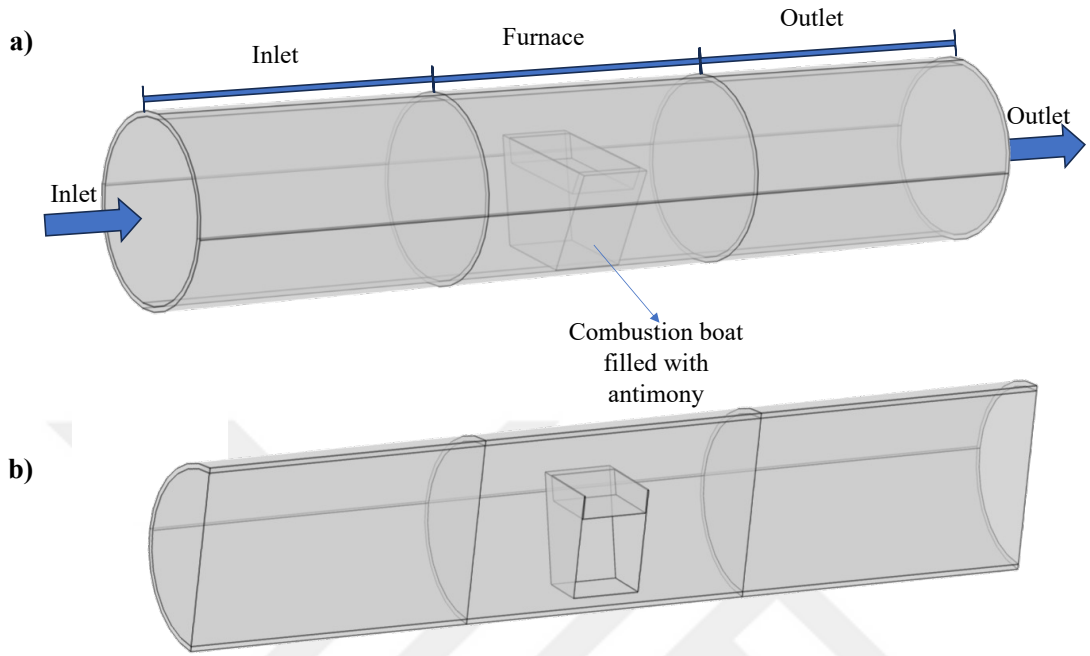

Figure 2.1. **3D schematic of the model domain.** For visual purposes, this geometry is scaled by factors of 1:10:10 for the *x*:*y*:*z* axes. a) Complete geometry of the system b) Cross section of the geometry at the center.

The geometry in Figure 2.1 depicts the actual geometry of the system closely. However, due to the computational expenses of simulating the generator in 3D, both time-wise and computational power-wise (mostly RAM requirements), the majority of modeling efforts were focused on the use of a 2-D geometry, which represents a slice taken out of the center of the 3-D geometry. The results of the simulations presented in this study was obtained by using a reduced 2-D geometry shown in Figure 2.2. It is important to note that the scaling on this geometry is solely for visual purposes. The model focuses on phenomena that occur inside the tubular geometry shown in 2.1 above. Due to the large aspect ratio, which can be inferred from the dimensions shown on Figure 2.2, the geometry is plotted in scaled fashion, so that the results can be presented with ease. This visualization strategy was followed throughout the entire study, but calculations were done on the actual dimensions.

It is important to mention that the side walls of the boat have been deliberately included in the calculations. These walls make meshing and convergence significantly more difficult, but their presence in the experiments creates a mass transfer resistance for the vapor on top of the Sb surface to get entrained in the flow, as will be shown in the next chapter. In practice, the boat can never be filled fully with Sb metal (see Appendix A), and therefore the amount of metal with respect to the total volume of the boat determine how larger of a mass transfer resistance there will be on top of the Sb surface. In the majority of the calculations, the inlet portion of the furnace, i.e. the section upstream of the furnace, was neglected to improve computational efficiency. It was seen that the entering gas heats up across a very short length in the furnace (approximately 15 cm, see Appendix B), and there was negligible axial back streaming of vapor. Therefore, the simulation domain was further reduced to the red box shown in Figure 2.2

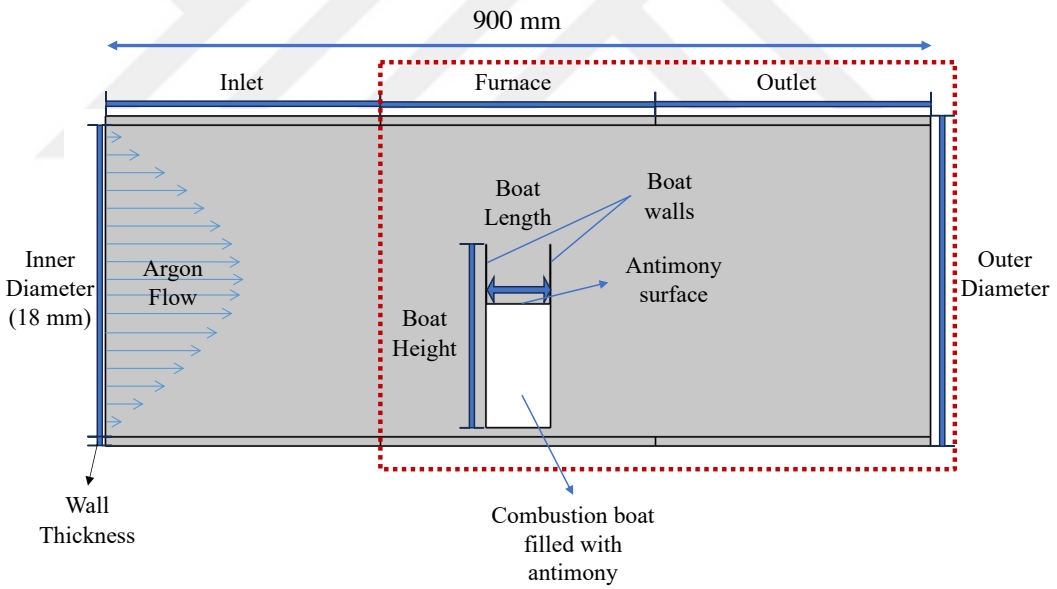

Figure 2.2. 2D schematic of the model domain. For visual purposes, this geometry is scaled by factors of 1:20 for the *x*:*y* axes. The majority of the calculations conducted in this work focused on the domains covered by the red box.

2.2 Material Equations and Parameters

As mentioned above, evaporation and aerosol formation of antimony in argon gas enclosed in a fused silica tube ECG is modeled in this study. Due to multiple physics involved in simulations, a fairly large database of material properties was required. Some properties of the materials were taken as constant, whereas some were expressed in the forms of equations and correlations. The relevant parameters and equations for argon, antimony and fused silica are detailed below.

2.2.1 Argon

Argon is the sole component of fluid dynamics in the generator. Dynamic viscosity, μ, of argon was estimated as a function of temperature using Sutherland's equation [63].

$$\frac{\mu}{\mu_0} = \left(\frac{T}{T_0}\right)^{\frac{3}{2}} \left(\frac{T_0 + S_\mu}{T + S_\mu}\right) \tag{2.1}$$

μ_0 and T_0 are reference values of the gas and the S_μ in this equation is called the Sutherland constant for viscosity, which depicts an effective temperature for the gas under consideration. For the argon, the values and the units of these constants are 2.125×10^{-5} N·s/m^2, 273 K and 144 K, respectively [63]. Based on kinetic theory, the description of the viscosity of a simple gas is very similar to that of thermal conductivity. Therefore, a similar Sutherland type equation can also be used to determine the thermal conductivity, k, for the argon as a function of temperature.

$$\frac{k}{k_0} = \left(\frac{T}{T_0}\right)^{\frac{3}{2}} \left(\frac{T_0 + S_k}{T + S_k}\right) \tag{2.2}$$

Similar to Equation 2.1, the k_0 and T_0 refer to the reference values and S_k refers to the Sutherland constant for thermal conductivity. For argon, the values and the units of these constants are 0.0163 W/m. K, 273 K and 170 K respectively.

The simulations involve temperature gradients. Considering that the system is operated at high temperatures and low molar pressures, argon can be satisfactorily described as an ideal gas. Therefore, the density and heat capacity under constant pressure is calculated according to the ideal gas laws [64].

$$\rho = \frac{pM_{Ar}}{RT} \tag{2.3}$$

$$c_p = \frac{5}{2}R \tag{2.4}$$

R is the ideal gas constant. Other data such as atomic data of argon which is used to calculate other parameters such as diffusion coefficient are given in the table below.

Table 2.1. Physical constants of argon

Physical Property	Value and Unit
Molar mass of argon	39.948×10^{-3} kg/mol
Atomic mass of argon	6.634×10^{-26} kg
Collision diameter of argon[1]	3.432×10^{-10} m [65]

2.2.2 Antimony

Solid antimony vaporizes in the simulations. As shown in Figure 2.2, solid Sb in the combustion boat is not a part of the simulation, but the vapor is carried by the argon flow, it disperses due to fast diffusion and is subjected to a temperature field. The important physical properties and constants of Sb are given in Table 2.2

[1] Lennard-Jones parameter; characteristic diameter of molecules.

Table 2.2. Physical properties and constants of antimony.

Physical Property	Value and Unit
Solid Sb density	6535 kg/m³ [66]
Liquid Sb density[2]	6492 kg/m³ [67]
Antimony melting temperature	904 K [66]
Sb molar weight	0.122 kg/mol [68]
Sb atomic weight	2.022×10^{-25} kg/atom
Sb atomic diameter	2.66×10^{-10} m [69]
Sb collision diameter	3.15×10^{-10} m [70]

In the ECG, solid antimony is vaporized at high temperature. The amount of antimony vapor in the system is therefore determined by the equilibrium vapor pressure of Sb. In literature, there are three different correlations in which the Sb vapor pressure can be determined. However, each of these correlations have their limitations. The equations and their suitable temperature range can be found in Table 2.3.

Table 2.3. Equations describing the vapor pressure of solid antimony. First two entries are experimental studies whereas the third is a recommended correlation without a definitive reference.

Study	Vapor Pressure Equation	Limits (K)
Aldred & Pratt [71]	$\log_{10}(p[mmHg]) = 11.539 - \left(\frac{11025}{T[K] + 273.15}\right)$	763.7-817
Rosenblatt & Birchenall [72]	$\log_{10}(p[mmHg]) = 10.571 - \left(\frac{10300}{T[K] + 273.15}\right)$	966-1094
Yaws & Satyro [73]	$\log_{10}(p[mmHg]) = 5.8813 - \left(\frac{4984.6752}{T[°C] + 74.32}\right)$	807-1860

[2] At the melting point of 904 K.

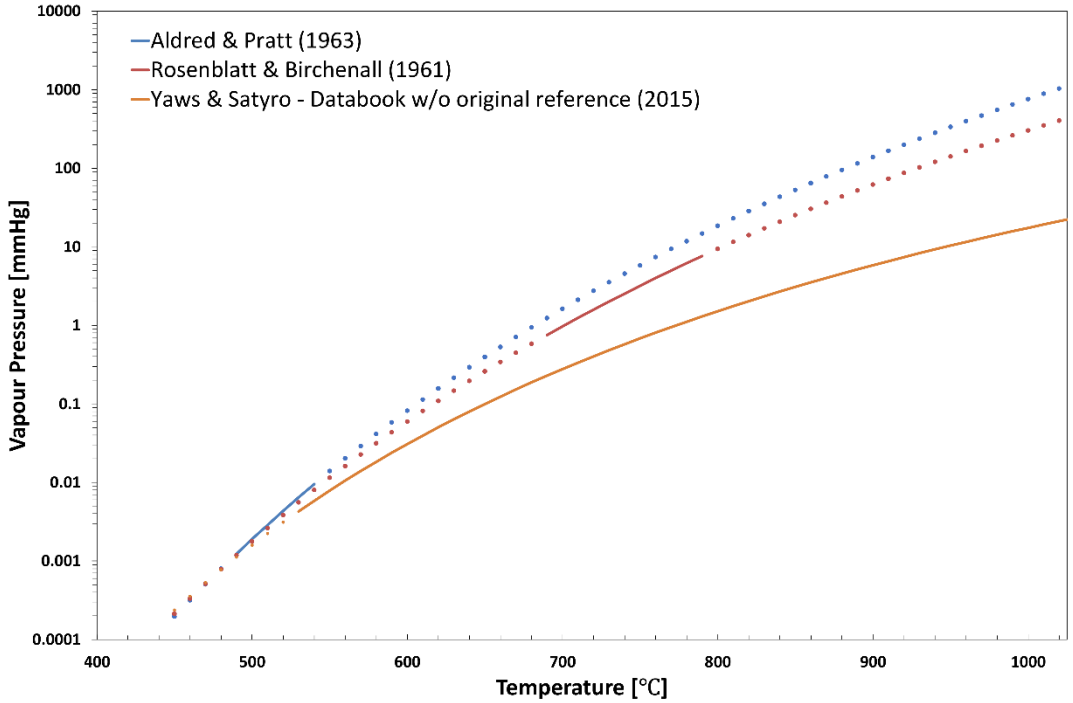

Figure 2.3. Vapor pressure of antimony predicted by the equations listed in Table 2.3. Solid lines represent the temperature range at which the stated equation is applicable. Dots represent the temperature ranges at which the equations are extrapolated.

The correlations provided by the first two entries in Table 2.3 are extracted from experiments, whereas the correlation given by Yaws and Satyro is a recommended formula based on experimental results and empirical models. For the calculations of vapor pressure of Sb, the correlation given by Rosenblatt and Birchenall was used in this study. This is due to the fact that when their correlation is extrapolated, the predicted values represent the experimental data of Aldred and Yaws well

The antimony is transported in and downstream of the furnace. Once the vapor exits the furnace, the nucleation starts to take place resulting in particle formation. In vapor and particle form, antimony is distributed in the system via both diffusion and convection. Therefore, the diffusion coefficients of Sb vapor and Sb particles amidst argon gas must be known. Two different sets of equations are utilized to calculate these diffusion coefficients. For the vapor phase, Chapman-Enskog kinetic theory [65] is used to calculate the diffusion coefficient of antimony.

$$D_{Sb} = \frac{3}{16}\sqrt{\frac{2(RT)^3}{\pi}\left(\frac{1}{M_{Sb}}+\frac{1}{M_{Ar}}\right)}\frac{1}{\widetilde{N}p\sigma_{Sb-Ar}^2\Omega_{\mathcal{D},Sb-Ar}} \tag{2.5}$$

where; D_{Sb} is the diffusion coefficient, R is the ideal gas constant, T is gas temperature, M_{Sb} and M_{Ar} are the molar masses of antimony vapor and argon [grams/mole], respectively, $\widetilde{N}$ is Avogadro's number, p is pressure [atm], σ_{Sb-Ar} is the collision diameter [m] and $\Omega_{\mathcal{D},Sb-Ar}$ is the temperature-dependent collision integral. The calculations for the collision diameter and the integral are given in Appendix C. The physics of diffusion related to particles is presented in Chapter 3.

2.2.3 Fused Silica Parameters

The tubular furnace includes a fused silica tube and the thermal properties of this tube contribute to the cooling of the gas at the outlet via axial conduction away from the furnace, and via free convection, and radiation into the ambient. The relevant physical properties of fused silica tubing are given in the table below.

Table 2.4. Physical constants of fused silica.

Physical Property	Value and Unit
Thermal conductivity	1.38 W/m·K [74]
Emissivity	0.9 [75]

2.3 Simulation Details

2.3.1 Structural and Operational Parameters

The structural and operational parameters are taken from the benchmark experiments [37, 62]. They are listed in Table 2.5. The system is kept under constant pressure; the furnace is set to a constant temperature and the experiments were conducted at steady-state conditions.

Table 2.5. Structural parameters of the furnace and the combustion boat.

Dimensions	Value and Unit
Heated region (furnace) length	300 mm
Outlet length	300 mm
Inner diameter	17 mm
Wall thickness	0.5 mm
Outer diameter	18 mm
Boat length	70 mm
Boat height	10 m
Boat top width	14 mm
Boat bottom width	8 mm

The operational parameters of the ECG are listed in Table 2.6. The volumetric flow rate into the system is given in standard cubic centimeters per minute (sccm) as it is the common unit of the mass flow controllers that feed gas to the generator. A conversion to SI units (m^3/s) can be done by utilizing the ideal gas law:

$$\dot{V} = \dot{V}_{sccm} \cdot \left(\frac{p_{stp}}{p}\right)\left(\frac{T}{T_{stp}}\right)\frac{10^{-3}}{60} \tag{2.6}$$

In the equation above, $\dot{V}$ is the volumetric flow rate and the *stp* subscript indicates the standard temperature and pressure conditions of 273.15 K and 1 atm.

Table 2.6. Operational parameters of the system. These parameters were used in all calculations unless otherwise noted.

Parameter	Value and Unit
Volumetric Flow Rate	500 sccm
Inlet Temperature	298 K
Furnace Temperature	823 K
Ambient Temperature	298 K
Pressure	6 Torr

The main areas of interest within our system are the furnace and the section downstream of it. The governing equations and their corresponding boundary conditions that apply in those domains are provided with justifications in the next subsection.

2.3.2 Equations of Momentum Transport

Operational pressure of the system is low and therefore whether the system can still be described by the continuum approach must be checked. Knudsen number for the argon gas was evaluated $Kn_{Ar} = l_{p,Ar}/L_c$, where $l_{p,Ar}$ is the mean free path of the argon molecules and the characteristic length, L_c , which was taken as the inner diameter of the tube. Under the conditions of 550 K and 6 Torr, Kn_{Ar} was evaluated to have a maximum value of 10^{-3}. Therefore, argon and transport phenomena that happen in it obey the continuum description for the flow.

Another important flow condition that must be considered in our system is the flow regime. The flow regime in which the argon gas passes through the system is determined by the Reynolds number, $Re = D\langle v_z\rangle\rho/\mu$, where D is the diameter of the circular conduit, $\langle v_z\rangle$ is the average linear velocity and μ is the dynamic viscosity[65]. $\langle v_z\rangle$ increases with decreasing pressure (see Equation 2.6) but ρ decreases, therefore Re is independent of pressure. The same trend roughly applies to temperature since μ is a rather weak function on temperature (Equation 2.1). The pressure independency can be seen more clearly when Re is described in terms of inlet volumetric flow rate, $Re = 4\dot{V}_{sccm}\rho_{stp}/\pi D\mu$. Between the operational conditions of 100 sccm and 1000 sccm, Re ranges from approximately 10 to 100 under the given operational conditions, indicating laminar flow to present everywhere in the generator

The effect of Sb vapor that gets introduced to the system is assumed to have no effect on the momentum transport in the system. This is due to the fact that the amount of Sb vapor that is present in the system at all times is very small, which can be justified by calculating the vapor pressure of the antimony. At 823 K temperature, the vapor pressure of antimony is 11.4 mTorr according to Rosenblatt [72]. This is the maximum partial pressure of Sb vapor in the system, which should be present only on top of the solid Sb surface in the boat, and therefore partial pressure of Sb should be lower anywhere else due to dispersion and dilution. At 6 Torr total pressure, the equilibrium vapor pressure indicates that the maximum mole fraction of Sb vapor is 1.905×10^{-3}, which is adequate for assuming this system to be dilute in Sb.

In addition to the flow regime of the argon gas in the system, the compressibility of the flow also needs to be taken into the consideration. The extent of compressibility is determined by the Mach number, $Ma = v/c$, where v is the local flow velocity and c is the speed of sound in argon under operational conditions of the system. Considering that argon behaves as an ideal gas under the conditions investigated, the speed of sound in argon can be estimated as $c = \sqrt{(R/M_{Ar})T\gamma}$,

where γ is the specific heat ratio, which can be assumed to be equal to 1.66 for a monoatomic ideal gas such as argon. The Mach number for the system is determined to be 0.04 when the calculations are performed with the linear maximum velocity. The value is smaller than the threshold value 0.3, which sets the upper limit for incompressible flow. Regardless, the flow is taken to be compressible due to the presence of a temperature field, which would result in a significant change in density and therefore velocity. Under these conditions, the governing equations for laminar flow, i.e. momentum conservation equation and continuity, in the system are defined as following:

$$\rho(\boldsymbol{u} \cdot \boldsymbol{\nabla})\boldsymbol{u} = \nabla \cdot [-p\boldsymbol{I} + \boldsymbol{K}] + \boldsymbol{F} \quad (2.7)$$

$$\nabla \cdot (\rho \boldsymbol{u}) = 0 \quad (2.8)$$

where; ρ is the density of argon (described with Equation 2.3), $\boldsymbol{u}$ is the velocity vector, p is the pressure of the system, $\boldsymbol{I}$ is the identity matrix, $\boldsymbol{K}$ is the shear stress tensor, $\boldsymbol{F}$ is the body force vector. For our system, the obvious body force is gravity, but it is not included as the tubular furnace is horizontal, its vertical thickness is small (17 mm) and density is low due to low pressure, resulting in negligible gravity effects. The boundaries for the momentum transport are shown in Figure 2.4.

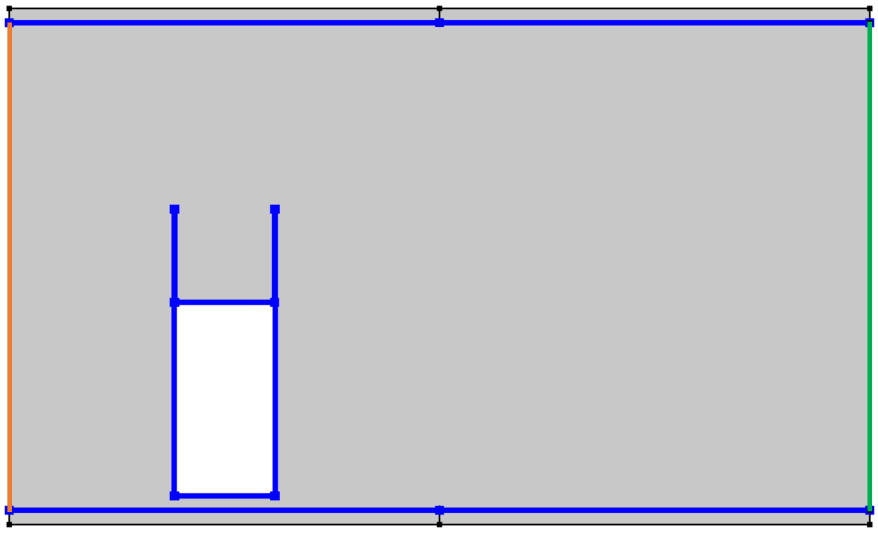

Figure 2.4. **Boundaries for fluid flow.** Orange line on the left is the inlet boundary, green line on the right is the outlet boundary and blue lines are the wall boundaries.

The following boundary conditions are assigned for closing the equations of fluid flow. At the inlet we have a fully developed laminar flow (parabolic velocity profile) with the average velocity calculated from the inlet flow rate and the geometry of the system. On the walls and the surface of the Sb metal in the boat, we have assigned the no-slip boundary condition. The boundaries for the momentum transport are demonstrated in Figure 2.4.

$$\boldsymbol{u} = 0 \tag{2.9}$$

This is due to the fact that the surface of Sb is taken as a solid boundary since operation temperatures are below the melting point of Sb (904 K). At the outlet we have defined the pressure to have a fixed value of 6 Torr.

2.3.3 Equations of Heat Transfer in Solids and Fluids

There are several heat transfer mechanisms occurring concurrently within the ECG. The main mechanisms that are taking place are convection and conduction. The convection mechanisms heat the argon gas as it flows through the heated region of the generator and also cools the outlet gas and the tube via free convection. The conduction occurs at the outlet tube that is connected to the furnace. The general governing equations for the heat transfer physics are defined as the following,

$$d_z \rho C_p \boldsymbol{u} \cdot \nabla T + d_z \nabla \cdot \boldsymbol{q} = d_z \dot{Q} + q_0 \tag{2.10}$$

$$\boldsymbol{q} = -k \nabla T \tag{2.11}$$

where, d_z is the in-plane thickness[3], ρ is the fluid density, C_p is the heat capacity at constant pressure, $\boldsymbol{u}$ is the velocity vector, T is the temperature, $\boldsymbol{q}$ is the conductive heat flux defined Fourier's law in Equation 2.11. In the equations above, k is the thermal conductivity, $\dot{Q}$ is the heat source term and q_0 is the external heat flux.

[3] Due to the 2-D geometry, the value of d_z does not change the temperature field. It is only used when calculating flow rates of quantities. Such calculations are done for mass transfer, and they are detailed in the next two chapters.

The temperature of the furnace region, i.e. the walls of the fused silica tube inside the furnace, the boat walls, and the surface of the Sb, was taken to be constant at 823 K. In practice, the temperature in most tubular furnaces varies axially, and most of the time, the temperature reported by the sensor of the furnace corresponds to some average temperature. An example of this is given in Figure 2.5. Since predicting such a temperature profile would require modeling on the scale of the entire furnace that includes heating elements, insulation materials and circuitry, constant temperature was assumed in this work. It is known that the temperature variation does not complicate operation as long as the boat is placed at the same location in the furnace [62]. It is also known that the temperature profile does not lead to significant vapor condensation inside the furnace [see Appendix D]. However, the maximum temperature in the furnace being higher than the temperature measured by the sensor hampers the prediction capabilities of the model slightly. Therefore, it is best to accept at this point that average temperature that the Sb in the boat gets subjected can differ by ± few tens of K, which consequently changes the vapor pressure. Since vapor pressure directly affects the amounts of vapor produced in the furnace and the resulting amount of mass output, it is actually the boat temperature that should either be measured or estimated for a fully predictive model. Such detail is omitted in this work. With the uncertainty that comes from the effective temperature that the evaporating element is subject to, and the sensitivity of vapor pressure with respect to temperature, predicting the mass output of an experimental generator with high accuracy is rather difficult, but yield is expected to the less dependent on operating temperature.

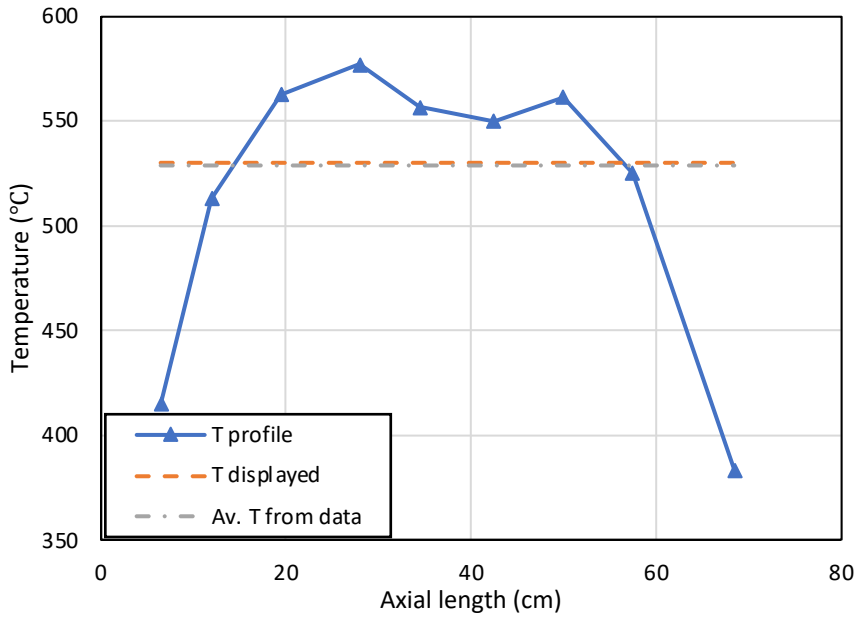

Figure 2.5. Temperature profile of a tubular furnace used as an ECG [76]. The furnace (Series 1200, CM Furnaces Inc., USA) was 74 cm long. The solid line depicts the pointwise temperature within the furnace measured by a long and translatable thermocouple, whereas the dotted line represents the set temperature of the furnace (530 °C). Numerical average of the pointwise data is found to be approximately equal to the set temperature of the furnace (528.6 °C).

In the outlet tube walls which is open to atmosphere, conjugate heat transfer is taking place. Argon exits the furnace at 823 K and as it passes through the colder outlet, where heat transfer between the walls and the gas occurs. Along the axial direction, conduction is taking place within the walls of the outlet tube. Lastly, since the tube at the outlet is surrounded by the ambient environment, heat is lost to the surroundings through both free convection and radiation. Estimating the heat lost by free convection requires the evaluation of the convective heat transfer coefficient for air that surrounds the outlet tube. This transfer coefficient is calculated via a series of equations valid for a long horizontal cylinder [74].

$$Nu_d = \left\{ 0.60 + \frac{0.387 Ra_d^{\frac{1}{6}}}{\left[1 + (0.559/Pr)^{\frac{9}{16}}\right]^{\frac{8}{27}}} \right\}^2, \qquad Ra_d \leqslant 10^{12} \tag{2.12}$$

$$Nu_d = \frac{h_a d}{k_a} \tag{2.13}$$

Nu_d is the average Nusselt number over the circumference of the tube, Ra_d is the Rayleigh number, Pr is the Prandtl number, h_a is the convective heat transfer coefficient averaged over the tangential direction, d outer tube diameter, k_a is the thermal conductivity of air. Definitions of the dimensionless parameters are given below,

$$Ra_d = \frac{g\beta(T_s - T_\infty)d^3}{\nu\alpha} \tag{2.14}$$

where g is the gravitational acceleration constant, β is the volumetric thermal expansion coefficient taken as $1/T$, T_s is the surface temperature of the tube, T_∞ is the ambient temperature, ν is the kinematic viscosity and α is the thermal diffusivity, both of air. Physical parameters of air are evaluated at the average air temperature, $\bar{T} = (T_s + T_\infty)/2$. The heat flux equation at the outer wall of the outlet is then defined in the following manner:

$$\boldsymbol{q}_{Outlet} = \boldsymbol{q}_{Natural\ Convection} + \boldsymbol{q}_{Radiation} \tag{2.15}$$

$$\boldsymbol{q}_{Outlet} = h_a(T_s - T_\infty) + \varepsilon\sigma\left({T_\infty}^4 - {T_s}^4\right) \tag{2.16}$$

In Equation 2.16, h_a is the convective heat transfer coefficient evaluated using equation 2.13, ε is the emissivity of fused silica and σ is the Stefan-Boltzmann constant. The equation above assumes that fused silica is fully opaque when emitting the IR radiation and thus heat is only lost from the exterior surface of the fused silica tube.

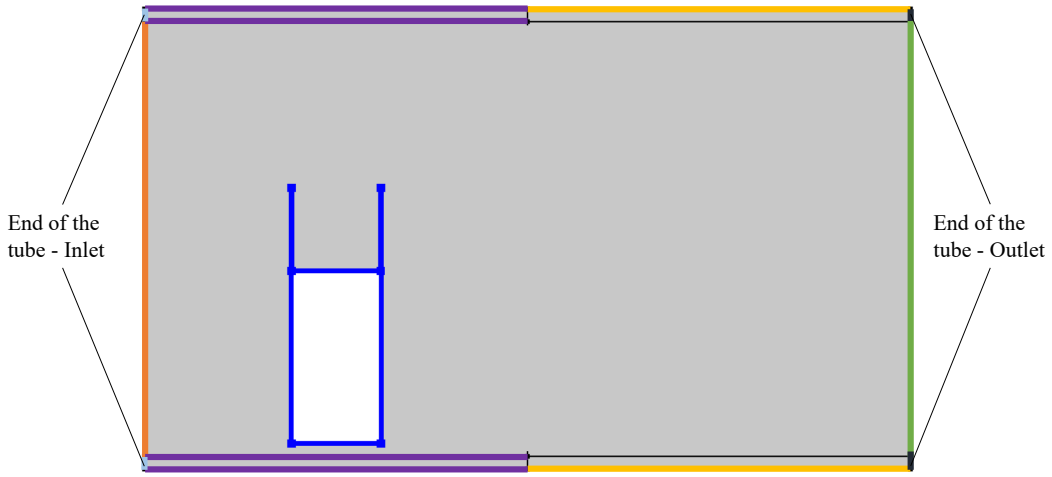

Figure 2.6. **Boundaries for heat transport.** Orange line on the left is the inlet boundary, green line on the right is the outlet boundary, purple lines are the furnace boundaries, dark blue lines are the combustion boat boundaries, yellow lines are the outlet walls boundaries. Along the thickness of the tube there is an inlet wall boundary (light blue on the left) and an outlet wall boundary (dark grey on the right).

At the inlet, on the boundaries of the furnace, on the walls of the boat and the surface of the Sb, a fixed temperature boundary condition of 823 K was assigned. At the outer walls of the outlet tube, surface-to-ambient cooling boundary condition was assigned. On the ends of the outlet tube a no flux boundary condition was defined.

2.3.4 Equations of Mass Transfer

The mass transport equations describe the distribution of Sb vapor within the system. It was shown above that the maximum mole fraction of Sb is very low at the temperatures and pressures investigated in this study. Therefore, it is safe to employ a dilute system-approach, where the diffusive flux of Sb is modeled with Fick's Law and advective flux is determined by argon flow. The governing equations of mass transfer are given below:

$$\nabla \cdot (\boldsymbol{J}_{Sb} + \boldsymbol{u}c_{Sb}) = R_{Sb} \tag{2.17}$$

$$\boldsymbol{J}_{Sb} = -D_{Sb}\nabla c_{Sb} \tag{2.18}$$

where, $\boldsymbol{J}_{Sb}$ is the diffusion flux vector. D_{Sb} is the diffusion coefficient, $\boldsymbol{u}$ is the velocity vector, c_{Sb} is the concentration of Sb and R_{Sb} is the volumetric reaction rate for the vapor. The diffusion coefficient for Sb vapor in the system is determined via the Chapman-Enskog kinetic theory equations which were previously mentioned in section 2.2.2 above (Equation 2.5). Note that the diffusion coefficient was implemented as a temperature-dependent parameter, where $D_{Sb} \propto T^{3/2}$ according to the Chapman-Enskog theory.

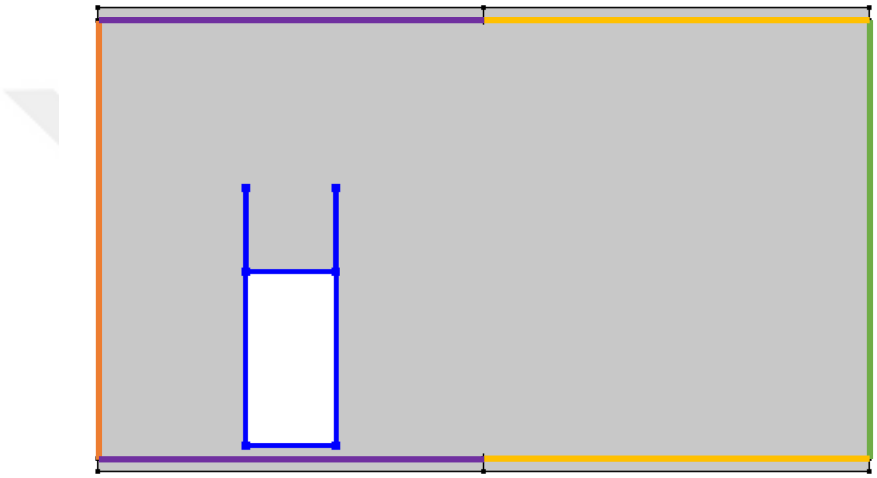

Figure 2.7. **Boundaries for mass transport.** Orange line on the left is the inlet boundary, green line on the right is the outlet boundary, purple lines are the furnace boundary, dark blue lines are the combustion boat boundary, yellow lines are the outlet walls boundary.

At the inlet, there is no Sb vapor present, therefore the concentration boundary condition indicating this, $C = 0$, was applied. On the surface of solid Sb in the boat, the boundary condition reflects the Sb concentration which is directly correlated with the equilibrium vapor pressure. Just above the solid Sb surface, the vapor concentration was set to:

$$C_{Sb}^{vap} = \frac{P^{vap}}{RT} \tag{2.19}$$

Based on previous experience (Appendix D), flux of Sb inside the furnace walls and on the combustion boat walls were set to zero, i.e. $\boldsymbol{J_{Sb}} = 0$, preventing any deposition. On the walls of the outlet due to the temperature gradients, wall

deposition occurs since condensation can become favorable. This was described by a special boundary condition of flux type, which was written on the basis that when the partial pressure of the Sb exceeds the vapor pressure at a given temperature[4], the excess Sb vapor deposits on the walls:

$$\boldsymbol{J}_{Sb,wall} = \frac{1}{4}\frac{v_{th}}{RT}\Phi_s(C_{Sb}RT, P^{vap}) \tag{2.20}$$

In this equation, v_{th} refers to the mean thermal velocity of vapor atoms, and it was calculated as $\sqrt{8k_BT/\pi Mn_{Sb}}$. C_{Sb} refers to the Sb vapor concentration near the wall and k_B is the Boltzmann constant. In COMSOL, this equation was coupled with a sigmoidal step function, shown with $\Phi_s(C_{Sb}RT, P^{vap})$ in the equation above, in order to create a smooth transition from no wall deposition to deposition. The step function represents the conditional physics involved, and it has the argument of $P_{Sb} - P_{Sb}^{vap}$, with the transition zone size of 0.001 Pa (see Appendix E for details). As soon as the partial pressure of Sb exceeds the vapor pressure, the step function changes from 0 to 1 resulting in wall deposition. The wall deposition flux is defined here as the product of excess concentration, calculated by $(P_{Sb} - P_{Sb}^{vap})/RT$, and the thermal velocity. The coefficient of ¼ gives the directionality to the particle fluxes that are colliding with the walls and comes from kinetic theory [77]. A mathematical summary of all boundary conditions employed in modeling the overall transport phenomena is presented in Appendix F.

2.4 Solution of Multiphysics Equations

The model domain was meshed entirely with triangular elements. While a swept (i.e. extruded) and quadrilateral mesh could be used with less cell count and degree of freedom, the ability to adapt and improve triangular elements as a function of square of residuals (the L2 norm) deemed to be useful. Consequently, adaptive

[4] The saturation ratio, defined in Chapter 4 determines both the direction and rate of condensation-evaporation phenomena.

meshing was employed to improve accuracy and resolution, especially around the exit of the furnace and the beginning of the outlet region, as shown in Figure 2.8.

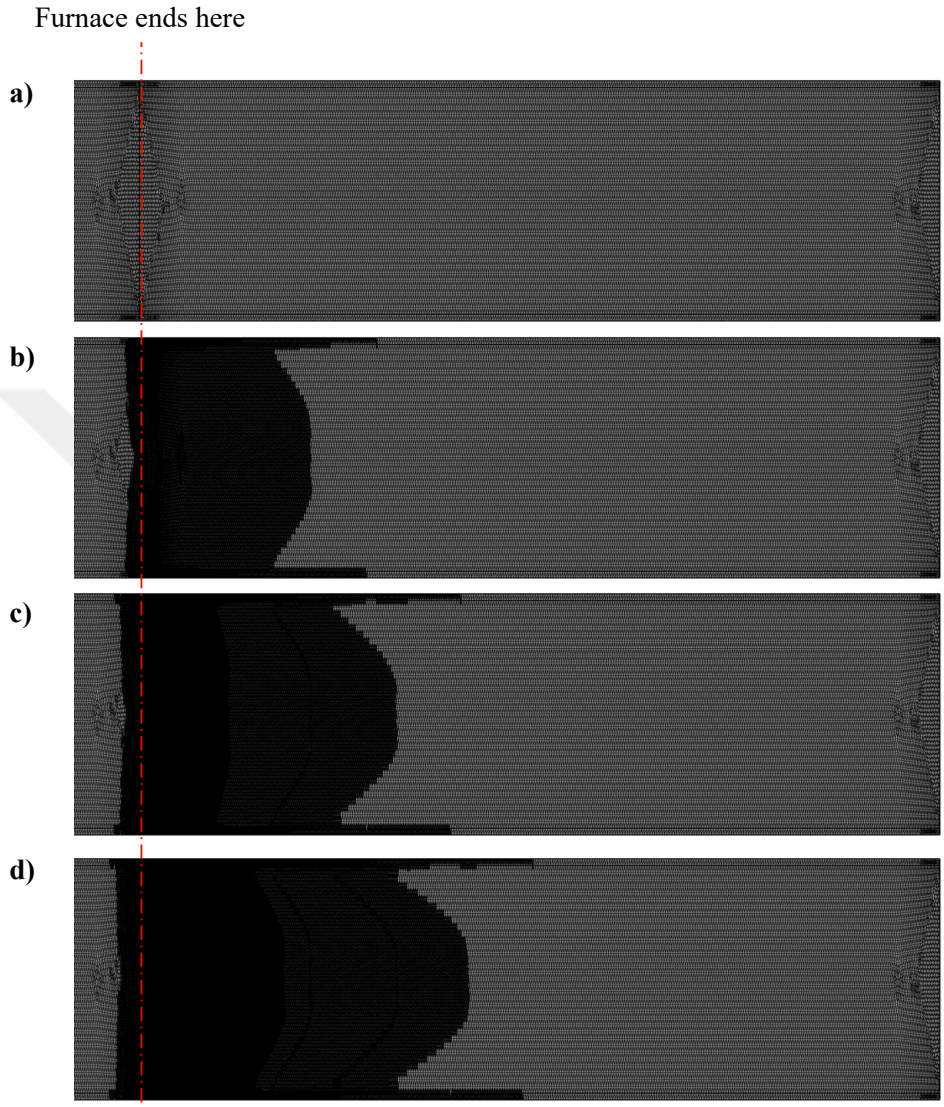

Figure 2.8. Adaptive triangular mesh in the system. Geometry is 1:5 scaled for the *x*:*y* axes. a) Initial mesh b) Level 1 adaptive mesh c) Level 2 adaptive mesh d) Level 3 adaptive mesh.

The number of numerical cells used was approximately 67 000 for the initial mesh, and it increased to 342 000 after 3 adaptation steps.

The momentum and heat transfer equations form a strongly coupled pair of nonlinear partial differential equations. Difficulties were encountered in solving the

two physics simultaneously, where convergence appeared to be either very slow or not possible. Therefore, a strategy was devised to achieve convergence. First, flow rate was taken as a continuation parameter in momentum transfer, that is, flow rate was slowly increased stepwise up to the desired value and the solution obtained for every flow rate was used as the initial condition for the next until the desired flow rate is reached, so that convergence is achieved at flow velocities. For heat transfer-coupling, momentum transfer equations were solved isothermally at furnace temperature (823 K) with initial iteration values of $\boldsymbol{u} = 0$ and $P = 6$ Torr everywhere, and the resulting flow field was used as the initial condition for a second solver that coupled momentum and heat transfer. Ambient conditions (298 K) were used everywhere in the model domain as the starting point for iterations for heat transfer equations. Adaptive meshing was incorporated for this solver to improve resolution in flow and temperature field at the outlet. Then, the resulting non-isothermal flow solution was used to solve the equations of mass transfer where Sb vapor is a dilute species on the same adapted mesh. An initial value of $C_{Sb} = 0$ was used everywhere in the model domain where mass transfer equations were solved. The presence of Sb does not affect the momentum and heat transfer in the ECG, therefore mass transfer is one-way-coupled to momentum and heat transfer. The coupling of the physics in the ECG is depicted in the Figure 2.9. Mesh independence and mass conservation, two important requirements of consistent and accurate numerical calculations, are detailed in the Appendix G.

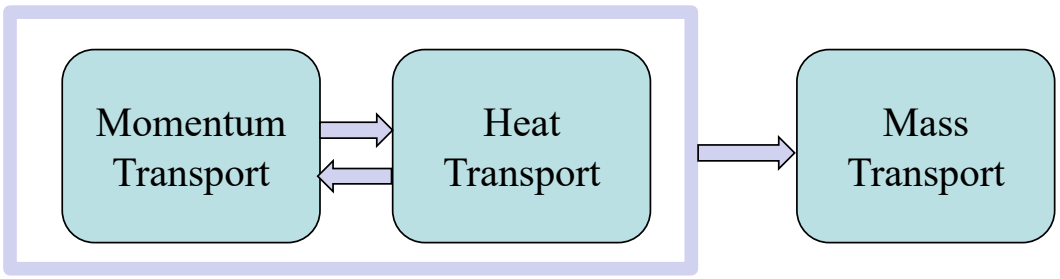

Figure 2.9. Physics coupling in the simulation. Momentum transfer and heat transfer are two-way coupled, but mass transfer is one-way coupled to momentum and heat transfer.

CHAPTER 3

VAPOR TRANSPORT

This chapter presents the results of the calculations done using CFD in the ECG. By using the physics coupling detailed in the previous chapter, the flow of argon through and out of the ECG is simulated through the solution of momentum transfer equations, which is coupled with heat transfer. The Sb vapor that comes from the boat in the furnace gets carried by advection and eventually diffuses to the walls at the outlet of the ECG. The heat lost downstream of the furnace outlet affects mass transfer significantly, the flow decelerates, and residence time increases due to cooling. In the meantime, the vapor cools down and deposition on the cold walls become favorable. It is shown that solely modeling the vapor leads to miniscule mass yields and mass outputs, indicating that no vapor leaves ECG, and for replicating mass yields and mass outputs that agree with the benchmark, modeling particle formation is a necessity.

3.1 Momentum Transfer

The momentum transfer and resulting fluid flow phenomena was investigated under two different flow rate conditions, 200 sccm and 500 sccm. The results for the velocity profiles in the system for 500 sccm flow rate of argon are presented in Figure 3.1 and Figure 3.2.

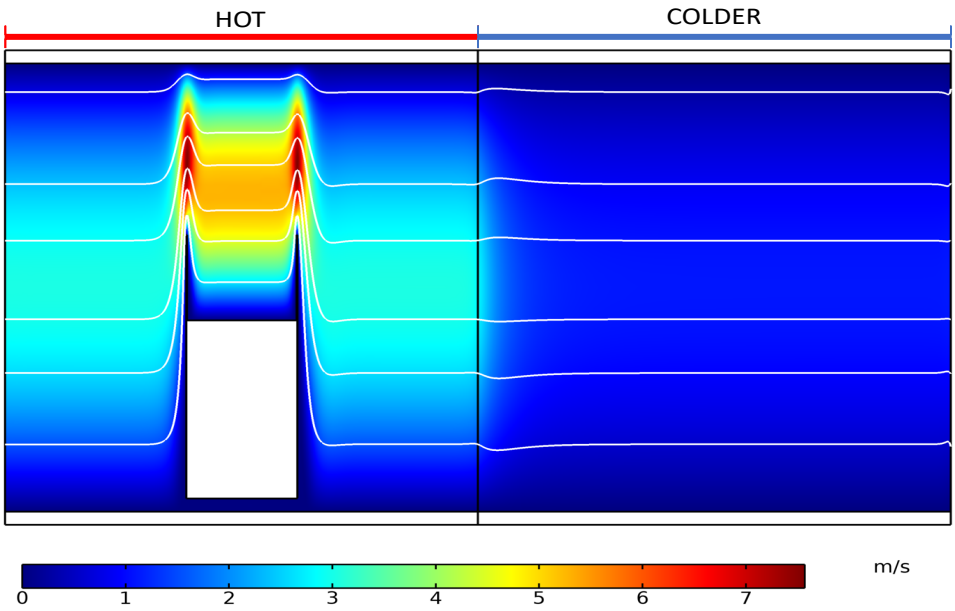

Figure 3.1. Flow map in the ECG. The argon flow rate is 500 sccm and the system pressure is 6 Torr. The pressure drop in the axial direction within the system was evaluated to be only 20 mTorr.

Due to the presence of the boat at the center of the furnace, the argon flow gets compressed over the boat, and expands as soon as it passes the boat, as demonstrated by the streamlines in Figure 3.1, creating a complicated flow pattern. The major complication stems from the boat walls. The distance between boat's top wall surface and the antimony surface determines distance over which the flow expands into the boat. Since momentum diffusivity increases with decreasing pressure[5], it was observed that flow was able to penetrate into the boat (Figure 3.2) fairly well. However, since mass transfer from surfaces subject to laminar sweeping flow is dependent on the velocity gradient and contact time nearby the surface[6], the rate of removal of Sb vapor from the solid Sb surface is expected to depend on the amount of Sb in the boat[65].

[5] $\nu = \mu/\rho$, and μ is practically independent of pressure, but ρ is.
[6] A.k.a. Leveque theory of heat and mass transfer.

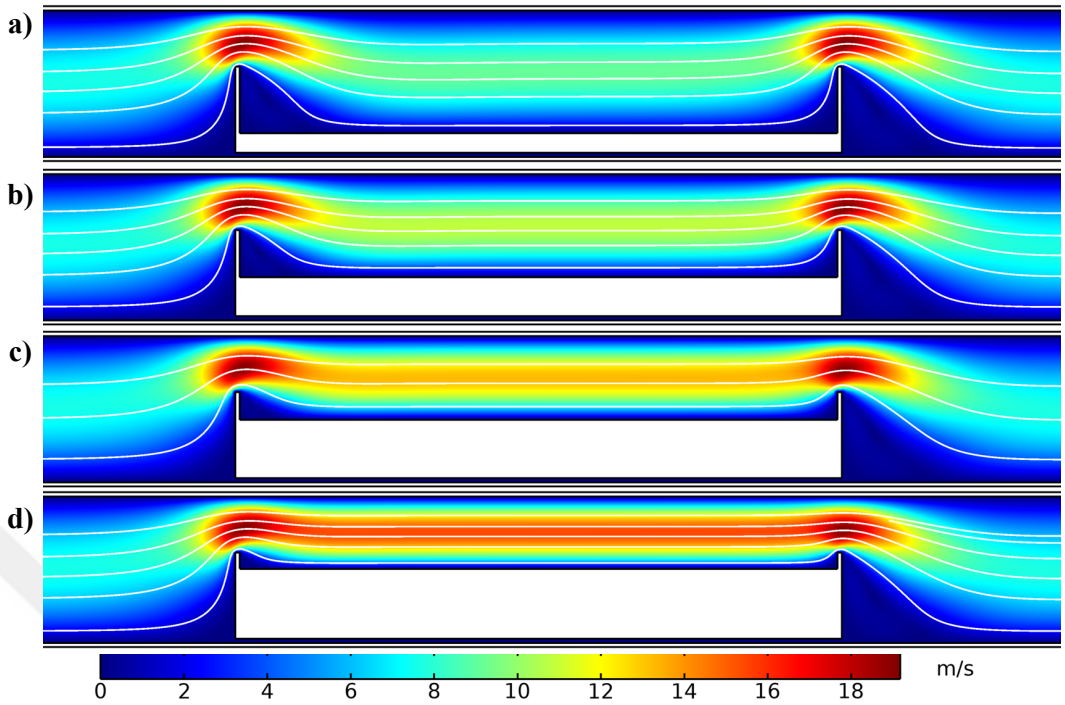

Figure 3.2. Effect of Sb amount in the boat to gas flow. The flow is from left to the right. The height of the solid antimony layer increases from panel a to d. Fill percentages and total Sb weight are accordingly a) 25 % (8.2 g), b) 50 % (16.5 g), c) 75 % (24.6 g) and d) 90 % (29.7 g).

Since momentum transport is two-way coupled with the heat transfer in the ECG, flow velocities decrease downstream of the furnace. The differences of the velocity profiles in the furnace and the downstream can be qualitatively seen in Figure 3.1. A more quantitative presentation of this effect is shown in Figures 3.3 and 3.4 by preparing linear data sets on the flow map (to be called cut lines from now on). Flow velocities were evaluated on these sets as shown below.

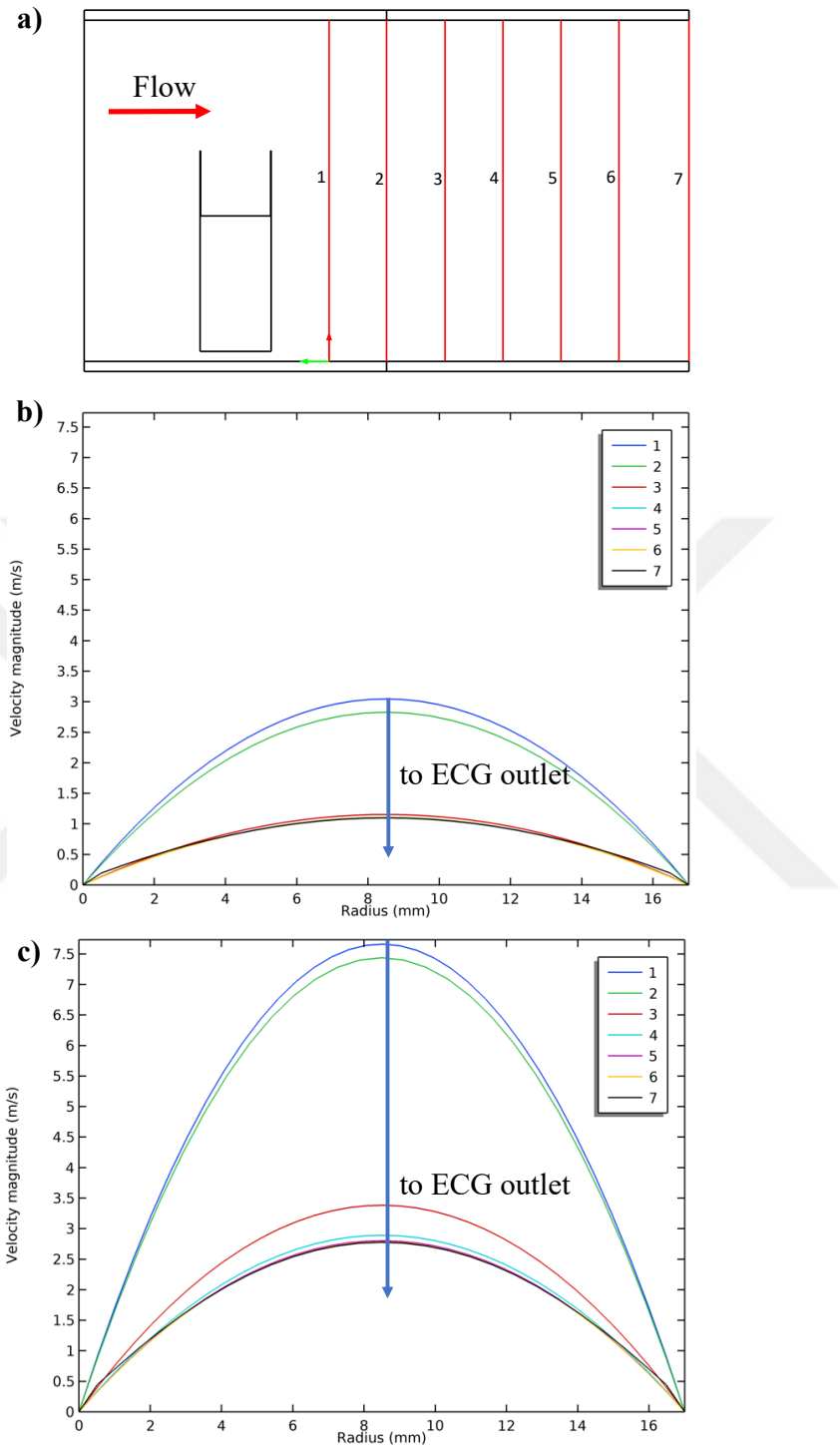

Figure 3.3. Velocity profiles in the vertical plane a) Vertical cut lines taken at positions further away from the boat. #2 indicates the exit of the furnace. The red lines indicate the cut lines at which the velocity profiles were extracted for b) 200 sccm flow rate c) 500 sccm flow rate.

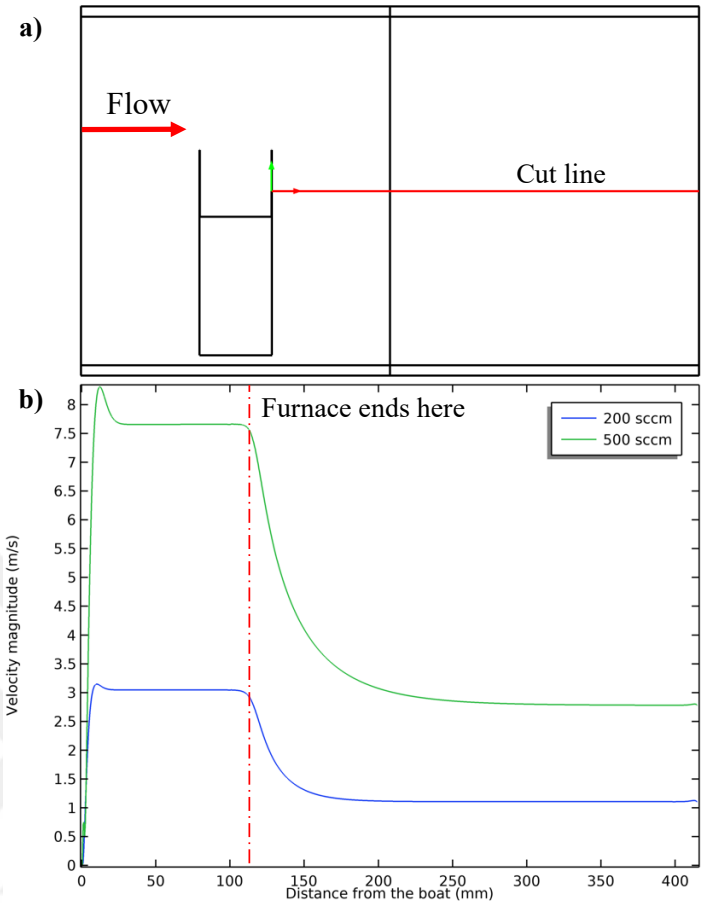

Figure 3.4. Velocity profiles in the horizontal plane a) Horizontal cut line, shown with red, which presents the centerline of the geometry starting downstream of the boat. b) Velocity calculated on the cut line. The blue and green lines indicate the velocity profiles for 200 sccm and 500 sccm respectively.

Due to low Re and high ν, flow retains its parabolic profile downstream of the boat as temperature decreases, but maximum velocity values drop significantly (Figure 3.3). For example, it can be seen that at vertical cut line 1 in Figure 3.3, the maximum velocities are 7.66 m/s and 3.05 m/s for 500 and 200 sccm, and at the vertical cut line 7 the maximum velocities are 2.76 m/s and 1.09 m/s, respectively at 200 sccm, the maximum velocity decreases by almost three times. Hence, maximum and minimum centerline velocities expectedly scale approximately linearly with volumetric flow rates, 200 sccm and 500 sccm in Figures 3.4. However, since cooling is more efficient at lower flow rates, deceleration of flow happens on a shorter length scale. The range over which the deceleration occurs is determined by

heat transfer, as detailed in the next subsection. This deceleration zone is important since it determines how long the vapor stays in a cooling zone. The extent of this zone is expected to play a major role in nucleation and particle growth.

An alternative view of flow dynamics in shown in Figure 3.4, where a horizontal cut line was prepared to visualize acceleration starting from the end of the combustion boat in continuous fashion. Beyond the boat, expansion starts and then cooling occurs. At the walls of the boat the no slip boundary condition was applied, causing the velocity profiles to start from zero. The small peaks and the beginning of the plateau region indicate where the expansion of the argon gas is completed within the furnace. For both flow rates, 200 and 500 sccm, the first plateau is located within the furnace at 823 K, and the second plateau is downstream of the furnace where the gas is cooling down to ambient temperature.

3.2 Heat Transfer

The heat transfer downstream of the furnace is affected by the heat retained in the fused silica tube and the heat lost to the surroundings. At the outlet, the convective heat transfer coefficient for natural convection cooling around the tube changes with the external surface temperature of the tube. This effect was taken into account by defining the convective heat transfer coefficient, h_a, as a temperature-dependent variable evaluated at a temperature average of the ambient temperature and the local external surface temperature on the tube. The correlation given in Equation 2.12 was used to determine the convective heat transfer coefficient. The correlation is applicable under the condition of Ra_D smaller than 10^{12} [74]. The Ra_D values at the exit of the furnace and at the end of the tube were calculated and found to be approximately 30300 and 33, respectively, at 500 sccm flow.

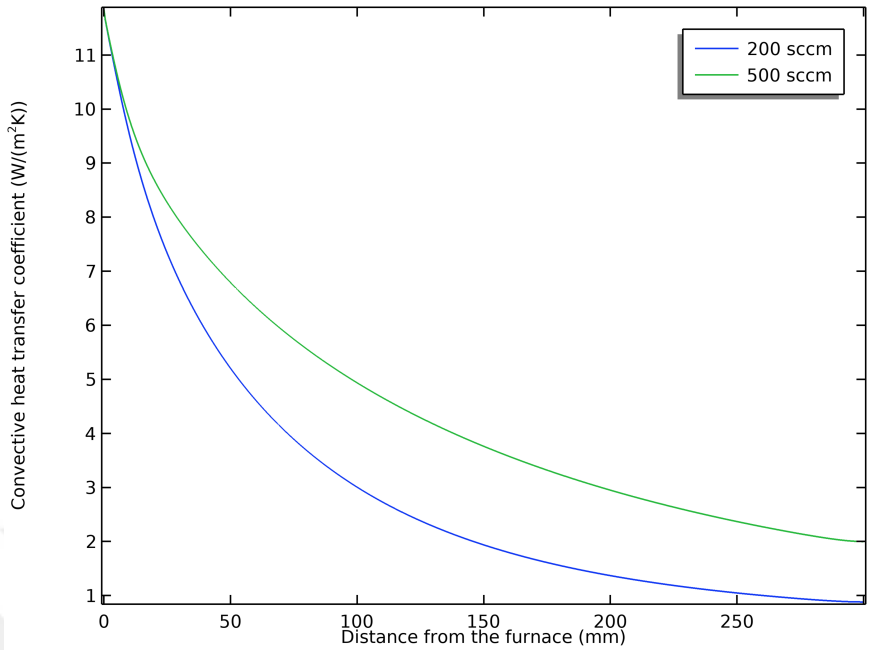

Figure 3.5. Variation of convective heat transfer coefficient around the outlet tube for 200 and 500 sccm flow. The value of h_a decreases exponentially with the increasing distance from the furnace.

In the Figure 3.5 it is seen that the value of convective heat transfer coefficient of air decreases as distance from the exit of the furnace increases. Accordingly, the ratio of radiative and convective cooling rates, $\beta = \varepsilon\sigma(T^4 - T_\infty^4)/[h_a(T - T_\infty)]$, is always larger than 1 (Figure 3.6), indicating that radiative losses always play an important role in the development of the temperature at the outlet, especially within the first few cm away from the furnace due to large temperature differences.

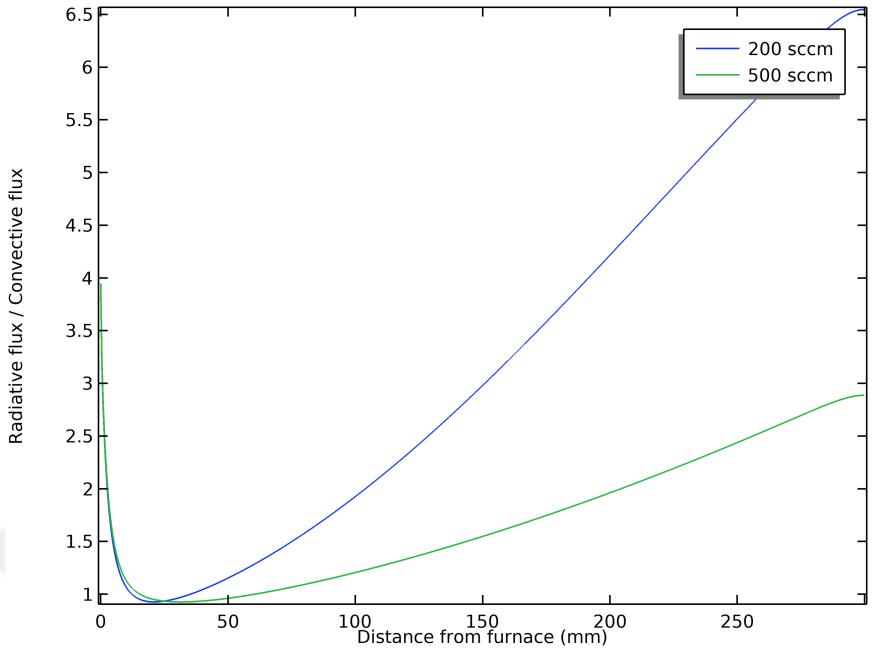

Figure 3.6. Ratio of radiative flux to convective flux at the outlet tube for 200 and 500 sccm flow.

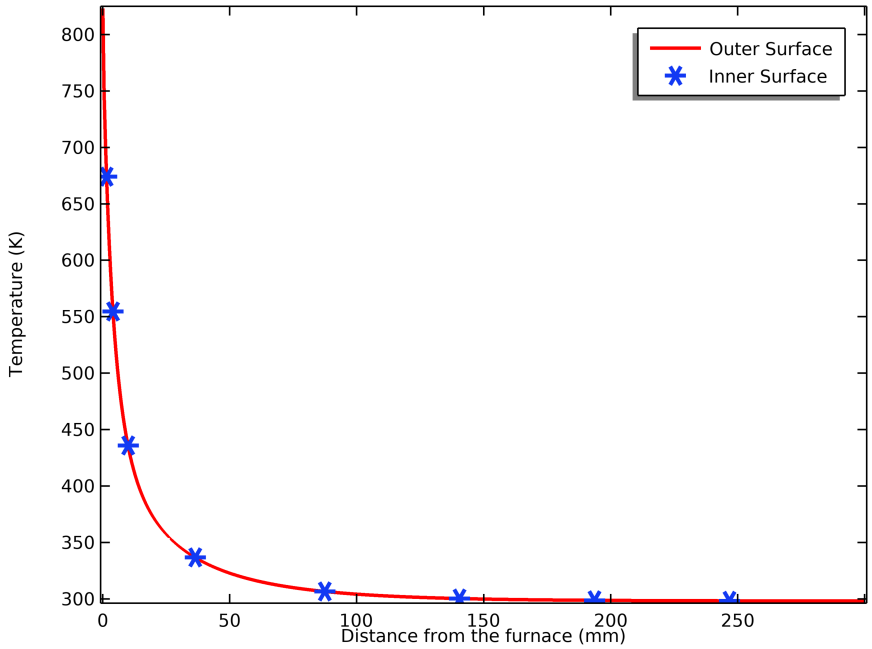

Figure 3.7. Temperature profile on the outlet tube for 500 sccm flow. The red solid line indicates the temperature profile at the outer surface of the outlet wall and the asterisk indicate the temperature values at the center of the wall. Overlapping profiles indicate that the temperature gradient across the tube wall is insignificant, which was expected due to the dimensions of the tube (i.e. small Biot number).

Expectedly, the wall temperature and cooling rates affect each other. For example, as wall temperature increases, the value of h_a also increases, as well as β, as shown in Figure 3.5. Figure 3.7 shows that the distance over which the outlet tube cools is approximately 5 cm. This length is approximately two times shorter than what was observed in the benchmark [62] . Radiation emanating from the interior of the furnace and exiting through the insulation blocks, as seen in Figure D2 in the Appendix, is thought to be the reason.

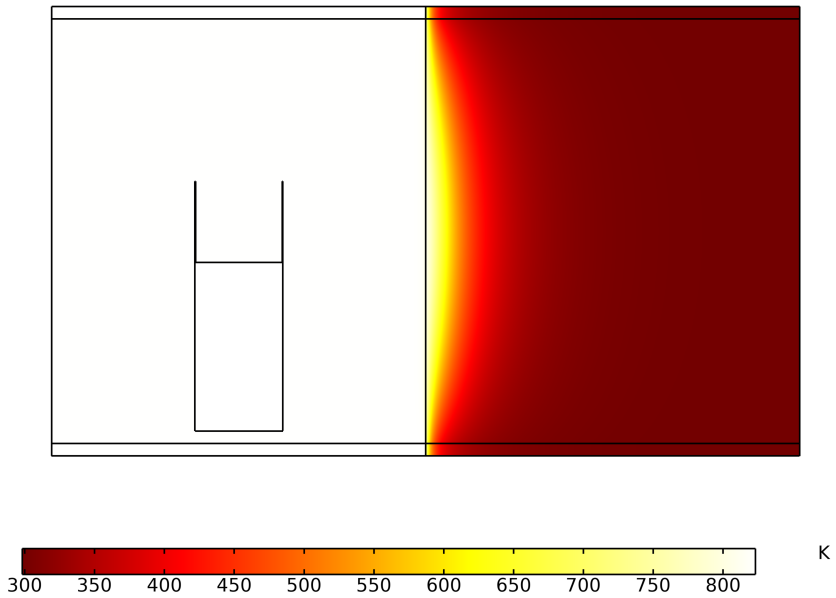

Figure 3.8. Temperature flow map in the ECG for 500 sccm flow. As soon as the gas leaves the furnace it is cooled down rapidly.

The temperature distribution downstream of the generator is shown in Figure 3.8 and it carries similar features with the flow field given in Figure 3.1, specifically for the outlet section. Downstream of the furnace, at the center of the tube where the velocity is at its highest the temperature is also at its highest. Cooling of the gas in this region slows the gas. Accordingly, Figures 3.1 and 3.8 show the two-way coupling of the momentum and heat transfer in the system.

3.3 Vapor transport

The rapid cooling downstream of the furnace creates a highly supersaturated vapor and therefore favors deposition on the walls of the outlet. Despite the decrease in the diffusion coefficient with temperature downstream, the coefficient has a minimum order of magnitude of 10^{-3} m^2/s due to operation at low pressure. Hence, vapor loss to the walls is significant. Figure 3.9 shows the concentration profile of Sb vapor in the system at 200 and 500 sccm. These calculations do not include the formation of a solid phase. It is observed that the vapor quickly distributes itself uniformly just after the boat and a symmetric distribution is obtained at the exit of the furnace. This is followed by rapid diffusion to the walls. Note that the sharp decay in the axial direction is associated with the rescaling of the dimensions, as detailed in the previous chapter. These results indicate that a mathematical description of vapor recovery from the boat would enable a simpler simulation, where only the downstream of the furnace is modeled with the following boundary condition at the furnace outlet

$$J = \frac{\dot{n}_{evap}}{A_f} \tag{3.1}$$

where $\dot{n}_{evap}$ is the molar evaporation rate from the boat and A_f is the cross-section area of the tube in the furnace. The calculations presented here aim at developing a reliable modeling benchmark for such reduced models, however, the development and testing of such models is left for future work. One of major points of interest is investigating the mass flow rate of Sb that comes out of the evaporator, which is on the order of 1 mg/min for the conditions of the benchmark as measured by collecting the particulate Sb mass on a filter sufficiently far away from the ECG [37]. Another important quantity is the yield, which is defined as the fraction of the amount of evaporated mass that leaves the ECG. This quantity has a time-averaged value of 10% for the benchmark [62].

In Figure 3.9 the concentration distribution along with the flux directionalities at the outlet is presented. The uniformity of the concentration

distribution in the furnace can be explained via the Peclet number which is defined as $L_c v_z / D_{Sb}$, where L_c is the characteristic length which was chosen as the length of the boat. The maximum value of the diffusion coefficient within the furnace was calculated to be in the order of 10^{-3}, which results in somewhat low *P*é values (average of 49 for 500 sccm and 20 for 200 sccm at the exit of the furnace), meaning that within the furnace, diffusion assists advection, especially where local velocities are low. The profile of Sb vapor within the bulk flow has a similar distribution as shown by the streamlines in Figure 3.1.

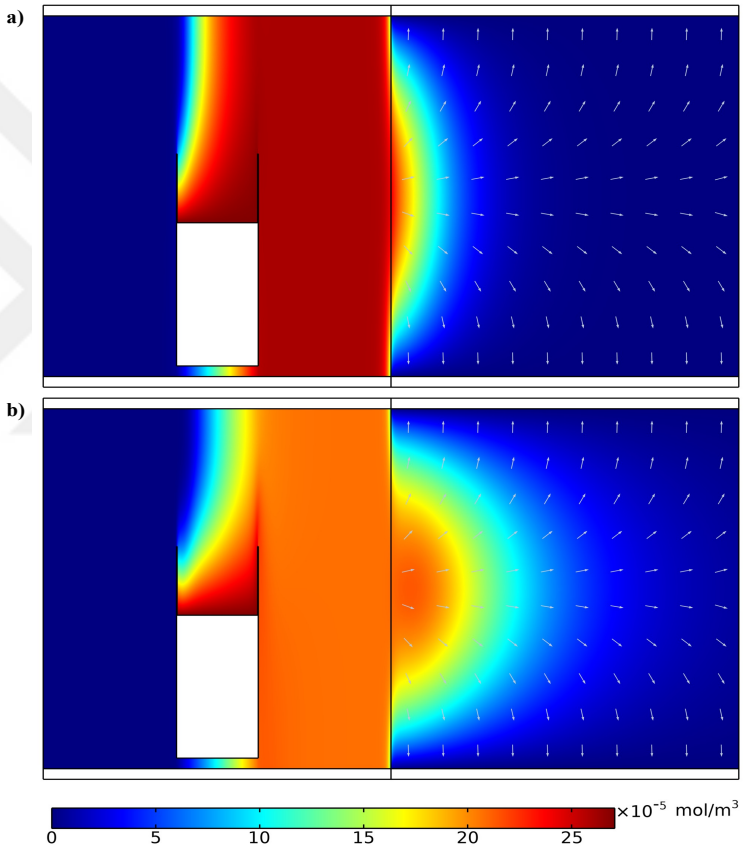

Figure 3.9. Concentration distribution map of Sb vapor under 200 and 500 sccm flow rate. a) 200 sccm b) 500 sccm. Light grey arrows indicate the total flux of Sb within the outlet of the system. A clear concentration boundary layer develops above the boat. Towards the exit of the furnace, the concentration of Sb becomes radially uniform. As the Sb vapor moves toward the exit of the ECG, concentration approaches zero. Note that there is only a very small drop in concentration before the exit of the furnace, verifying the expectations that stem from the Peclet number.

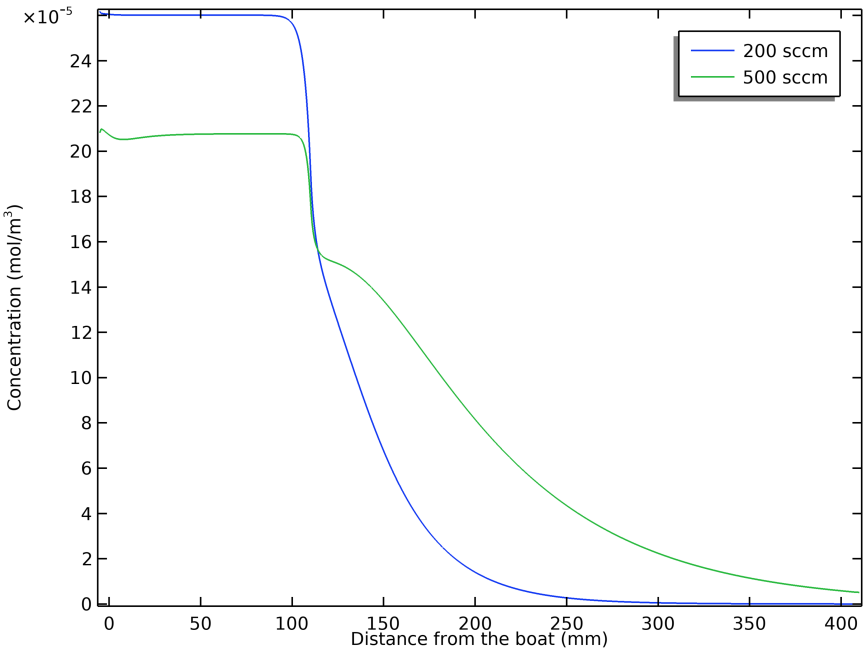

Figure 3.10. Sb vapor concentration averaged over the y-dimension as a function of flow rate. Averaged vapor concentration calculated as a function of distance from the boat, until the outlet. is taken at center of the tube and from the end of the boat to the outlet.

Figure 3.10 shows the decrease in vapor concentration on the central axis downstream of the boat. Higher flow velocities decrease the overall concentration in the furnace, but vapor content is better retained since diffusion time gets shorter. Flows above 500 sccm were not investigated since at 6 Torr operation pressure, flow rates are generally limited by the capacity of the vacuum pump. Generally, pumps that can retain few Torr pressure at flow rates of 1000 sccm or more are very large and expensive.

The contour map and the line graph of how the concentration of Sb vapor changes towards the outlet at the center gives a semi-qualitative picture of how fast the vapor starts to deplete. To better quantify the vapor losses in the system, mass flow rates and the yields were calculated for each configuration. Mass flow rate was calculated by taking the integral of the product of velocity and concentration, along with the depth factor, which is $\pi R_i/2$ with R_i being the inner radius (8.5 mm), at the exit of the ECG. This depth was taken to account for the outline cross sectional area of a cylindrical tube. The line integration was taken over the length of $2R_i$ and the

multiplication with the depth factor yields $\pi {R_i}^2$ which is the area of the outlet cross section.

$$\dot{m} = \frac{\pi R_i}{2} \int_0^{2R_i} \boldsymbol{u} C_{Sb} dy \tag{3.2}$$

For the yield, fluxes on different surfaces are taken into account. At the surface of the Sb metal in the boat, the total flux magnitude was evaluated because we are interested in all the Sb vapor that leaves the surface no matter the direction. At the outlet and its walls, normal total fluxes were evaluated to assess the diffusional losses. The yield is defined by taking the ratio of mass flow rate at the exit to the mass flow rate that comes from the solid Sb surface in the boat.

$$Y = \frac{\text{Flow rate of Sb at the ECG outlet}}{\text{Evaporation rate of Sb from the boat}} \times 100 \tag{3.3}$$

Table 3.1. Mass flow rates and yield of Sb vapor for two argon flow rates.

$\dot{V}$ [sccm]	$\dot{m}$ [mg/min]	Y [%]
200	2.11×10^{-5}	2.93×10^{-3}
500	1.93×10^{-2}	1.09

These results for mass flow rate and yield are far away from the benchmark (~1 mg/min and ~10% respectively), indicating that almost all vapor is converted to particles in reality, and the prediction of the observables, i.e. $\dot{m}$ and Y, does not appear to be possible without modeling particle formation. In order to assess whether the benchmark values for the observables can be obtained with the modeling framework developed, results of a simplistic model were first calculated before incorporating a detailed description of aerosol dynamics into the model. The simplistic approach relies on the change in diffusion coefficient during the particle formation and growth. Since the diffusion coefficient of a particle will rapidly decrease as it grows from a molecular cluster into a particle of few nm size, diffusional mass losses will decrease exponentially, which is explored in the following section.

3.4 Artificial Nucleation

In the ECG, particle formation occurs when the argon gas carries the Sb vapor to outside of the furnace. Therefore, right at the exit of the furnace, there must be a nucleation zone due to rapid cooling of the vapor. When particles form, diffusional mass losses decrease rapidly. In this subsection, nucleation is modeled artificially, by only changing the diffusion coefficient of the vapor gradually into the diffusion coefficient of the particles created by the ECG in the benchmark [62]. Determining the location of the zone in which the vapor is converted to particles requires the use of the equations of aerosol dynamics, however, before attempting to incorporate aerosol physics, which has considerable detail and involves significant computational difficulties, it is of interest to investigate whether $\dot{m}$ and Y could be increased to the orders of magnitude of the benchmark when particle formation is modeled artificially. To account for the location of the nucleation zone and the rate of growth, an empirical model was utilized to emulate particle formation by changing the diffusion coefficient as a function of distance away from the furnace.

Setting up this model requires the particle diffusion coefficient, D_p , which is described by the Stokes-Einstein equation. D_p is related to the particle size and the fluid properties through the friction coefficient, f, and fluid temperature, T, in this case, the temperature of the surrounding gas and vapor.

$$D_p = \frac{k_B T}{f} \tag{3.4}$$

$$f = \frac{3\pi\mu d_p}{C_c} \tag{3.5}$$

$$C_c = 1 + Kn_p \left[A_1 + A_2 \exp\left(-\frac{A_3}{Kn_p} \right) \right] \tag{3.6}$$

In the equations above, k_B is the Boltzmann constant, μ is the dynamic viscosity, C_c is the Cunningham slip correction factor, $\ell_p = k_B T/\sqrt{2}\sigma_{Ar} p$ is the mean free path of the particle, where σ_{Ar} is the collision cross-section of argon (3.8×10^{-19} m^2)[62] and d_p is the particle diameter. With C_c , the friction coefficient accommodates the

entire range of the particle Knudsen number, $Kn_p = 2\ell_p/d_p$, which is the ratio of the molecular free path, ℓ_p, to particle radius, $d_p/2$. The unitless constants A_1, A_2 and A_3 in C_c are given as 1.257, 0.4 and 1.10 respectively [47].

In the benchmark [37], particle sizes measured by TEM were below 50 nm. For the temperatures and pressure utilized in this work, an upper limit for the Kn_p was calculated using this upper particle size. For 50 nm size, 6 Torr pressure and ambient temperature, which are expected to yield the minimum Kn_p value, Kn_p was calculated as 191. Since this value is much greater than 1, particles are practically in the free molecular regime and the physics that apply to the transport and growth of particles are described by expressions that stem from kinetic theory.

The conversion from the vapor diffusion coefficient to particle diffusion coefficient at the exit of the furnace was represented with the following empirical equation.

$$D_{Sb} = D + \Phi_s(x - x_0, X)\big(D_p - D\big), \tag{3.7}$$

Here, D_{Sb} is the diffusion coefficient that depicts the change from vapor to particle. D is the vapor diffusion coefficient calculated with Equation 2.5. $\Phi_s(x - x_0, X)$ is the smoothed Heaviside step function, which changes from 0 to 1 at $x = x_0$across varying transition zone widths, shown by X, which is taken to be either 5, 10, 20 or 50 mm in the calculations. Details on the mathematical form of Φ_s and theselection of x_0 and X are given in Appendix E. In this approach, X refers to the distance throughout which the diffusion coefficient changes from that of vapor to particle after exiting the furnace, i.e. the nucleation and growth zone. The variation of D_{Sb} is illustrated in Figure 3.11. In this emulation of particle formation, diffusivity decreases by orders of magnitude from D to D_p, across a distance shown by X.

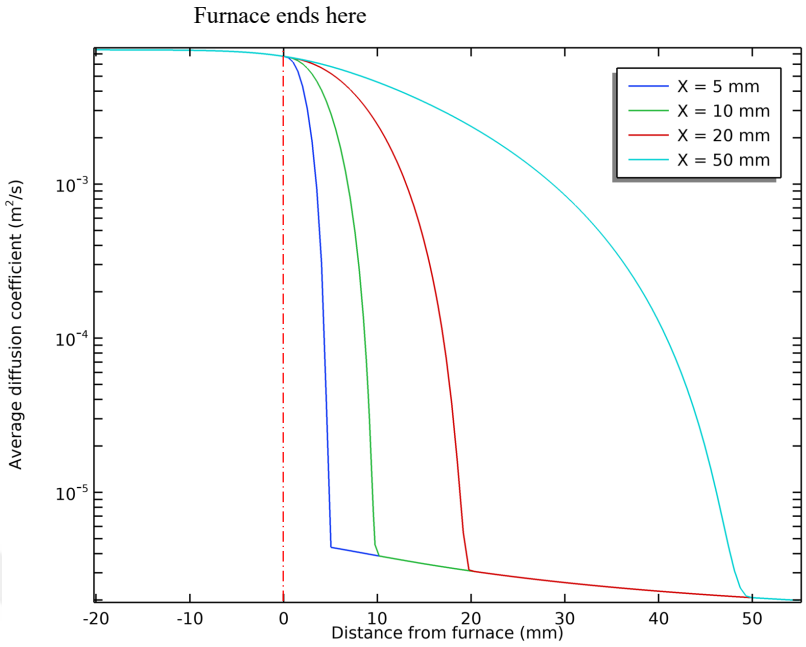

Figure 3.11. Transition from vapor diffusion to particle diffusion under 500 sccm flow at the central axis, plotted as a function of the transition zone width, *X*. As *X* increases, the conversion from vapor to particle occurs across a longer distance.

It can be seen from Figure 3.11 that there is a drastic change in the diffusion coefficient when vapor molecules convert into particles. This change also affects the Peclet number in the system, which determines the interplay of mass transport mechanisms. In order to present the effect of the change in diffusion coefficient on Pe, the ratio of linear velocity to diffusion coefficient in the system was plotted in Figure 3.12.

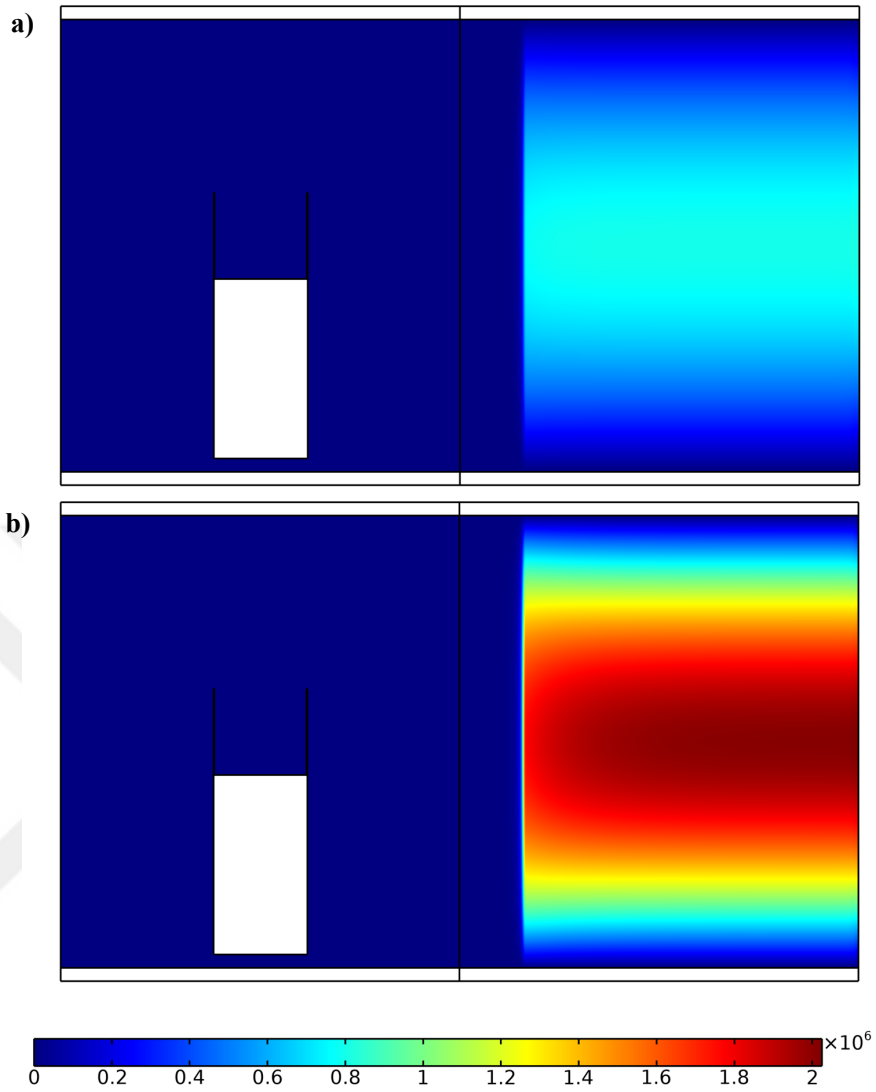

Figure 3.12. u/D map of the system with a transition size of 50 mm. a) 200 sccm b) 500 sccm Ar flow.

The uniform Sb distribution is dissipated mainly by two mechanisms: diffusion and advection. Velocity of the system changes due to the temperature change, modifying advection rates, and the diffusion coefficient changes due to particle formation, modifying the rates of diffusion. Therefore, the prominent transport mechanism is determined by the ratio of u and D. In Figure 3.12 it can be seen that when the particle formation is completed, Pe increases by a factor of 10^4, and thus advection becomes more prominent transport mechanism on the flow direction, and its strength is directly correlated with the flow rate of argon supplied

to the system. Converting the u/D values given in Figure 3.12 requires a length scale. As done in the previous subsection, the length scale was taken as the length of the boat. Thus, Pe increases from 20 to 5×10^4 at 200 sccm, and from 70 to 10^5 at 500 sccm, as the vapor was converted into particles in this artificial nucleation model. The values of Pe at two different flow rates show the direct correlation with flow velocities.

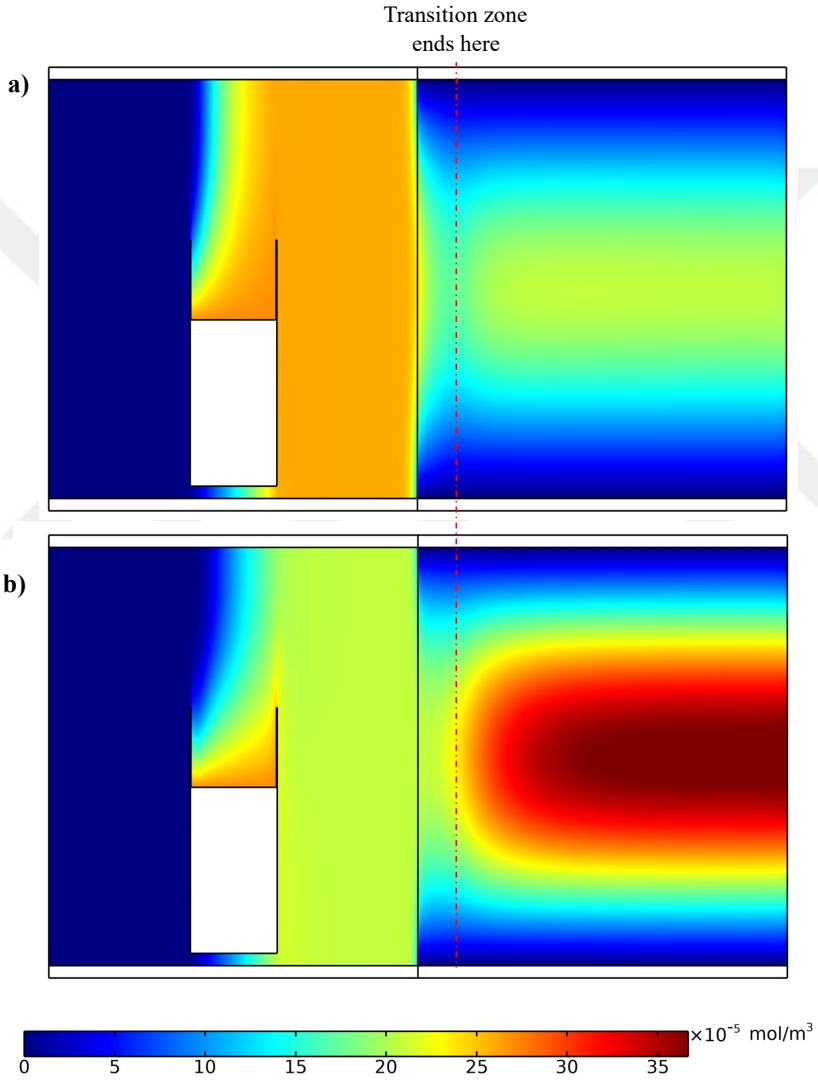

Figure 3.13. Concentration distribution of Sb with the transition size of 50 mm. a) 200 sccm b) 500 sccm. In both cases the concentration reaches uniformity in the furnace, as shown before in Figure 3.9. Due to the lower diffusion coefficient of the particles, the convective movement of Sb particles is the dominant transport mechanism which causes a strong flow of mass towards the exit.

Figures 3.11 and 3.12 show that at the exit of the furnace, advection becomes the prominent method of mass transport. As soon as the Sb vapor exits the furnace, nucleation starts according to the empirical description, lowering the diffusion coefficient and making the convection dominant transport mechanism in the system. However, due to the drop in temperature, the velocity decreases as well, but not as drastically as diffusivity. This results in lowered advection rates and subsequent accumulation of Sb particles at the centerline as shown in Figure 3.13. The transition zone was taken as specifically as 50 mm and this is expected to be acceptable, since this zone also corresponds to the zone in which the tube of the ECG cools down to temperatures nearby the ambient, leading to the aforementioned dynamics in diffusion and advection.

With nucleation being simulated artificially, it can be inferred from Table 3.2 that the experimentally obtained yield and mass flow rates have been approached to the order of magnitude. An exact match with the experimental data could have been obtained by further adjusting the transition zone, but such an effort holds little value since the approach would not be predictive for different operation conditions due to the empiricism involved. However, results indicate that to have a model suitable for designing an ECG with the desired performance, an aerosol dynamics model must be developed, and it should be solved along with fluid mechanics, heat transfer and vapor transport that is present in the ECG. The order-of-magnitude agreement obtained in the observable quantities via the contour maps shown in Figure 3.13 suggest that the aerosol model should yield a map that looks similar to the ones in Figure 3.13, but only for the region downstream of the dotted line that shows the transition zone.

Table 3.2. Mass flow rates and yield for two argon flow rates of Sb with a diffusion transition size of 50 mm.

$\dot{V}$ [sccm]	$\dot{m}$ [mg/min]	Y [%]
200	0.19	21.68
500	0.87	49.33

CHAPTER 4

AEROSOL DYNAMICS

In the previous chapter, the need for the development of an aerosol model to depict the particle formation in the system was demonstrated. Only with such a model, the output and yield of the ECG can be predicted. The aerosol model is based on the general dynamic equation, which incorporates all the mechanisms involved in the particle formation and transport.

4.1 General Dynamics Equation

The general dynamics equation (GDE, Equation 4.1) is the governing equation for the aerosol dynamics. For a continuous particle size distribution n_v defined with respect to particle volume v_p, where n_v has the SI units of [# (m^{-3} system volume) (m^{-3} particle volume)], the GDE describes the evolution of n_v with respect to time and position, and through advection, diffusion, surface growth, coagulation (abbreviated as "*coag*" below) and migration [47].

$$\frac{\partial n_v}{\partial t} + \boldsymbol{\nabla} \cdot n_v \boldsymbol{u} = \boldsymbol{\nabla} \cdot D \boldsymbol{\nabla} n_v + \left[\frac{\partial n_v}{\partial t^*}\right]_{\text{growth}} + \left[\frac{\partial n_v}{\partial t^*}\right]_{\text{coag}} - \boldsymbol{\nabla} \cdot \boldsymbol{c} n_v \qquad (4.1)$$

In this equation, $\boldsymbol{u}$ is the velocity vector of the carrier fluid, which is argon in this case, and the flow field that describes $\boldsymbol{u}$ was presented in the previous chapter. As given in Equation 3.4, D_p is the particle diffusion coefficient and it is a function of particle volume[7]. $\boldsymbol{c}$ is the particle velocity resulting from external forces, and for our case, it will be assumed to be solely described by thermophoresis. In this equation, n_v is defined on the particle size range $\left[v_p^*, \infty\right)$, where v_p^* is the critical nucleus size

[7] Particles formed during this process are considered to be spherical. A simple the conversion from volume of the particle to diameter can be obtained via this relation: $v_p = (\pi/6){d_p}^3$.

[47]. v_p^* describes the smallest size that is thermodynamically stable in the system which is also referred to as the critical nucleus size and is calculated by $d_p^* = 4\gamma v_m / k_B T \ln S$, where γ is the surface tension of the Sb droplets, v_m is the molecular volume of the particle and S is the saturation ratio which is the ratio of partial pressure of Sb to its vapor pressure at given conditions [47]. Sizes smaller than v_p^*, that is, small molecular clusters, are generally not included in n_v. It can be shown below that in our case, v_p^* is a dimer of Sb vapor, i.e. $v_p^* = 2v_m$ where v_m is the molecular volume of Sb vapor. Therefore, the smallest species other than the monoatomic vapor.

In Equation 4.1, the first term is not used for the calculations presented in this chapter since only steady state is considered. The advection and diffusion terms given in the same equation are similar to the terms given in Equation 2.17 and Equation 2.18, but the growth and coagulation terms are unique to the GDE. The time variable t^* present in these terms (in Equation 4.1) denote either time or flow time, therefore these terms are retained in both steady or transient calculations. The growth term represents the change in n_v due to condensation or evaporation, and it is generally described as:

$$\left[\frac{\partial n_v}{\partial t^*}\right]_{\text{growth}} = \frac{\partial I}{\partial v_p}. \tag{4.2}$$

In Equation 4.2, I is the droplet current and it stands for the number flux in the particle size coordinate, where as $\partial I / \partial v_p$ describes the transport in and out of a size v_p in n_v. I depends on the mode of growth and it will be detailed in the next subsection. The coagulation term is described with Smoluchovski's equation:

$$\left[\frac{\partial n_v}{\partial t}\right]_{\text{coag}} = \frac{1}{2}\int_0^{v_p} \beta(\tilde{v}_p, v_p - \tilde{v}_p) n_v(\tilde{v}_p) n_v(v_p - \tilde{v}_p) d\tilde{v}_p - \int_0^{\infty} \beta(v_p, \tilde{v}_p) n_v(v_p) n_v(\tilde{v}_p) d\tilde{v}_p \tag{4.3}$$

The first term on the RHS describes the influx of particles into size v_p and the second term describes loss from size v_p due to collision with particles of any size. In aerosol dynamics, fragmentation is rare, therefore coagulational growth is unidirectional [47] . β is the collision frequency function which depend on the sizes of colliding particles. High Kn_p numbers that arise in this work due to low pressure and small particles (<50 nm, see below) allow a description based on kinetic theory to be valid for growth processes, as in diffusion (see section 3.4). For coagulation in the free molecular regime, β can be derived as [47]:

$$\beta(v_p, \tilde{v}_p) = \left(\frac{3}{4\pi}\right)^{1/6} \left(\frac{6kT}{\rho_p}\right)^{1/2} \left(\frac{1}{v_p} + \frac{1}{\tilde{v}_p}\right)^{1/2} \left(v_p^{1/3} + \tilde{v}_p^{1/3}\right)^2 \tag{4.4}$$

After the substitutions, the GDE becomes:

$$\begin{aligned} &\frac{\partial n_v}{\partial t} + \boldsymbol{\nabla} \cdot n_v \boldsymbol{u} + \frac{\partial I}{\partial v_p} = \boldsymbol{\nabla} \cdot D \boldsymbol{\nabla} n_v + \\ &\frac{1}{2}\int_0^{v_p} \beta(\tilde{v}_p, v_p - \tilde{v}_p) n_v(\tilde{v}_p) n_v(v_p - \tilde{v}_p) d\tilde{v}_p \\ &-\int_0^{\infty} \beta(v_p, \tilde{v}_p) n_v(v_p) n_v(\tilde{v}_p) d\tilde{v}_p - \boldsymbol{\nabla} \cdot \boldsymbol{c} n_v \end{aligned} \tag{4.5}$$

This is a five-dimensional (3 spatial coordinates, time, and particle size), nonlinear integrodifferential equation that requires vast computational resources even when reduced to a three-dimensional form on a 2D spatial domain at steady state. Instead of attacking this problem in its full form, the GDE will be simplified in the next subsection.

4.2 Lognormal Model of GDE

Evolution of the full-size distribution as described by the GDE (Equation 4.1) contains a very large amount of information, and all of this information is rarely desired. In most cases, the number density, the mean size, and the width of the size distribution, i.e. polydispersity, is enough to characterize the aerosol. However, to

reduce the amount of information buried in the GDE, an *a priori* assumption on the shape of the size distribution is required. Here, a lognormal approach is developed for simplifying the GDE. Lognormal models are common in aerosol dynamics [78, 79], especially since the lognormal distribution can describe particle size distributions in wide variety of processes [80-82]. By assuming that the size distribution always stays lognormal, it is possible to reduce the GDE into three separate equations, each dedicated to the evolution of a moment of the size distribution. The general definition of a moment of nth order with respect to particle volume when applied to a size distribution function is given below:

$$M_k(\mathbf{r}, t) = \int_0^\infty n_v v_p^k d(v_p) \tag{4.6}$$

In this equation M_k represents the moment of order k, which is a function of time and space. When applied to a size distribution, some of the moments have a distinct physical meaning. For example, the zero-order moment, or the zeroth moment (M_0), represents the total particle number concentration of the aerosol. The first moment (M_1) represents the particle volume concentration, or the volume fraction, but second moment has no physical meaning. We will show that with a few assumptions, the GDE can be integrated, and closure can be obtained through the use of these three moments.

In order to convert the GDE into equations of moments, all terms in the GDE must be subjected to the application of the relevant moment operator of order k, which can be shown as:

$$_m\langle\ \rangle_k = \int_0^\infty \ v_p^k d(v_p) \tag{4.7}$$

In the following subsections, moment integrals are applied to each term given in Equation 4.1. The system of interest is at steady state; therefore, the transient term is neglected. Below, the analysis for each term in the GDE is given with the aim of developing general moment equations that cover all the transport and growth

mechanisms given in the GDE for large Kn_p. This development is motivated with the lack of such general equations and their explicit derivations in literature.

4.2.1 Advection Term

The term representing advection in Equation 4.1 is $\nabla \cdot n\mathbf{u}$.

$$\nabla \cdot n_v \boldsymbol{u} = \frac{\partial}{\partial x}(n_v u_x) + \frac{\partial}{\partial y}(n_v u_y) + \frac{\partial}{\partial z}(n_v u_z) \tag{4.8}$$

By applying the chain rule, the derivatives of size distribution functions can be separated:

$$\boldsymbol{\nabla} \cdot n_v \boldsymbol{u} = u_x \frac{\partial n_v}{\partial x} + u_y \frac{\partial n_v}{\partial y} + u_z \frac{\partial n_v}{\partial z} + n_v(\boldsymbol{\nabla} \cdot \boldsymbol{u}) \tag{4.9}$$

Recollecting the terms for the size distribution function we get the following expression for the advection term:

$$\boldsymbol{\nabla} \cdot n_v \boldsymbol{u} = \boldsymbol{u} \cdot \boldsymbol{\nabla} n_v + n_v(\boldsymbol{\nabla} \cdot \boldsymbol{u}) \tag{4.10}$$

The divergence of velocity $(\boldsymbol{\nabla} \cdot \boldsymbol{u})$ cannot be neglected since the flow in the system is compressible. The moment operator is applied to the form of the advection term given on the RHS of the equation above, resulting in the following expressions.

Zeroth moment:

$$\int_{v_p^*}^{\infty} (\boldsymbol{u} \cdot \boldsymbol{\nabla} n_v) dv_p = \boldsymbol{u} \cdot \boldsymbol{\nabla} \int_{v_p^*}^{\infty} n_v dv_p = \boldsymbol{u} \cdot \boldsymbol{\nabla} M_0 \tag{4.11}$$

$$\int_{v_p^*}^{\infty} n_v (\boldsymbol{\nabla} \cdot \boldsymbol{u}) dv_p = M_0 (\boldsymbol{\nabla} \cdot \boldsymbol{u}) \tag{4.12}$$

Hence:

$$\int_{v_p^*}^{\infty} (\boldsymbol{\nabla} \cdot n_v \boldsymbol{u}) dv_p = \boldsymbol{u} \cdot \boldsymbol{\nabla} M_0 + M_0 (\boldsymbol{\nabla} \cdot \boldsymbol{u}) \tag{4.13}$$

First moment:

$$\int_{v_p^*}^{\infty}(\boldsymbol{u}\cdot\boldsymbol{\nabla}n_v)v_p dv_p = \boldsymbol{u}\cdot\boldsymbol{\nabla}\int_{v_p^*}^{\infty}n_v v_p dv_p = \boldsymbol{u}\cdot\boldsymbol{\nabla}M_1 \tag{4.14}$$

$$\int_{v_p^*}^{\infty}n_v(\boldsymbol{\nabla}\cdot\boldsymbol{u})v_p dv_p = M_1(\boldsymbol{\nabla}\cdot\boldsymbol{u}) \tag{4.15}$$

Hence:

$$\int_{v_p^*}^{\infty}(\boldsymbol{\nabla}\cdot n_v\boldsymbol{u})v_p dv_p = \boldsymbol{u}\cdot\boldsymbol{\nabla}M_1 + M_1(\boldsymbol{\nabla}\cdot\boldsymbol{u}) \tag{4.16}$$

Second moment:

$$\int_{v_p^*}^{\infty}(\boldsymbol{u}\cdot\boldsymbol{\nabla}n_v){v_p}^2 dv_p = \boldsymbol{u}\cdot\boldsymbol{\nabla}\int_{v_p^*}^{\infty}n_v{v_p}^2 dv_p = \boldsymbol{u}\cdot\boldsymbol{\nabla}M_2 \tag{4.17}$$

$$\int_{v_p^*}^{\infty}n_v(\boldsymbol{\nabla}\cdot\boldsymbol{u}){v_p}^2 dv_p = M_2(\boldsymbol{\nabla}\cdot\boldsymbol{u}) \tag{4.18}$$

Hence:

$$\int_{v_p^*}^{\infty}(\boldsymbol{\nabla}\cdot n_v\boldsymbol{u}){v_p}^2 dv_p = \boldsymbol{u}\cdot\boldsymbol{\nabla}M_2 + M_2(\boldsymbol{\nabla}\cdot\boldsymbol{u}) \tag{4.19}$$

4.2.2 Surface Growth Term

The term representing the surface growth is denoted by $\partial I/\partial v_p$. In the ECG, particles grow by condensation. The Kn_p values that arise result in the description of condensation and evaporation in the free molecular range to be valid [47].

$$\frac{\partial I}{\partial v_p} = \frac{\partial(n_v G)}{\partial v_p} \tag{4.20}$$

$$G = \frac{dv_p}{dt} = \frac{\alpha(p-p_s)v_m}{\sqrt{2\pi\mu k_B T}}(36\pi)^{\frac{1}{3}}{v_p}^{\frac{1}{3}} = \theta(T)(S-1){v_p}^{\frac{1}{3}} \tag{4.21}$$

where,

$$\theta(T) = \frac{\alpha(36\pi)^{\frac{1}{3}} p_s}{\sqrt{2\pi m k_B T}} \tag{4.22}$$

$$S = \frac{C_{Sb} RT}{p_s} \tag{4.23}$$

Above, Kelvin effect in the growth was neglected since it prevents closure in the development of the lognormal model. Equation 4.21 comes from kinetic theory, and S in Equation 4.23 is the saturation ratio, which is the ratio of monomer partial pressure to the equilibrium vapor pressure at the local temperature. α is the mass accommodation coefficient and it was set to 1. The integration of the surface growth term according to the general definition of the zeroth moment yields:

$$\int_{v_p^*}^{\infty} \frac{\partial I}{\partial v_p} dv_p = -I|_{v_p^*} + I|_{\infty} \tag{4.24}$$

The first term on the RHS equals to the nucleation rate (I_0) described by the classical nucleation theory in this work, and the second term on the RHS equals to zero as there are no particles of infinite size. The nucleation rate is defined as following [47];

$$I_0 = 2\left[\frac{\mathrm{p}_1}{2\pi m k_B T}\right]\left(n_1 v_m^{2/3}\right)\left[\frac{\gamma\, v_m^{2/3}}{k_B T}\right]^{1/2} exp\left[-\frac{16\pi\, \gamma^3\, v_m^2}{3(k_B T)^3 (lnS)^2}\right] \tag{4.25}$$

where, p_1 is the monomer partial pressure (equal to partial pressure of Sb vapor), m is the atomic weight, n_1 is the monomer number concentration, $n_1 = C_{Sb} N_A$, where N_A is the Avogadro constant. v_m is the molecular volume of the particle and γ is the surface tension[8] of the antimony droplets[9]. Nucleation rate has units of $m^{-3}s^{-1}$

Integration for the first moment of the surface growth term yields:

$$\int_{v_p^*}^{\infty} \frac{\partial I}{\partial v_p} v_p dv_p = \int_{v_p^*}^{\infty} v_p \frac{\partial}{\partial v_p}(n_v G) dv_p \tag{4.26}$$

Applying the chain rule inversely yields:

[8] $\gamma\ [mJ/m^2] = 372 - 0.0276(T - T_m)$ where T_m is the melting point temperature in K [66].
[9] The melting point decreases with increasing droplet size[47].

$$\int_{v_p^*}^{\infty}\left[\frac{\partial}{\partial v_p}\left(v_p n_v G\right)-n_v G\right]dv_p = v_p n_v G|_{\infty} - v_p n_v G|_{v_p^*} - \int_{v_p^*}^{\infty} n_v G dv_p \quad (4.27)$$

The first term on the RHS in Equation 4.27 equals to zero for the infinitely sized particle. Note that:

$$v_p n_v G|_{v_p^*} = \left(v_p I\right)|_{v_p^*} = v_p^* I_0 \quad (4.28)$$

By substituting the definition of G from Equation 4.21, the integral on the RHS of Equation 4.27 can be evaluated.

$$\int_{v_p^*}^{\infty} n_v G dv_p = \theta(T)(S-1)M_{\frac{2}{3}} \quad (4.29)$$

Therefore, the first moment integral equals to:

$$\int_{v_p^*}^{\infty}\frac{\partial I}{\partial v_p}v_p dv_p = -2v_m I_0 - \theta(T)(S-1)M_{\frac{2}{3}} \quad (4.30)$$

The integral of the second moment can be evaluated similarly:

$$\int_{v_p^*}^{\infty}\frac{\partial I}{\partial v_p}{v_p}^2 dv_p = \int_{v_p^*}^{\infty}\left[\frac{\partial}{\partial v_p}\left({v_p}^2 n_v G\right)-2v_p n_v G\right]dv_p \quad (4.31)$$

$$= -{v_p^*}^2 I_0 - \theta(T)(S-1)M_{\frac{5}{3}} \quad (4.32)$$

4.2.3 Diffusion Term

The diffusion term in the GDE is denoted as $\boldsymbol{\nabla}\cdot D\boldsymbol{\nabla}n_v$ and the equation for the particle diffusion coefficient was given by Equation 3.4 in the artificial nucleation section. However, due to the use of the Cunningham slip correction factor in the Stokes-Einstein equation, the integrals cannot be solved analytically and expressions for moments (M_0, M_1 and M_2) cannot be achieved in explicit form. Therefore, some approximations must be made to put the Stokes-Einstein equation in an acceptable power-law form, so that the moment integrals can be evaluated. Series expansion results in the following form of the diffusion coefficient that is accurate for large Kn_p, therefore directly applicable in this model:

$$D \cong \left(\frac{\pi}{162}\right)^{\frac{1}{3}} \frac{k_B T}{\mu} \left(\frac{1}{{v_p}^{\frac{1}{3}}} + \frac{2.671 \ell_p}{{v_p}^{\frac{2}{3}}} \right) \tag{4.33}$$

Details of this derivation can be found in Appendix H. The moments of the diffusion term can now be evaluated by using Equation 4.33. Integration for the zeroth moment results in:

$$\begin{aligned} &\int_{v_p^*}^{\infty} (\boldsymbol{\nabla} \cdot D \boldsymbol{\nabla} n_v) dv_p \\ &\qquad = \int_{v_p^*}^{\infty} \frac{\partial}{\partial x}\left(D \frac{\partial n_v}{\partial x}\right) dv_p + \int_{v_p^*}^{\infty} \frac{\partial}{\partial y}\left(D \frac{\partial n_v}{\partial y}\right) dv_p \\ &\qquad + \int_{v_p^*}^{\infty} \frac{\partial}{\partial z}\left(D \frac{\partial n_v}{\partial z}\right) dv_p \end{aligned} \tag{4.34}$$

For the term on x-axis:

$$\begin{aligned} \int_{v_p^*}^{\infty} \frac{\partial}{\partial x}\left(D \frac{\partial n_v}{\partial x}\right) dv_p &= \frac{\partial}{\partial x} \int_{v_p^*}^{\infty} D \frac{\partial n_v}{\partial x} dv_p \\ &= \frac{\partial}{\partial x} \int_{v_p^*}^{\infty} \left[\frac{\partial}{\partial x} (D n_v) - n_v \frac{\partial D}{\partial x} \right] dv_p \end{aligned} \tag{4.35}$$

Similar forms follow for the y and z components for the diffusion term. In the definition of the diffusion coefficient, the mean free path and temperature are position dependent. Therefore, chain rule must be applied to Equation 4.35 in order to evaluate the integrals.

$$\int_{v_p^*}^{\infty} \frac{\partial}{\partial x}\left(D\frac{\partial n_v}{\partial x}\right) dv_p$$

$$= \frac{\partial}{\partial x}\left\{\frac{\partial}{\partial x}\left[\left(\frac{\pi}{162}\right)^{\frac{1}{3}} \frac{k_B T}{\mu}\left(\int_{v_p^*}^{\infty} {v_p}^{-\frac{1}{3}} n_v \, dv_p\right.\right.\right.$$

$$\left.\left.\left. + 2.671\ell_p \int_{v_p^*}^{\infty} {v_p}^{-\frac{2}{3}} n_v \, dv_p\right)\right]\right. \tag{4.36}$$

$$- \left[\left(\frac{\pi}{162}\right)^{\frac{1}{3}} k_B \frac{\partial}{\partial x}\left(\frac{T}{\mu}\right) \int_{v_p^*}^{\infty} {v_p}^{-\frac{1}{3}} n_v \, dv_p\right.$$

$$\left.\left. + \left(\frac{\pi}{162}\right)^{\frac{1}{3}} k_B \frac{\partial}{\partial x}\left(\frac{T\ell_p}{\mu}\right) 2.671 \int_{v_p^*}^{\infty} {v_p}^{-\frac{2}{3}} n_v \, dv_p\right]\right\}$$

Here, the first derivative with respect to x was taken out of the integral and the variation of v_p^* with respect to x was neglected. This detail can be incorporated into the model equations, however, since $v_p^* = 2v_m$ holds within the majority of the particle-laden zone because of very high S. Therefore, the integrals in the Equation 4.36 yield the following moment expressions:

$$\int_{v_p^*}^{\infty} {v_p}^{-\frac{1}{3}} n_v \, dv_p = M_{-\frac{1}{3}} \tag{4.37}$$

$$\int_{v_p^*}^{\infty} {v_p}^{-\frac{2}{3}} n_v \, dv_p = 2.671\ell_p M_{-\frac{2}{3}} \tag{4.38}$$

$$\int_{v_p^*}^{\infty} {v_p}^{-\frac{2}{3}} n_v \, dv_p = M_{-\frac{2}{3}} \tag{4.39}$$

and substitution of Equations 4.37-4.39 into Equation 4.36 results in:

$$\int_{v_p^*}^{\infty} \frac{\partial}{\partial x}\left(D\frac{\partial n_v}{\partial x}\right) dv_p$$
$$= \frac{\partial}{\partial x}\left\{\frac{\partial}{\partial x}\left[\left(\frac{\pi}{162}\right)^{\frac{1}{3}} \frac{k_B T}{\mu}\left(M_{-\frac{1}{3}} + 2.671\ell_p M_{-\frac{2}{3}}\right)\right]\right.$$
$$- \left[\left(\frac{\pi}{162}\right)^{\frac{1}{3}} k_B \frac{\partial}{\partial x}\left(\frac{T}{\mu}\right) M_{-\frac{1}{3}}\right. \tag{4.40}$$
$$\left.\left. + \left(\frac{\pi}{162}\right)^{\frac{1}{3}} k_B \frac{\partial}{\partial x}\left(\frac{T\ell_p}{\mu}\right) 2.671 M_{-\frac{2}{3}}\right]\right\}$$

The second set of brackets brings a formidable mathematical complexity to the expression, and therefore it is neglected to put the final equations in simpler form. Interestingly, an equivalent term was neglected in literature before, without providing any explanation [57]. With this simplification, the integral in x-direction finally becomes.

$$\int_{v_p^*}^{\infty} \frac{\partial}{\partial x}\left(D\frac{\partial n_v}{\partial x}\right) dv_p = \left(\frac{\pi}{162}\right)^{\frac{1}{3}} \frac{k_B T}{\mu} \frac{\partial^2}{\partial x^2}\left(M_{-\frac{1}{3}} + 2.671\ell_p M_{-\frac{2}{3}}\right) \tag{4.41}$$

The equations for the y and z coordinates follow the same procedure. The first and second moments are also evaluated following the same procedure and their integrals explicitly evaluated for x-direction are given below:

$$\int_{v_p^*}^{\infty} \frac{\partial}{\partial x}\left(D\frac{\partial n_v}{\partial x}\right) v_p\, dv_p = \left(\frac{\pi}{162}\right)^{\frac{1}{3}} \frac{k_B T}{\mu} \frac{\partial^2}{\partial x^2}\left(M_{\frac{2}{3}} + 2.671\ell_p M_{\frac{1}{3}}\right) \tag{4.42}$$

$$\int_{v_p^*}^{\infty} \frac{\partial}{\partial x}\left(D\frac{\partial n_v}{\partial x}\right) {v_p}^2 dv_p = \left(\frac{\pi}{162}\right)^{\frac{1}{3}} \frac{k_B T}{\mu} \frac{\partial^2}{\partial x^2}\left(M_{\frac{5}{3}} + 2.671\ell_p M_{\frac{4}{3}}\right) \tag{4.43}$$

Evaluation of the moments and their integrals for the y and z direction were evaluated in the same manner, they yield the same results. Simply, replacement of the partial differential in the x direction with three-dimensional gradient operator gives the final and compact result for the diffusion term in terms of moments, since x, y and z does not appear explicitly in the equations.

$$\int_{v_p^*}^{\infty} \boldsymbol{\nabla}\left(D\frac{\partial n_v}{\partial x}\right) dv_p = \left(\frac{\pi}{162}\right)^{\frac{1}{3}} \frac{k_B T}{\mu} \boldsymbol{\nabla}^2 \left(M_{-\frac{1}{3}} + 2.671\ell_p M_{-\frac{2}{3}}\right) \tag{4.44}$$

$$\int_{v_p^*}^{\infty} \boldsymbol{\nabla}\left(D\frac{\partial n_v}{\partial x}\right) v_p\, dv_p = \left(\frac{\pi}{162}\right)^{\frac{1}{3}} \frac{k_B T}{\mu} \boldsymbol{\nabla}^2 \left(M_{\frac{2}{3}} + 2.671\ell_p M_{\frac{1}{3}}\right) \tag{4.45}$$

$$\int_{v_p^*}^{\infty} \boldsymbol{\nabla}\left(D\frac{\partial n_v}{\partial x}\right) {v_p}^2 dv_p = \left(\frac{\pi}{162}\right)^{\frac{1}{3}} \frac{k_B T}{\mu} \boldsymbol{\nabla}^2 \left(M_{\frac{5}{3}} + 2.671\ell_p M_{\frac{4}{3}}\right) \tag{4.46}$$

4.2.4 Coagulation Term

The moment integrals for coagulation in the free molecular regime were evaluated and moment equations were previously derived in approximate form by Lee, Chen and Gieseke previously [83]. We use their equations directly:

$$[\text{coag}]_{LN}^{(0)} = -b_0 K \left(M_0^{\frac{151}{72}} M_1^{-\frac{13}{36}} M_2^{\frac{19}{72}} + 2M_0^{\frac{131}{72}} M_1^{\frac{7}{36}} M_2^{-\frac{1}{72}} + M_0^{\frac{127}{72}} M_1^{\frac{11}{36}} M_2^{-\frac{5}{72}} \right) \tag{4.47}$$

$$[\text{coag}]_{LN}^{(2)} = 2b_2 K \left(M_0^{\frac{19}{72}} M_1^{\frac{47}{36}} M_2^{\frac{31}{72}} + 2M_0^{-\frac{1}{72}} M_1^{\frac{67}{36}} M_2^{\frac{11}{72}} + M_0^{-\frac{5}{72}} M_1^{\frac{71}{36}} M_2^{\frac{7}{72}} \right) \tag{4.48}$$

$$b_0 = 0.633 + 0.092{\sigma_g}^2 - 0.022{\sigma_g}^3 \tag{4.49}$$

$$b_2 = 0.39 + 0.5\sigma_g - 0.214{\sigma_g}^2 + 0.029{\sigma_g}^3 \tag{4.50}$$

$$K = \left(\frac{3}{4\pi}\right)^{\frac{1}{6}} \left(\frac{6k_B T}{\rho_p}\right) \tag{4.51}$$

K is the coagulation constant for free molecular regime [84]. b_0 and b_2 are interpolation functions required for closure of the integrated form of the Smoluchowski equation.

4.2.5 Thermophoresis Term

The term for the external forces ($\boldsymbol{\nabla} \cdot \mathbf{c} n_k$) is thermophoresis for our case; which is the force that transports the particles due to a temperature gradient. Particles at higher temperature region are pushed by the more energetic molecules, and they are transported down the temperature gradient [85]. This is important as the aerosol leaving the furnace is at high temperature and the walls of the outlet tube is much colder, resulting in the transport of particles towards the walls by thermophoresis and causing more deposition. Consequently, $\mathbf{c}$ in Equation 4.1 is defined as thermophoretic velocity and it is derived from the kinetic theory as follows[47];

$$\mathbf{c}_T = \frac{-3\nu \boldsymbol{\nabla} T}{4\left(1 + \frac{\pi\alpha}{8}\right) T} \tag{4.52}$$

where ν is the kinematic viscosity of the surrounding gas and α_T is the thermal accommodation coefficient. In Equation 52, Thermophoretic velocity is independent of particle size, therefore the moment integrals can simply be evaluated and the following expressions are obtained:

$$\int_{v_p^*}^{\infty} \boldsymbol{\nabla} \cdot \mathbf{c}_T n_v dv_p = \boldsymbol{\nabla} \cdot \mathbf{c}_T M_0 \tag{4.53}$$

$$\int_{v_p^*}^{\infty} (\boldsymbol{\nabla} \cdot \mathbf{c}_T n_v) v_p dv_p = \boldsymbol{\nabla} \cdot \mathbf{c}_T M_1 \tag{4.54}$$

$$\int_{v_p^*}^{\infty} (\boldsymbol{\nabla} \cdot \mathbf{c}_T n_v) {v_p}^2 dv_p = \boldsymbol{\nabla} \cdot \mathbf{c}_T M_2 \tag{4.55}$$

4.2.6 Hatch-Choate Equations

The moments with fractional orders cannot be not readily computed in a lognormal model, and they must be converted into the orders of zeroth, first and second. This conversion is done via the Hatch-Choate equations. For any k[th] order[57, 83];

$$M_k = M_0 v_g^k \exp\left(\frac{9}{2} k^2 \ln^2 \sigma_g\right) \tag{4.56}$$

$$\ln^2 \sigma_g = \frac{1}{9} \ln\left(\frac{M_0 M_2}{M_1^2}\right) \tag{4.57}$$

$$v_g = M_0^{-\frac{3}{2}} M_1^2 M_2^{-\frac{1}{2}} \tag{4.58}$$

where v_g is the geometric average particle volume, σ_g is the geometric standard deviation. By substituting Equations 4.57 and 4.58 into Equation 4.56, the fractional ordered moments can be converted to M_0, M_1 and M_2:

$$M_k = M_0^{\frac{k^2-3k+2}{2}} M_1^{2k-k^2} M_2^{\frac{k^2-k}{2}} \tag{4.59}$$

With this equation, fractional moments that appear in the derived expressions above can be converted to a multiplication of M_0, M_1 and M_2 as follows:

$$M_{\frac{2}{3}} = M_0^{\frac{2}{9}} M_1^{\frac{8}{9}} M_2^{-\frac{1}{9}} \tag{4.60}$$

$$M_{\frac{5}{3}} = M_0^{-\frac{1}{9}} M_1^{\frac{5}{9}} M_2^{\frac{5}{9}} \tag{4.61}$$

$$M_{-\frac{1}{3}} = M_0^{\frac{14}{9}} M_1^{-\frac{7}{9}} M_2^{\frac{2}{9}} \tag{4.62}$$

$$M_{-\frac{2}{3}} = M_0^{\frac{20}{9}} M_1^{-\frac{16}{9}} M_2^{\frac{5}{9}} \tag{4.63}$$

$$M_{\frac{1}{3}} = M_0^{\frac{5}{9}} M_1^{\frac{5}{9}} M_2^{-\frac{1}{9}} \tag{4.64}$$

$$M_{\frac{4}{3}} = M_0^{-\frac{1}{9}} M_1^{\frac{8}{9}} M_2^{\frac{2}{9}} \tag{4.65}$$

4.2.7 GDE in Moment Form

By using the moment expressions developed above, along with the Hatch-Choate equations, the lognormal equations for zeroth, first and second order moments become the following set of equations:

Zeroth moment:

$$\begin{aligned} &\boldsymbol{u}\cdot\boldsymbol{\nabla}M_0 + M_0(\boldsymbol{\nabla}\cdot\boldsymbol{u}) - I_0 \\ &\qquad = D_1(T)\boldsymbol{\nabla}^2\left(M_0^{\frac{14}{9}} M_1^{-\frac{7}{9}} M_2^{\frac{2}{9}}\right) \\ &\qquad + \mathrm{D}_2(T)\boldsymbol{\nabla}^2\left(M_0^{\frac{20}{9}} M_1^{-\frac{16}{9}} M_2^{\frac{5}{9}}\right) + [\mathrm{coag}]_{LN}^{(0)} - \boldsymbol{\nabla}\cdot\mathbf{c}_T M_0 \end{aligned} \tag{4.66}$$

First moment:

$$\begin{aligned} &\boldsymbol{u}\cdot\boldsymbol{\nabla}M_1 + M_1(\boldsymbol{\nabla}\cdot\boldsymbol{u}) - 2v_m I_0 - \theta(T)(S-1)\left(M_0^{\frac{2}{9}} M_1^{\frac{8}{9}} M_2^{-\frac{1}{9}}\right) \\ &\qquad = D_1(T)\boldsymbol{\nabla}^2\left(M_0^{\frac{2}{9}} M_1^{\frac{8}{9}} M_2^{-\frac{1}{9}}\right) \\ &\qquad + \mathrm{D}_2(T)\boldsymbol{\nabla}^2\left(M_0^{\frac{5}{9}} M_1^{\frac{5}{9}} M_2^{-\frac{1}{9}}\right) - \boldsymbol{\nabla}\cdot\mathbf{c}_T M_1 \end{aligned} \tag{4.67}$$

Second moment:

$$\begin{aligned} &\boldsymbol{u}\cdot\boldsymbol{\nabla}M_2 + M_2(\boldsymbol{\nabla}\cdot\boldsymbol{u}) - v_p^{*2} I_0 - \theta(T)(S-1)(M_0^{-\frac{1}{9}} M_1^{\frac{5}{9}} M_2^{\frac{5}{9}}) \\ &\qquad = D_1(T)\boldsymbol{\nabla}^2\left(M_0^{-\frac{1}{9}} M_1^{\frac{5}{9}} M_2^{\frac{5}{9}}\right) \\ &\qquad + D_2(T)\boldsymbol{\nabla}^2\left(M_0^{-\frac{1}{9}} M_1^{\frac{8}{9}} M_2^{\frac{2}{9}}\right) + [\mathrm{coag}]_{LN}^{(2)} - \boldsymbol{\nabla}\cdot\mathbf{c}_T M_2 \end{aligned} \tag{4.68}$$

where; $\mathrm{D}_1(T) = (\pi/162)^{\frac{1}{3}}(k_B T/\mu)$ and $\mathrm{D}_2(T) = 2.671(\pi/162)^{\frac{1}{3}}(k_B T/\mu)\ell_p$. Through further simplification of the advective term, the final equations that describe the transport of M_0, M_1 and M_2 can obtained as:

$$\begin{aligned}\boldsymbol{\nabla}\cdot(\boldsymbol{u}+\mathbf{c}_T)M_0 - I_0 &= D_1(T)\boldsymbol{\nabla}^2\left(M_0^{\frac{14}{9}}M_1^{-\frac{7}{9}}M_2^{\frac{2}{9}}\right)\\ &+D_2(T)\boldsymbol{\nabla}^2\left(M_0^{\frac{20}{9}}M_1^{-\frac{16}{9}}M_2^{\frac{5}{9}}\right)+[\mathrm{coag}]_{LN}^{(0)}\end{aligned} \tag{4.69}$$

$$\begin{aligned}\boldsymbol{\nabla}\cdot(\boldsymbol{u}+\mathbf{c}_T)M_1 - 2v_m I_0 - \theta(T)(S-1)M_0^{\frac{2}{9}}M_1^{\frac{8}{9}}M_2^{-\frac{1}{9}}&\\ = D_1(T)\boldsymbol{\nabla}^2\left(M_0^{\frac{2}{9}}M_1^{\frac{8}{9}}M_2^{-\frac{1}{9}}\right)&\\ +\mathrm{D}_2(T)\boldsymbol{\nabla}^2\left(M_0^{\frac{5}{9}}M_1^{\frac{5}{9}}M_2^{-\frac{1}{9}}\right)&\end{aligned} \tag{4.70}$$

$$\begin{aligned}\boldsymbol{\nabla}\cdot(\boldsymbol{u}+\mathbf{c}_T)M_2 - 4v_m{}^2 I_0 - 2\theta(T)(S-1)\left(M_0^{-\frac{1}{9}}M_1^{\frac{5}{9}}M_2^{\frac{5}{9}}\right)&\\ = D_1(T)\boldsymbol{\nabla}^2\left(M_0^{-\frac{1}{9}}M_1^{\frac{5}{9}}M_2^{\frac{5}{9}}\right)&\\ +D_2(T)\boldsymbol{\nabla}^2\left(M_0^{-\frac{1}{9}}M_1^{\frac{8}{9}}M_2^{\frac{2}{9}}\right)+[\mathrm{coag}]_{LN}^{(2)}&\end{aligned} \tag{4.71}$$

4.2.8 Implementation of Aerosol Model into COMSOL

The moments of the general dynamics equation are dependent on the temperature and velocity profiles of the system. Each of the moment equations given in Equations 4.69, 4.70 and 4.71 are implemented individually using the Stabilized Convection-Diffusion Equation (CDE) physics interface in COMSOL. The governing equation for this interface is

$$\boldsymbol{\nabla} \cdot (-D_{st}\boldsymbol{\nabla} M_i + \boldsymbol{\alpha} M_i) + \boldsymbol{\beta} \cdot \boldsymbol{\nabla} M_i + a M_i = f \tag{4.72}$$

where M_i is the moment with $i = 0,1,2$ being the moment respective orders and D_{st} is the diffusion coefficient for stabilization [m^2/s]. D_{st} is used only to achieve stabilization and it must not affect the calculations of the moments. Therefore, a value of 10^{-8} m^2/s was designated for all CDE equations. $\boldsymbol{\alpha}$, $\boldsymbol{\beta}$, a and f are the coefficients of the equation. Based on the moment equations and the aerosol mechanism involved in the system, the values of these coefficients change.

The high nonlinearity of moment equations creates difficulties in achieving convergence during the simulation. A multiple step solving mechanism in which the aerosol mechanisms are cumulatively added was utilized. The simulations were initiated with vapor transport phenomena and nucleation present in the system. The value of the coefficients used were based on the moment equations derived in the previous subchapter, and they are given in Table 4.1.

Table 4.1. Coefficients for Equation 4.72 where there is only nucleation.

Moment	$\boldsymbol{\alpha}$	f
M_0	$\boldsymbol{u}$	I_0
M_1	$\boldsymbol{u}$	$2v_m I_0$
M_2	$\boldsymbol{u}$	$4{v_m}^2 I_0$

The solution of this step was taken as the basis for the following step which involves surface growth by condensation. The coefficients involved in the evaluation of moments for this step are given in Table 4.2, which are components of the lognormal form of the GDE given in equations 4.69-4.71.

Table 4.2. Coefficients for Equation 4.72 for surface growth and condensation.

Moment	$\boldsymbol{\alpha}$	f
M_0	$\boldsymbol{u}$	I_0
M_1	$\boldsymbol{u}$	$2v_m I_0 + \theta(T)(S-1)M_0^{\frac{2}{9}} M_1^{\frac{8}{9}} M_2^{-\frac{1}{9}}$
M_2	$\boldsymbol{u}$	$4{v_m}^2 I_0 + 2\theta(T)(S-1)\left(M_0^{-\frac{1}{9}} M_1^{\frac{5}{9}} M_2^{\frac{5}{9}}\right)$

Due to the high temperatures present in the furnace, aerosol formation takes place only in the outlet tube. Therefore, the stabilized convection diffusion equation (Equation 4.72) is only solved in the outlet tube, downstream of the furnace. Particle formation and growth only takes place if the saturation ratio is larger than 1, therefore, along with these coefficients an "if" condition is also applied to prevent negative growth terms. The condition states that if the value of saturation ratio is less than equal to 1 all the f terms in M_1 and M_2 will be taken as 0 and for values larger than 1, the coefficients given in Table 4.1 and Table 4.2 will be taken for nucleation only and surface growth by condensation respectively.

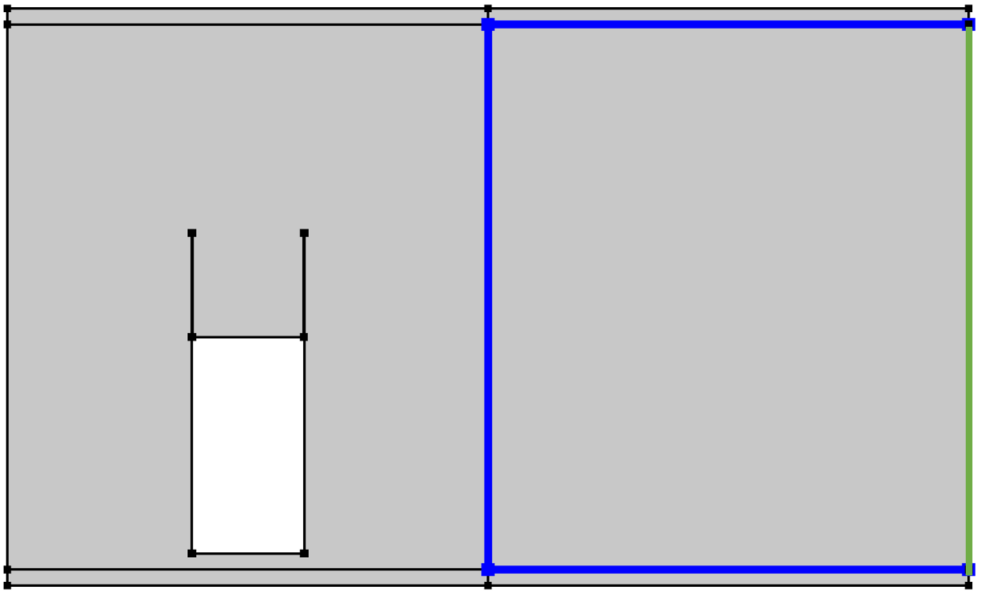

Figure 4.1. **Boundaries for stabilized diffusion coefficient equation.** Blue lines indicate the internal boundaries including the end of the furnace and the outlet boundary, green line on the right is the outlet boundary.

The boundaries for moment equations can be seen in Figure 4.1. The boundary condition for the inner boundaries is the Dirichlet boundary condition. The values for each moment vary; for M_0 the value is taken as 10^8, for M_1 it is 10^{-12} and for M_3 it is 10^{-40}. These values are taken to prevent overshooting and consequent negative values, which are common in the Galerkin-based finite element method. Due to fractional orders of moments for condensational growth, achieving convergence with the lognormal model is extremely sensitive to the presence of negative values that can be produced because of the in-cell interpolations and resulting overshoots. For the outlet boundary, no diffusive flux condition was assigned (Equation 4.73). This is because the particle diffusion coefficient is very low, and the transport happens mainly due to convection (refer Figure 3.12b)

$$-\mathbf{n} \cdot (-c_s \nabla M_i) = 0 \tag{4.73}$$

Saturation ratio and nucleation rate are two important parameters to consider for aerosol formation as they determine the amount of aerosol that will be formed in the outlet tube. When the value of saturation ratio exceeds 1, nucleation is favored, but rate-wise nucleation becomes only significant when S is much larger, as described by the classical nucleation theory (Equation 4.25). Therefore, it is important to know the variation of the saturation ratio throughout the system. In Figure 4.2a the logarithmic plot of saturation ratio throughout the tube is illustrated. The temperature profile of the system was given in Figure 3.8 and based on that, towards the outlet of the tube, the vapor pressure of antimony decreases and with higher concentrations of antimony present in the system, the saturation ratio reaches its peak in the system domain.

Nucleation rate is the rate at which the vapor is converted into particles of critical nucleus size. Contour map of the nucleation rate is given in Figure 4.2b. Note that the saturation ratio also directly effects the surface growth term (see Equation 4.21), which effects the condensation rate. Nucleation takes place right at the exit of the furnace, leading to vapor conversion into particles and depletion of the monomer quickly after the gas leaves the furnace.

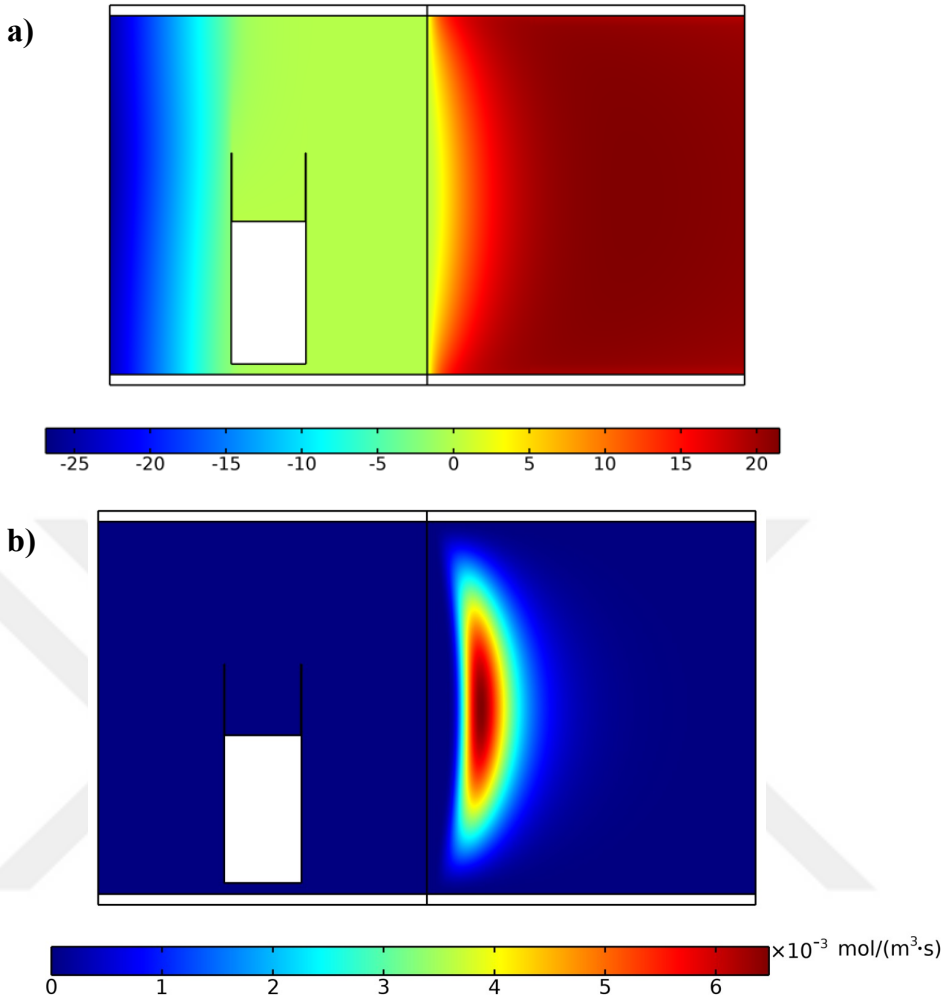

Figure 4.2. **Saturation ratio and nucleation rate distribution maps for 500 sccm flow rate.** a) Saturation ratio in base 10 logarithmic scale b) Nucleation rate of antimony vapor.

M_0 and M_1 were defined as the total number concentration of the particles and particle volume concentration respectively. These moments are used to determine the efficiency of the generator. Average volume of the particles, particle mass flow rate and yield are determined by using these moments. The flow map of M_0 and M_1 are given in Figure 4.3.

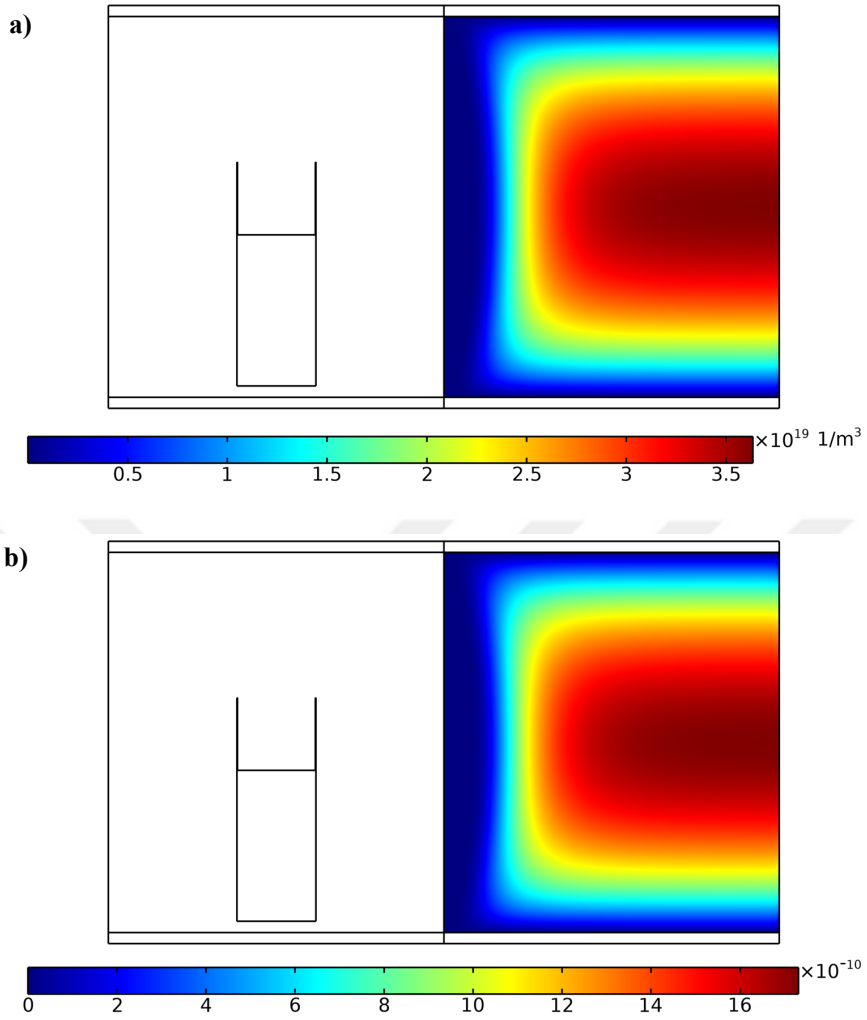

Figure 4.3. **Flow maps of M_0 and M_1 for 500 sccm flow rate.** a) M_0 b) M_1

The distributions in Figure 4.3 show that the particle formation occurs somewhere close to the middle of the outlet tube, and then the particles are dragged by advection (Figure 4.1a). For the surface growth and condensation mechanisms at the outlet; the average volume of the particles was determined to be 4.98×10^{-29} m^3, close to the value for the critical nucleus size (the dimer), which is expected because there is no coagulation in the system and condensation appears to be slow. Particle mass flow rate was calculated as 0.239 mg/min and yield was determined to be %13.6, which are very close to the values experimentally observed in the benchmark (~1 mg/min and ~%10, respectively).

CHAPTER 5

CONCLUSIONS AND FUTURE WORK

ECGs provide a simple yet useful approach for delivering aerosols of elements with high volatility. However, the main problem with ECGs is that they have low yield. This problem have been tried to overcome with flow field manipulation and vapor management by employing various flow configurations[52, 53]. The yields and mass flow rates obtained by the experimental designs do not pose a long-lasting solution as they are specific to a set of operational parameters and materials. In this study, a rigorous model for the aerosol formation in evaporation condensation generators was developed. Mathematical modeling of momentum, heat and mass transport phenomena was accomplished, and a very comprehensive form a lognormal model for aerosol dynamics was developed. Model equations were solved in COMSOL Multiphysics ® version 5.6, in which a custom solver was configured for a reduced version of the aerosol dynamics model that involves nucleation and condensation. The numerical results from these simulations are reasonable, however for further achieving further accuracy, reliable vapor pressure and physical data, incorporating a more realistic temperature profile in the furnace, and the implementation of the remaining mechanisms is required. Especially with the implementation of all mechanisms of aerosol dynamics, important growth and transport mechanisms can be elucidated.

The future work should focus on studying the interplay of all terms of the general aerosol dynamics developed in this study, as well as extending the 2D model to 3D, so that the curvilinear features of the studied geometry can be captured and inaccuracies resulting from the geometric simplifications can be reduced.

Constructing an experimental setup for testing the model framework for aerosol generation from different elements, such as Bi, S and Zn, is important. After

verifying the model, a higher yield ECG can be constructed ala previous designs [52, 53], and a temperature programming scenario can be developed for extracting constant aerosol output from the ECG.

REFERENCES

[1] R. Rossetti, S. Nakahara, and L. E. Brus, "Quantum size effects in the redox potentials, resonance Raman spectra, and electronic spectra of CdS crystallites in aqueous solution," *J. Chem. Phys.*, vol. 79, no. 2, pp. 1086–1088, Jul. 1983, doi: 10.1063/1.445834.

[2] E. Tiguntseva *et al.*, "Room-Temperature Lasing from Mie-Resonant Nonplasmonic Nanoparticles," *ACS Nano*, vol. 14, no. 7, pp. 8149–8156, Jul. 2020, doi: 10.1021/acsnano.0c01468.

[3] K. Orthaber, M. Pristovnik, K. Skok, B. Perić, and U. Maver, "Skin Cancer and Its Treatment: Novel Treatment Approaches with Emphasis on Nanotechnology," *J. Nanomater.*, vol. 2017, pp. 1–20, 2017, doi: 10.1155/2017/2606271.

[4] F. Todescato, I. Fortunati, A. Minotto, R. Signorini, J. Jasieniak, and R. Bozio, "Engineering of Semiconductor Nanocrystals for Light Emitting Applications," *Materials*, vol. 9, no. 8, p. 672, Aug. 2016, doi: 10.3390/ma9080672.

[5] A. Hagfeldt and M. Grätzel, "Molecular Photovoltaics," *Acc. Chem. Res.*, vol. 33, no. 5, pp. 269–277, May 2000, doi: 10.1021/ar980112j.

[6] "Quantum dot dot dot," *Nat. Nanotechnol.*, vol. 18, no. 12, pp. 1375–1375, Dec. 2023, doi: 10.1038/s41565-023-01586-x.

[7] "Analyze Results." Accessed: Mar. 03, 2024. [Online]. Available: https://www.webofscience.com/wos/woscc/analyze-results/01870f2f-23ca-4a1c-8e25-664590d6807e-c282fe8b

[8] A. M. Smith and S. Nie, "Semiconductor Nanocrystals: Structure, Properties, and Band Gap Engineering," *Acc. Chem. Res.*, vol. 43, no. 2, pp. 190–200, Feb. 2010, doi: 10.1021/ar9001069.

[9] G. Ramalingam *et al.*, "Quantum Confinement Effect of 2D Nanomaterials," in *Quantum Dots - Fundamental and Applications*, F. Divsar, Ed., IntechOpen, 2020. doi: 10.5772/intechopen.90140.

[10] H. Chen, Y. Gong, and R. Han, "Cadmium Telluride Quantum Dots (CdTe-QDs) and Enhanced Ultraviolet-B (UV-B) Radiation Trigger Antioxidant Enzyme Metabolism and Programmed Cell Death in Wheat Seedlings," *PLoS ONE*, vol. 9, no. 10, p. e110400, Oct. 2014, doi: 10.1371/journal.pone.0110400.

[11] A. Fu, W. Gu, C. Larabell, and A. P. Alivisatos, "Semiconductor nanocrystals for biological imaging," *Curr. Opin. Neurobiol.*, vol. 15, no. 5, pp. 568–575, Oct. 2005, doi: 10.1016/j.conb.2005.08.004.

[12] Y. Kim, D. H. Wi, J. W. Hong, and S. W. Han, "Plasmonic Nanocrystal Assembly–Semiconductor Hybrids for Boosting Visible to Near-Infrared Photocatalysis," *ACS Nano*, vol. 17, no. 18, pp. 18641–18651, Sep. 2023, doi: 10.1021/acsnano.3c08182.

[13] J. Schlenkrich *et al.*, "Investigation of the Photocatalytic Hydrogen Production of Semiconductor Nanocrystal-Based Hydrogels," *Small*, vol. 19, no. 21, p. 2208108, May 2023, doi: 10.1002/smll.202208108.

[14] R. Burke, K. L. Bren, and T. D. Krauss, “Semiconductor nanocrystal photocatalysis for the production of solar fuels,” *J. Chem. Phys.*, vol. 154, no. 3, p. 030901, Jan. 2021, doi: 10.1063/5.0032172.
[15] “Quantum Dots.” Accessed: Apr. 16, 2024. [Online]. Available: https://www.sigmaaldrich.com/TR/en/technical-documents/technical-article/materials-science-and-engineering/biosensors-and-imaging/quantum-dots
[16] C. B. Murray, C. R. Kagan, and M. G. Bawendi, “Self-Organization of CdSe Nanocrystallites into Three-Dimensional Quantum Dot Superlattices,” *Science*, vol. 270, no. 5240, pp. 1335–1338, Nov. 1995, doi: 10.1126/science.270.5240.1335.
[17] M. D. Tessier, D. Dupont, K. De Nolf, J. De Roo, and Z. Hens, “Economic and Size-Tunable Synthesis of InP/ZnE (E = S, Se) Colloidal Quantum Dots.,” *Chem. Mater.*, vol. 27, no. 13, pp. 4893–4898, Jul. 2015, doi: 10.1021/acs.chemmater.5b02138.
[18] A. L. Rogach, Ed., *Semiconductor nanocrystal quantum dots: synthesis, assembly, spectroscopy, and applications*. Wien ; New York: Springer, 2008.
[19] K. Agarwal, H. Rai, and S. Mondal, “Quantum dots: an overview of synthesis, properties, and applications,” *Mater. Res. Express*, vol. 10, no. 6, p. 062001, Jun. 2023, doi: 10.1088/2053-1591/acda17.
[20] A. Karatutlu, A. Barhoum, and A. Sapelkin, “Liquid-phase synthesis of nanoparticles and nanostructured materials,” in *Emerging Applications of Nanoparticles and Architecture Nanostructures*, Elsevier, 2018, pp. 1–28. doi: 10.1016/B978-0-323-51254-1.00001-4.
[21] T. Athar, “Smart precursors for smart nanoparticles,” in *Emerging Nanotechnologies for Manufacturing*, Elsevier, 2015, pp. 444–538. doi: 10.1016/B978-0-323-28990-0.00017-8.
[22] T. A. Saleh, “Large-scale production of nanomaterials and adsorbents,” in *Interface Science and Technology*, vol. 34, Elsevier, 2022, pp. 167–197. doi: 10.1016/B978-0-12-849876-7.00007-5.
[23] A. Matthews and K. Holmberg, “PVD and CVD Coatings,” in *Encyclopedia of Tribology*, Q. J. Wang and Y.-W. Chung, Eds., Boston, MA: Springer US, 2013, pp. 2705–2711. doi: 10.1007/978-0-387-92897-5_724.
[24] L. Xie, D. Abliz, and D. Li, “Thin Film Coating for Polymeric Micro Parts,” in *Comprehensive Materials Processing*, Elsevier, 2014, pp. 157–170. doi: 10.1016/B978-0-08-096532-1.00713-5.
[25] C. A. Charitidis, P. Georgiou, M. A. Koklioti, A.-F. Trompeta, and V. Markakis, “Manufacturing nanomaterials: from research to industry,” *Manuf. Rev.*, vol. 1, p. 11, 2014, doi: 10.1051/mfreview/2014009.
[26] R. J. Martín-Palma and A. Lakhtakia, “Vapor-Deposition Techniques,” in *Engineered Biomimicry*, Elsevier, 2013, pp. 383–398. doi: 10.1016/B978-0-12-415995-2.00015-5.
[27] C. M. Sorensen, Q. Li, H. K. Xu, Z. X. Tang, K. J. Klabunde, and G. C. Hadjipanayis, “Aerosol Spray Pyrolysis Synthesis Techniques,” in *Nanophase*

Materials, G. C. Hadjipanayis and R. W. Siegel, Eds., Dordrecht: Springer Netherlands, 1994, pp. 109–116. doi: 10.1007/978-94-011-1076-1_15.
[28] L. Mangolini, E. Thimsen, and U. Kortshagen, "High-Yield Plasma Synthesis of Luminescent Silicon Nanocrystals," *Nano Lett.*, vol. 5, no. 4, pp. 655–659, Apr. 2005, doi: 10.1021/nl050066y.
[29] R. Strobel and S. E. Pratsinis, "Flame aerosol synthesis of smart nanostructured materials," *J. Mater. Chem.*, vol. 17, no. 45, p. 4743, 2007, doi: 10.1039/b711652g.
[30] U. R. Kortshagen, R. M. Sankaran, R. N. Pereira, S. L. Girshick, J. J. Wu, and E. S. Aydil, "Nonthermal Plasma Synthesis of Nanocrystals: Fundamental Principles, Materials, and Applications," *Chem. Rev.*, vol. 116, no. 18, pp. 11061–11127, Sep. 2016, doi: 10.1021/acs.chemrev.6b00039.
[31] "Catalog of gas-liquid-solid precursors of the elements." Accessed: Apr. 16, 2024. [Online]. Available: https://www.strem.com/catalog/
[32] S. Bandyopadhyay and J. Anderson, "Capacitive infrared photodetector for room temperature operation," *Appl. Phys. Lett.*, vol. 102, no. 10, p. 103108, Mar. 2013, doi: 10.1063/1.4795520.
[33] F. C. Krebs, "Solar Cell Materials—Developing Technologies . Edited by Gavin J. Conibeer and Arthur Willoughby," *Energy Technol.*, vol. 2, no. 9–10, pp. 851–851, Oct. 2014, doi: 10.1002/ente.201405007.
[34] B. Ganjipour *et al.*, "GaSb nanowire single-hole transistor," *Appl. Phys. Lett.*, vol. 99, no. 26, p. 262104, Dec. 2011, doi: 10.1063/1.3673328.
[35] M. A. Todd, G. Bhandari, and T. H. Baum, "Novel Antimony Precursors for Low-Temperature CVD of Antimonide Thin Films," *MRS Proc.*, vol. 495, p. 113, 1997, doi: 10.1557/PROC-495-113.
[36] PubChem, "Stibine." Accessed: Mar. 03, 2024. [Online]. Available: https://pubchem.ncbi.nlm.nih.gov/compound/9359
[37] N. B. Uner and E. Thimsen, "Phase mixing in GaSb nanocrystals synthesized by nonequilibrium plasma aerotaxy," *Plasma Process. Polym.*, vol. 17, no. 5, p. 1900233, May 2020, doi: 10.1002/ppap.201900233.
[38] N. B. Uner and E. Thimsen, "Nonequilibrium plasma aerotaxy of size controlled GaN nanocrystals," *J. Phys. Appl. Phys.*, vol. 53, no. 9, p. 095201, Feb. 2020, doi: 10.1088/1361-6463/ab59e6.
[39] N. B. Uner, D. M. Niedzwiedzki, and E. Thimsen, "Nonequilibrium Plasma Aerotaxy of InN Nanocrystals and Their Photonic Properties," *J. Phys. Chem. C*, vol. 123, no. 50, pp. 30613–30622, Dec. 2019, doi: 10.1021/acs.jpcc.9b09555.
[40] M. J. Sheehan, T. M. Peters, L. Cena, P. T. O'Shaughnessy, and R. A. Gussman, "Generation of Nanoparticles with a Nebulizer-Cyclone System," *Aerosol Sci. Technol.*, vol. 43, no. 11, pp. 1091–1098, Nov. 2009, doi: 10.1080/02786820903173687.
[41] C. F. Lange and W. H. Finlay, "Liquid Atomizing: Nebulizing and Other Methods of Producing Aerosols," *J. Aerosol Med.*, vol. 19, no. 1, pp. 28–35, Mar. 2006, doi: 10.1089/jam.2006.19.28.

[42] O. Misik, A. Peštálová, M. Belka, and F. Lízal, “Nebulizer particle size distribution measured by various methods,” *EPJ Web Conf.*, vol. 264, p. 01023, 2022, doi: 10.1051/epjconf/202226401023.
[43] H. R. Ghaffarian, M. Saiedi, M. A. Sayyadnejad, and A. M. Rashidi, “Synthesis of ZnO Nanoparticles by Spray Pyrolysis Method,” *Iran. J. Chem. Chem. Eng. IJCCE*, vol. 30, no. 1, Mar. 2011, doi: 10.30492/ijcce.2011.6250.
[44] S. H. Narwade, V. V. Jadhav, and R. S. Mane, “Spray-pyrolysis technique for the synthesis of metal oxide nanostructures,” in *Solution Methods for Metal Oxide Nanostructures*, Elsevier, 2023, pp. 155–174. doi: 10.1016/B978-0-12-824353-4.00013-0.
[45] M. Alonso, F. J. Alguacil, M. I. Martin, Y. Kousaka, and T. Nomura, “Aerosol particle size growth by simultaneous coagulation and condensation with diffusion losses in laminar flow tubes,” *J. Aerosol Sci.*, vol. 30, no. 9, pp. 1191–1199, Oct. 1999, doi: 10.1016/S0021-8502(99)00020-8.
[46] “Generation of Nano/Submicron Particles Using an Electrically Heated Tube Furnace,” *Trans. Korean Soc. Mech. Eng. B*, vol. 27, no. 12, pp. 1734–1743, Dec. 2003, doi: 10.3795/KSME-B.2003.27.12.1734.
[47] S. K. Friedlander, *Smoke, dust, and haze: fundamentals of aerosol dynamics*, 2. ed. in Topics in chemical engineering. New York Oxford: Oxford Univ. Press, 2000.
[48] D. Turnbull and J. C. Fisher, “Rate of Nucleation in Condensed Systems,” *J. Chem. Phys.*, vol. 17, no. 1, pp. 71–73, Jan. 1949, doi: 10.1063/1.1747055.
[49] H. Y. Sohn, “Process Modeling in Non-Ferrous Metallurgy,” in *Treatise on Process Metallurgy*, Elsevier, 2014, pp. 701–838. doi: 10.1016/B978-0-08-096988-6.00024-9.
[50] T. M. Damour, S. H. Ehrman, M. N. A. Karlsson, L. S. Karlsson, and K. Deppert, “Experimental Evidence for Nonuniform Flow in a Horizontal Evaporation/Condensation Aerosol Generator,” *Aerosol Sci. Technol.*, vol. 39, no. 5, pp. 444–451, May 2005, doi: 10.1080/027868290959834.
[51] I. Gonda, A. F. A. El Khalik, and A. Z. Britten, “Hexamethylmelamine aerosols prepared in an evaporation-condensation generator,” *Int. J. Pharm.*, vol. 27, no. 2–3, pp. 255–265, Dec. 1985, doi: 10.1016/0378-5173(85)90074-2.
[52] Y. Singh, J. R.N. Javier, S. H. Ehrman, M. H. Magnusson, and K. Deppert, “Approaches to increasing yield in evaporation/condensation nanoparticle generation,” *J. Aerosol Sci.*, vol. 33, no. 9, pp. 1309–1325, Sep. 2002, doi: 10.1016/S0021-8502(02)00072-1.
[53] K. Wegner, B. Walker, S. Tsantilis, and S. E. Pratsinis, “Design of metal nanoparticle synthesis by vapor flow condensation,” *Chem. Eng. Sci.*, vol. 57, no. 10, pp. 1753–1762, May 2002, doi: 10.1016/S0009-2509(02)00064-7.
[54] D. H. AG, “GRIMM 7860.” Accessed: Apr. 16, 2024. [Online]. Available: https://www.durag.com/en/product-filter-837.htm?productID=GRIMM 7860
[55] “Condensation Monodisperse Aerosol Generator 3475,” TSI.com. Accessed: Apr. 16, 2024. [Online]. Available: https://tsi.com/Products/Aerosol-Generators-Dispersers/Monodisperse-Generators/Condensation-Monodisperse-Aerosol-Generator-3475

[56] A. Kalani and P. D. Christofides, “Modeling and Control of a Titania Aerosol Reactor,” *Aerosol Sci. Technol.*, vol. 32, no. 4, pp. 369–391, Apr. 2000, doi: 10.1080/027868200303687.
[57] S. E. Pratsinis and K.-S. Kim, “Particle coagulation, diffusion and thermophoresis in laminar tube flows,” *J. Aerosol Sci.*, vol. 20, no. 1, pp. 101–111, Jan. 1989, doi: 10.1016/0021-8502(89)90034-7.
[58] S. Panda and S. E. Pratsinis, “Modeling the synthesis of aluminum particles by evaporation-condensation in an aerosol flow reactor,” *Nanostructured Mater.*, vol. 5, no. 7–8, pp. 755–767, Sep. 1995, doi: 10.1016/0965-9773(95)00292-M.
[59] D. A. Terry, R. McGraw, and R. H. Rangel, “Method of Moments Solutions for a Laminar Flow Aerosol Reactor Model,” *Aerosol Sci. Technol.*, vol. 34, no. 4, pp. 353–362, Jan. 2001, doi: 10.1080/02786820118736.
[60] N. B. Uner and E. Thimsen, “In-Flight Size Focusing of Aerosols by a Low Temperature Plasma,” *J. Phys. Chem. C*, vol. 121, no. 23, pp. 12936–12944, Jun. 2017, doi: 10.1021/acs.jpcc.7b03572.
[61] D. Moher, G. Ren, D. M. Niedzwiedzki, R. Mishra, and E. Thimsen, “Photonic Properties of Thin Films Composed of Gallium Nitride Quantum Dots Synthesized by Nonequilibrium Plasma Aerotaxy,” *ACS Appl. Mater. Interfaces*, vol. 16, no. 14, pp. 17927–17936, Apr. 2024, doi: 10.1021/acsami.4c01909.
[62] N. Üner, “Growth of Small Particles in Nonequilibrium Plasmas,” [object Object]. doi: 10.7936/JNMY-Z638.
[63] F. M. White, *Viscous Fluid Flow*, 2nd ed. New York: McGraw-Hill, 1991.
[64] İ. Tosun, *Thermodynamics: Principles and Applications*. New Jersey London Singapore Beijing Shanghai Hong Kong Taipei Chennai: World Scientific, 2015.
[65] R. B. Bird, W. E. Stewart, and E. N. Lightfoot, *Transport Phenomena*, 2nd, Wiley international ed ed. New York: J. Wiley, 2002.
[66] F. Aqra and A. Ayyad, “Theoretical Estimation of Temperature-Dependent Surface Tension of Liquid Antimony, Boron, and Sulfur,” *Metall. Mater. Trans. B*, vol. 42, no. 3, pp. 437–440, Jun. 2011, doi: 10.1007/s11663-011-9506-5.
[67] A. F. Crawley and D. R. Kiff, “The density and viscosity of liquid antimony,” *Metall. Trans.*, vol. 3, no. 1, pp. 157–159, Jan. 1972, doi: 10.1007/BF02680594.
[68] “Atomic Weight of Antimony | Commission on Isotopic Abundances and Atomic Weights.” Accessed: Mar. 05, 2024. [Online]. Available: https://www.ciaaw.org/antimony.htm
[69] E. Clementi, D. L. Raimondi, and W. P. Reinhardt, “Atomic Screening Constants from SCF Functions. II. Atoms with 37 to 86 Electrons,” *J. Chem. Phys.*, vol. 47, no. 4, pp. 1300–1307, Aug. 1967, doi: 10.1063/1.1712084.
[70] R. K. Rajgarhia, D. E. Spearot, and A. Saxena, “Heterogeneous dislocation nucleation in single crystal copper–antimony solid-solution alloys,” *Model. Simul. Mater. Sci. Eng.*, vol. 17, no. 5, p. 055001, Jul. 2009, doi: 10.1088/0965-0393/17/5/055001.

[71] A. T. Aldred and J. N. Pratt, “Vapor Pressures or Zinc, Cadmium, Antimony, and Thallium.,” *J. Chem. Eng. Data*, vol. 8, no. 3, pp. 429–431, Jul. 1963, doi: 10.1021/je60018a043.
[72] G. M. Rosenblatt and C. E. Birchenall, “Vapor Pressure of Antimony by the Torsion-Effusion Method,” *J. Chem. Phys.*, vol. 35, no. 3, pp. 788–794, Sep. 1961, doi: 10.1063/1.1701217.
[73] C. L. Yaws, *The Yaws handbook of vapor pressure: Antoine coefficients*, Second edition. Amsterdam ; Boston: Elsevier/GPP, Gulf Professional Publishing is an imprint of Elsevier, 2015.
[74] F. P. Incropera, D. P. DeWitt, T. L. Bergman, and A. S. Lavine, Eds., *Principles of heat and mass transfer*, 7. ed., International student version. Hoboken, NJ: Wiley, 2013.
[75] R. C. Ng, A. El Sachat, J. Jaramillo-Fernandez, C. M. Sotomayor-Torres, and E. Chavez-Angel, “Far-Field Radiative Thermal Rectification Based on Asymmetric Emissivity,” *ACS Appl. Opt. Mater.*, p. acsaom.3c00235, Sep. 2023, doi: 10.1021/acsaom.3c00235.
[76] N. B. Üner, “Unpublished data,” 2016.
[77] E. A. Guggenheim, *Elements of the Kinetic Theory of Gases (The International Encyclopedia of Physical Chemistry and Chemical Physics)*, 1st ed., vol. 1. Great Britain: Pergamon Press, 1960.
[78] T. L. C. Gomes, F. S. Lobato, L. C. Borges, F. O. Arouca, and J. J. R. Damasceno, “Mathematical modeling of monodisperse nanoparticle production in aerosols using separation in an electric field,” *Soft Comput.*, vol. 25, no. 16, pp. 11347–11362, Aug. 2021, doi: 10.1007/s00500-021-05931-x.
[79] G. Yang *et al.*, “Towards an Improved Understanding of the Evolution of the Size Distribution of Ultrafine Nanoparticles Produced by a Rapidly Quenched Vapor Source,” *Metall. Mater. Trans. A*, vol. 55, no. 5, pp. 1509–1515, May 2024, doi: 10.1007/s11661-024-07340-9.
[80] C. Deng *et al.*, “Measurement report: Size distributions of urban aerosols down to 1 nm from long-term measurements,” *Atmospheric Chem. Phys.*, vol. 22, no. 20, pp. 13569–13580, Oct. 2022, doi: 10.5194/acp-22-13569-2022.
[81] S. Bau and J. Nuvoli, “Combining the Particle Size Selector and a condensation particle counter to determine the number size distribution of airborne nanoparticles,” *J. Aerosol Sci.*, vol. 128, pp. 22–33, Feb. 2019, doi: 10.1016/j.jaerosci.2018.11.007.
[82] Q.-R. Yu, F. Zhang, J. Li, and J. Zhang, “Analysis of sea-salt aerosol size distributions in radiative transfer,” *J. Aerosol Sci.*, vol. 129, pp. 71–86, Mar. 2019, doi: 10.1016/j.jaerosci.2018.11.014.
[83] K. W. Lee, J. Chen, and J. A. Gieseke, “Log-Normally Preserving Size Distribution for Brownian Coagulation in the Free-Molecule Regime,” *Aerosol Sci. Technol.*, vol. 3, no. 1, pp. 53–62, Jan. 1984, doi: 10.1080/02786828408958993.
[84] E. Otto and H. Fissan, “Brownian coagulation of submicron particles,” *Adv. Powder Technol.*, vol. 10, no. 1, pp. 1–20, 1999, doi: 10.1016/S0921-8831(08)60453-7.

[85] D. Zhang, “Ash fouling, deposition and slagging in ultra-supercritical coal power plants,” in *Ultra-Supercritical Coal Power Plants*, Elsevier, 2013, pp. 133–183. doi: 10.1533/9780857097514.2.133.
[86] M. H. Mousazadeh and M. G. Marageh, “A perturbed Lennard-Jones chain equation of state for liquid metals,” *J. Phys. Condens. Matter*, vol. 18, no. 20, pp. 4793–4800, May 2006, doi: 10.1088/0953-8984/18/20/003.
[87] D. E. Seborg, *Process dynamics and control*, Fourth edition. Hoboken, NJ: Wiley, 2017.
[88] L. J. Reed and J. Berkson, “The Application of the Logistic Function to Experimental Data.,” *J. Phys. Chem.*, vol. 33, no. 5, pp. 760–779, May 1929, doi: 10.1021/j150299a014.
[89] K. W. Lee and B. Y. H. Liu, “On the Minimum Efficiency and the Most Penetrating Particle Size for Fibrous Filters,” *J. Air Pollut. Control Assoc.*, vol. 30, no. 4, pp. 377–381, Apr. 1980, doi: 10.1080/00022470.1980.10464592.

APPENDICES

A. Combustion Boat Photos

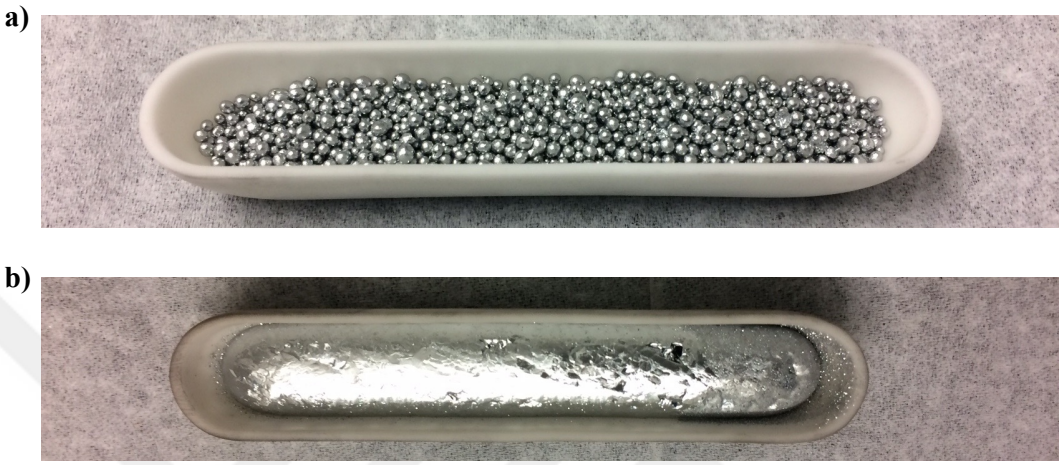

Figure A1. Combustion boat filled with Sb before and after the operation. a) Before the operation b) After the operation.

The Sb metal can be introduced to the boat as shots (Figure A1). Initially, the height of Sb within the boat is higher, however, due to viscous sintering in the furnace, these shots fuse together, resulting in lowered height of Sb in the boat. Therefore, it can be said that completely filling the boat with the Sb is not possible during operation.

B. Analysis of the Entrance Region

In a real ECG, the heated tube[10] is required to have some length upstream and downstream of the furnace, so that fittings at the ends of the tube can be retained at relatively low temperature. In the system modeled in the main text, the tube had an additional length of 300 mm downstream. A simulation was done in order to show the development of the flow and the temperature profiles in a similar region upstream, also of 300 mm length, through this inlet tube and at the entrance of the furnace. In the calculations, argon gas entered the upstream inlet of tube at room temperature with a volumetric flow of 500 sccm Around the entrance of the furnace there a focusing effect was observed in the streamlines (Figure B1). This is due to the sudden temperature change in the furnace, set at 823 K, and acceleration of the flow. However, the flow approaches fully developed conditions quickly downstream of the entrance, as seen in the form of a re-relaxation of streamlines, until the gas partially impinges on the boat where the sudden change in geometry causes another compression and subsequent expansion of the gas. Flow field just upstream of the boat was found to be very similar to that of flow obtained when the entrance portion of the tube was neglected, as shown in the main text (Figure 2.2), therefore studying the truncated geometry was acceptable in terms of fluid dynamics.

[10] Can be made of quartz, alumina, or even borosilicate glass if temperatures are below the softening point of 541 K.

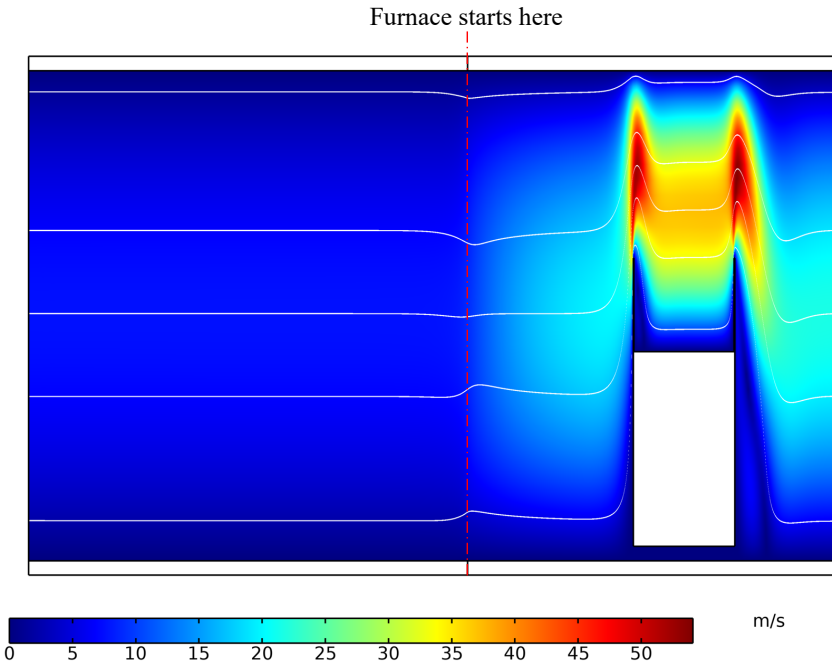

Figure B1. Flow map in the entrance region.

The temperature profile was then calculated to investigate whether argon gas reaches the boat at its desired temperature of 823 K. The boundary conditions for the inlet system are listed in Table B1.

Table B1. Boundary conditions for the inlet system.

Boundary	Boundary Condition
Internal walls of the inlet	$T\|_{tube} = T\|_{gas}$ $[-\boldsymbol{n} \cdot k(dT/dy)]\|_{tube} = [-\boldsymbol{n} \cdot k(dT/dy)]\|_{gas}$
External walls of the inlet	$\boldsymbol{q} = h(T_s - T_\infty) + \varepsilon\sigma\left({T_\infty}^4 - {T_s}^4\right)$
Furnace walls and boat	550 K
End of the glass tube – inlet	298 K

The temperature profile of the entrance region is shown in Figure B2. Over the boat, argon was seen to reach temperatures very close to the furnace temperature (823 K) when it reaches to the top of the boat. Therefore, neglecting the thermal entry region appears to be plausible in the calculations presented in the main text,

however, for shorter ECGs and larger flow rates, the entrance region and associated thermal equilibration within might be important

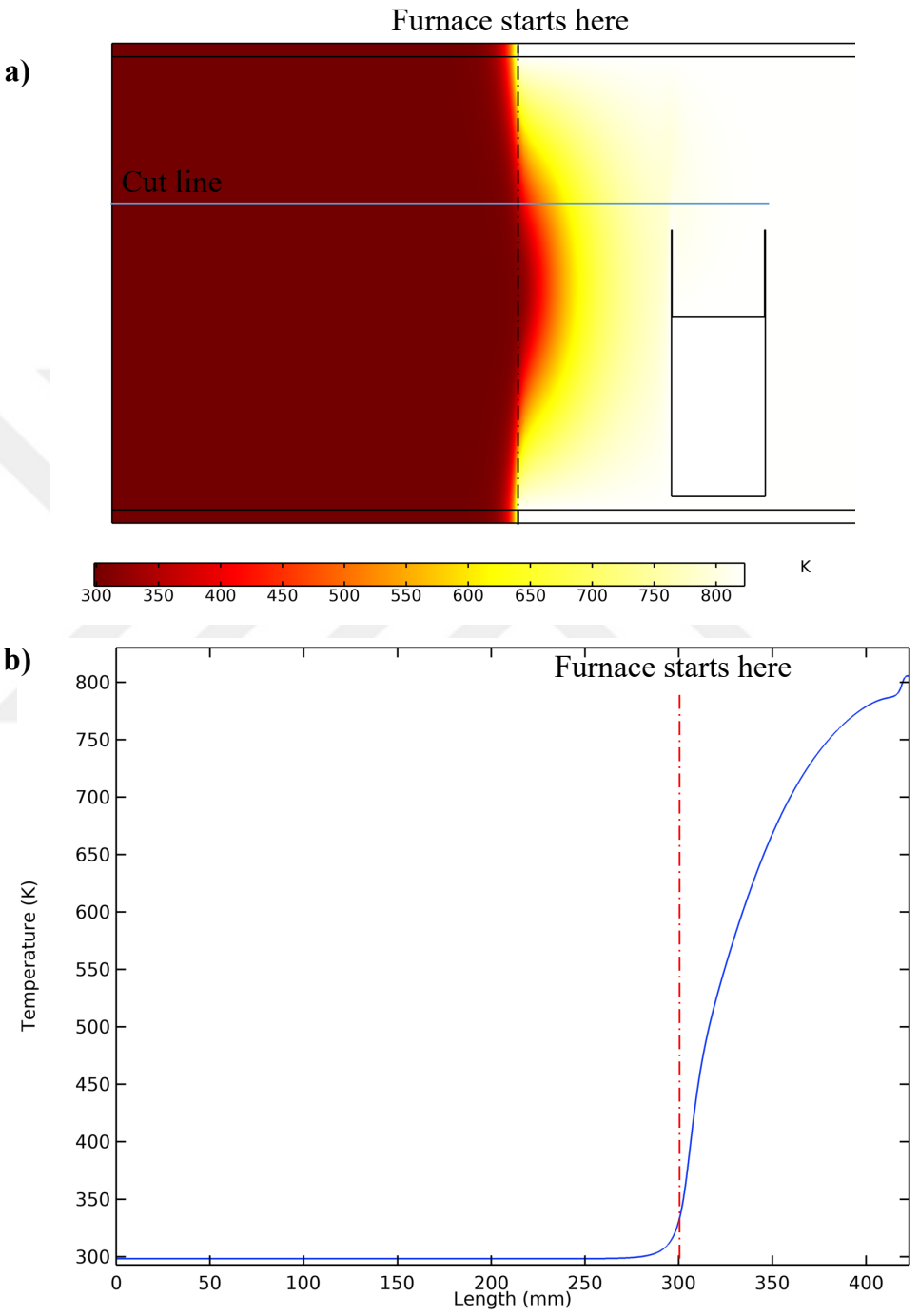

Figure B2. Temperature field in the entrance region. a) Temperature field in argon at the inlet and the entrance of the furnace. b) Axial temperature profile on the blue line shown in panel a.

C. On Predicting the Transport Properties of Antimony Vapor

Calculation of the diffusivity of Sb vapor through the Chapman-Enskog theory requires the use of Lennard-Jones parameters and the evaluation of the collision integral, $\Omega_{\mathcal{D},Sb-Ar}$. The collision diameter for the Sb-Ar pair was determined via utilizing the Van der Waals diameters with the combining rule; $\sigma_{Sb-Ar} = (\sigma_{Sb} + \sigma_{Ar})/2$. $\Omega_{\mathcal{D},Sb-Ar}$, was calculated with the following sets of equations [65]

$$\Omega_{\mathcal{D},Sb-Ar} = \frac{1.06036}{T^{*0.15610}} + \frac{0.19300}{\exp(0.47635T^*)} + \frac{1.03587}{\exp(1.52996T^*)} + \frac{1.76474}{\exp(3.89411T^*)} \quad \text{(C.1)}$$

$$T^* = \frac{k_B T}{\varepsilon_{Sb-Ar}} \quad \text{(C.2)}$$

$$\varepsilon_{Sb-Ar} = \sqrt{\varepsilon_{Sb}\varepsilon_{Ar}} \quad \text{(C.3)}$$

The Lennard-Jones parameter ε is found in the literature as ε/k_B. For Ar and Sb, these values are 122.4 K [36] and 3090 K [86], respectively.

D. Photos of a Quartz Tube Used in a Furnace-Type ECG

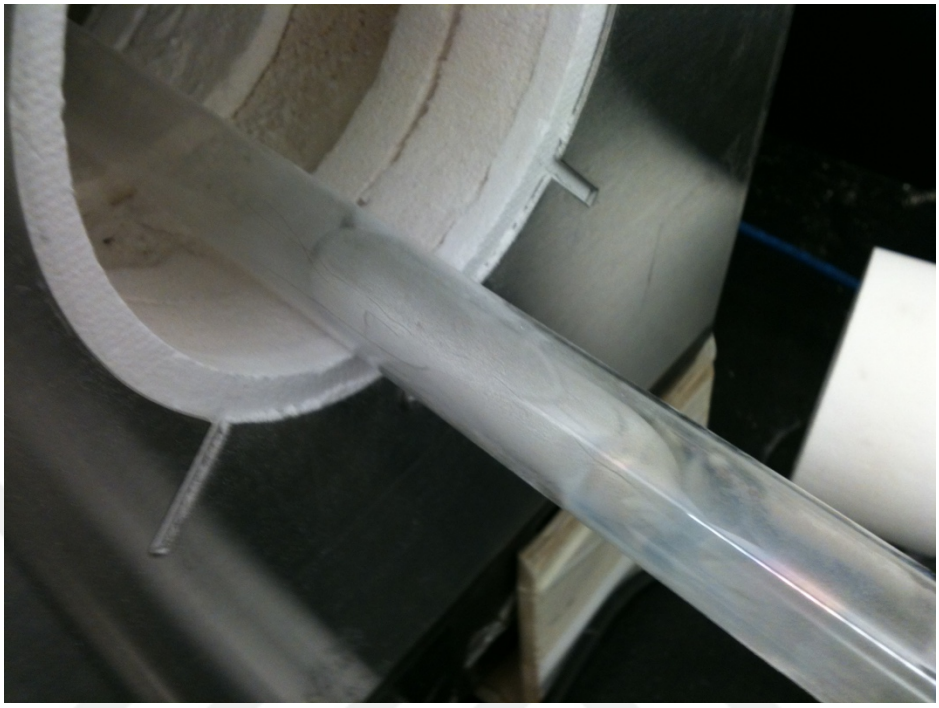

Figure D1. Part of the quartz tube located in the furnace of an ECG [62]. In this photo, the insulation block at the outlet of the furnace was removed (See Figure D2 below).

In section 2.3.4, diffusional flux to the interior walls of the tube was set to zero in the furnace, due to the saturation ratio being less than 1. This is justified by experimental observations done on a furnace-type ECG, as shown in Figure D1. After multiple operations that involved evaporation of Sb, the interior parts of the tube had little-to-no deposition.

For the parts of the tube that stays on the exit of the furnace, however, this is not true. The outlet tube is exposed to ambient temperature which cools the gas via both natural convection and radiation. Due to rapid cooling of the outlet tube (see Figure 3.7), thermophoresis and vapor diffusion cause Sb to move toward the walls of the outlet tube causing deposition which can be seen in Figure D2.

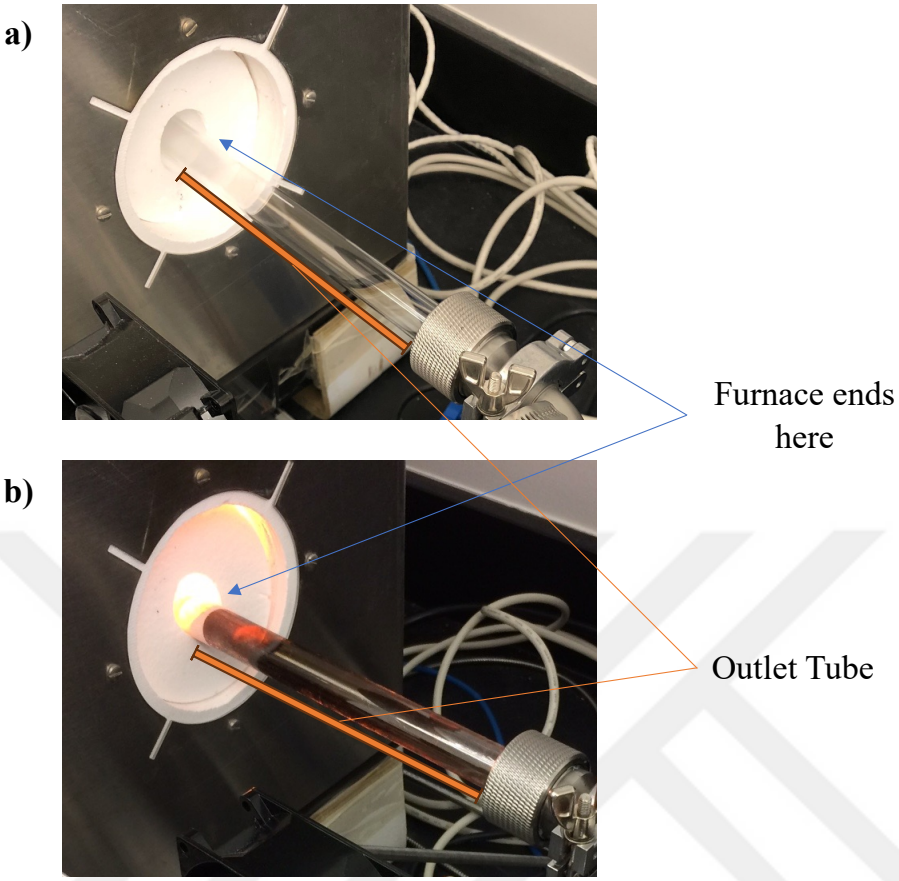

Figure D2. Outlet of the quartz tube located in an ECG [62]. a) Quartz tube before the operation b) Quartz tube after the operation.

E. Use of Step Functions in Modeling Conditional and Transitional Processes

Heaviside step functions were implemented in the calculations to describe conditional or transitional process, such as deposition of Sb vapor on the walls of the outlet tube and the transition from the diffusion coefficient of the vapor to that of the particle during artificial nucleation (Section 3.4). Unit step function is a piecewise function that yields 0 for negative arguments and 1 for positive arguments [87]:

$$\mathrm{S}(arg) = \begin{cases} 0 & arg < 0 \\ 1 & arg \geq 0 \end{cases} \qquad \text{(E.1)}$$

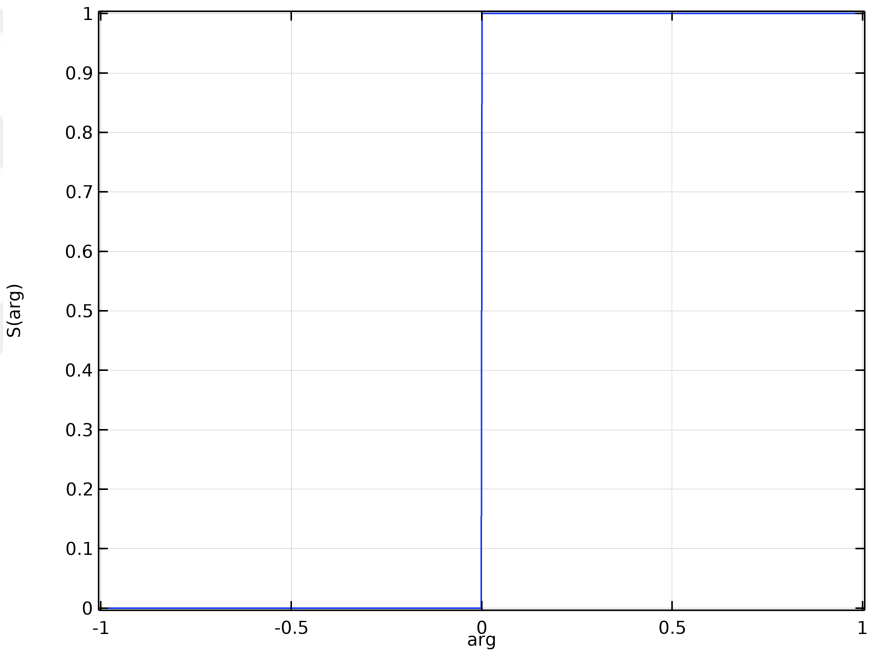

Figure E1. Unit step function. The argument for this function is designated as location.

In the finite element-based simulations conducted via COMSOL, continuous transitions are desired to prevent problems in achieving convergence. Because of this reason, smoothed Heaviside step functions (Φ_s) can be used as a replacement to the step function. A commonly used mathematical form of Φ_s is the unit logistic function[88].

$$\Phi_s(arg) = \frac{1}{1 + e^{-r \cdot arg}} \tag{E.2}$$

where r is the steepness of the curve and x is the argument of the function. Smoothed step function provides a continuous transition from 0 to 1 in the simulations which can be seen in Figure E2. r defines the size of the transition zone from 0 to 1. The smaller the value of r, the greater the size of the transition zone.

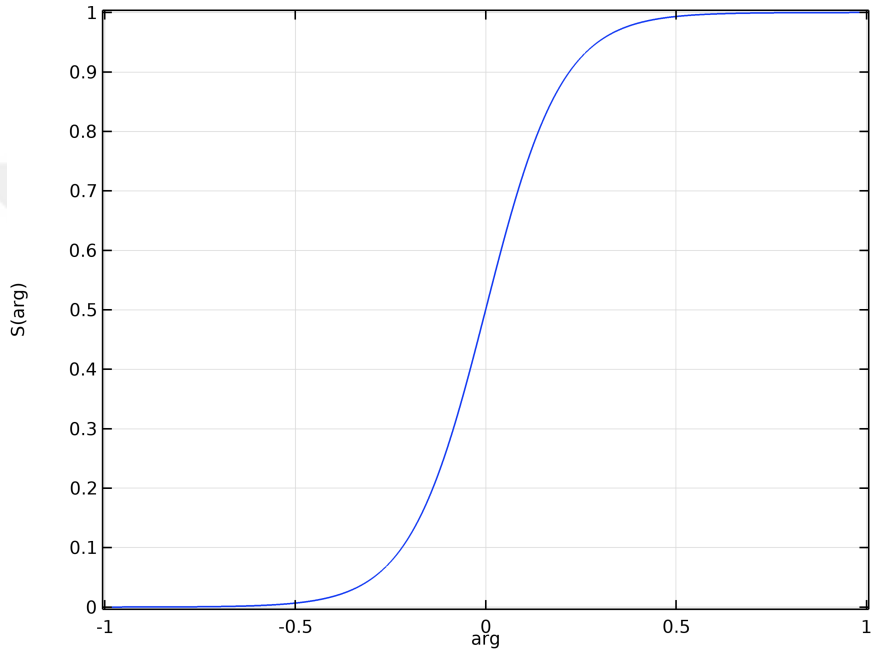

Figure E2. Unit Heaviside step functions. Smoothed version of the function shown in Figure E1. The value of r in Equation E.2 is set to 5. Note that COMSOL does not use a logistic function to describe the smoothed Heaviside function, but a similar functional form is present.

For vapor deposition on the walls, the argument for $\Phi_s$is the difference between the partial and the vapor pressures of Sb indicated by $P_{Sb} - P_{Sb}^{vap}$. Once the difference becomes positive, deposition occurs, therefore a relatively fast, but at the same, a smooth change is required so that flux to the walls is set to a nonzero value. Hence, size of the transition zone is taken to be 0.001 Pa. This means that when the value of the argument becomes -0.0005 the transition starts from 0 until the difference is 0.0005 where the value of the step function becomes 1.

When simulating artificial nucleation. the argument of for the change in diffusivity from that of the vapor to that of a 21 nm particle was based on the distance from the end of the furnace. This distance was described by $x - (L_F + (L_T/2))$. The x is the axial position, L_F is the length of the furnace and L_T is the length of transition zone of interest, which was taken to be 50 mm to conform with the strong temperature gradients at the outlet. The implementation of this transition zone therefore emulates the vapor conversion and particle formation zone at the exit of the furnace (see Figure 3.11)

F. Boundary Conditions for Transport Equations

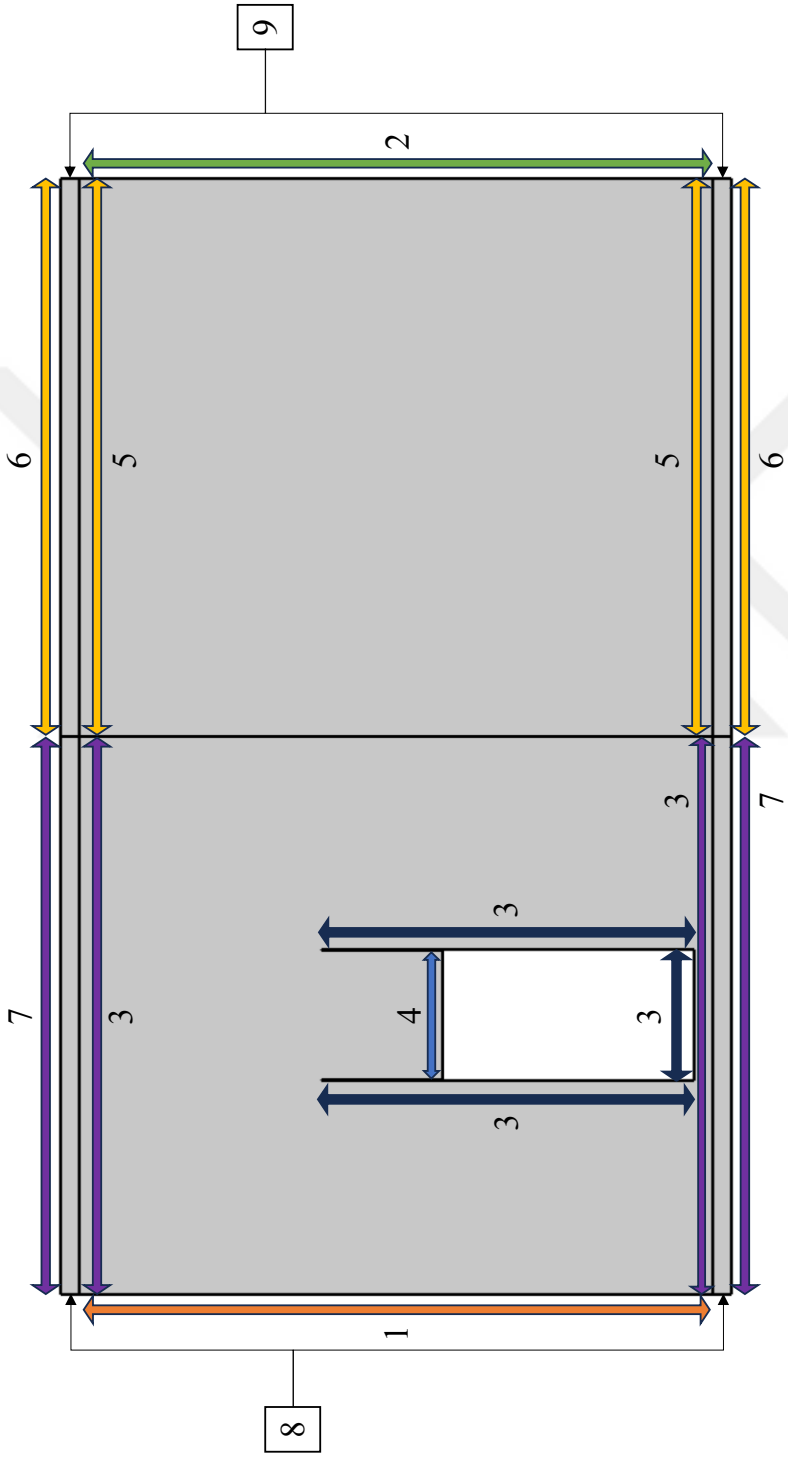

Figure F1. Boundaries of the system. For each physics certain boundary conditions are applied on these boundaries which are state in Table F1

Table F1. Boundary conditions for momentum, heat, and mass transport. Surfaces were shown in Figure F1 and are numerically listed in the second column.

Surface	Boundary #	Momentum Transfer	Heat Transfer	Mass Transfer
Inlet	1	Average inlet velocity*	$T = T_{wall} = 823\ K$	$C_{Sb} = 0$
Outlet	2	$P = 6$ Torr	$-\boldsymbol{n} \cdot \boldsymbol{q} = 0$**	$\boldsymbol{n} \cdot D_i \nabla C_{Sb} = 0$
Furnace and boat walls	3	$\boldsymbol{u} = 0$	$T = T_{wall} = 550$ K	$\boldsymbol{J}_{Sb} = 0$
Solid antimony surface	4	$\boldsymbol{u} = 0$	$T = T_{wall} = 550$ K	$C_{Sb} = P^{vap}/RT$
Interior walls of outlet tube	5	$\boldsymbol{u} = 0$	$T\|_{tube} = T\|_{gas}$*** $[-\boldsymbol{n} \cdot k(dT/dy)]\|_{tube} = [-\boldsymbol{n} \cdot k(dT/dy)]\|_{gas}$	$\boldsymbol{J}_{Sb,wall} = \frac{1}{4}\frac{v_{th}}{RT}\Phi_s(C_{Sb}RT, P^{vap})$ $v_{th} = \sqrt{8k_BT/\pi M n_{Sb}}$
Exterior walls of the outlet tube	6	N/A	$\boldsymbol{q} = h(T_s - T_\infty) + \varepsilon\sigma({T_\infty}^4 - {T_s}^4)$	N/A
Exterior walls of the furnace	7	N/A	$T = T_w = 550$ K	N/A
End of the glass tube - inlet	8	N/A	$T = T_w = 550$ K	N/A
End of the glass tube- outlet	9	N/A	$-\boldsymbol{n} \cdot \boldsymbol{q} = 0$	N/A

*Average velocity is computed from the inlet flow rate, which is input as sccm and then converted to m^3/s in COMSOL with the equation below. The area used for calculation of the average velocity is the internal area of the tube which is $\pi {R_i}^2$.

$$\dot{V} = \dot{V}_{sccm} \cdot \left(\frac{p_{stp}}{p}\right)\left(\frac{T}{T_{stp}}\right)\frac{10^{-3}}{60}$$

** The normal vector $\boldsymbol{n}$ is defined as the vector perpendicular and pointing away from the boundary.

*** These surfaces form an internal boundary, therefore there is temperature equilibrium and flux balance between the two different phases.

G. Mesh Independence and the Numerical Conservation of Mass

The mesh independence analysis was used to determine the effect of size and density of the meshes on the results of a simulation. The CPU required to run a simulation is directly correlated with the size and density of meshes present in the system. Therefore, through this analysis, the aim is to find the minimum number of meshes at which the solution is still reliable and accurate. In this process, various types of meshes were compared against the following criteria: mass flow rate, mass yield and conservation of mass.

The mass flow rate was calculated according to Equation 3.2, mass yield was determined by Equation 3.3 and the conservation of mass is determined via the following equation:

$$\text{Mass Conservation (\%)} = \frac{\text{Outlet flux of Sb} + \text{Wall flux of Sb}}{\text{Sb flux from boat}} \times 100 \qquad \text{(G.1)}$$

Mesh independence was conducted for 500 sccm argon flow rate for three different meshes and an additional simulation for no flux on the walls of the outlet tube of the furnace for comparison. The calculations were done only for the vapor transport (Chapter 3). The results are given in Table H1.

Table G1. Mesh independence and mass conservation data for 500 sccm flow of Ar for vapor transport.

Mesh Type	Number of Meshes	$\dot{m}$ [mg/min]	Y [%]	Mass Conservation [%]
Finer	191 056	0.02	1.05	100
Normal	42 136	0.02	1.04	99.98
Adaptive	342 349	0.02	1.10	100
Adaptive (No flux)	342 349	1.77	100	100

H. Reducing the Particle Diffusion Coefficient to Power-Law Form

In Section 3.4, the diffusion coefficient of particles was described by equations 3.3-3.5 for the whole range of particle Knudsen number ($Kn_p = 2\ell_p/d_p$). The exponential term in the Cunningham slip correction factor makes the use of these equations difficult in a lognormal aerosol model, since it creates a term that depends on the particle size in a relation that is not of power law-type.

$$C_c = 1 + Kn\left[1.257 + 0.4e^{\left(-\frac{1.1}{Kn}\right)}\right] \tag{H.1}$$

To express C_c, hence D_p, the exponential term in C_c can be expanded around zero for the argument of the exponential, that is, very large Kn_p:

$$e^{\left(-\frac{1.1}{Kn}\right)} = 1 - \frac{1.1}{Kn} + \frac{1}{2}\left(\frac{1.1}{Kn}\right)^2 + \cdots \tag{H.2}$$

For Kn_p values larger than 10, surprisingly, all terms but the first can be neglected [89]. Since Kn_p values that appear in this work is much higher, the Stokes-Einstein equation was simplified accordingly. Since the lognormal model was developed for the particle volume, particle diameter was converted to particle volume, and with the simplification of C_c, the Stokes-Einstein equation was reduced to the following power-law form suitable for the lognormal model at large Kn_p:

$$D \cong \frac{k_b T}{3\pi\mu}\left(\frac{1}{d_p} - \frac{3.314 l_p}{{d_p}^2}\right) = \left(\frac{\pi}{162}\right)^{\frac{1}{3}} \frac{k_B T}{\mu}\left(\frac{1}{{v_p}^{\frac{1}{3}}} + \frac{2.671\ell_p}{{v_p}^{\frac{2}{3}}}\right) \tag{H.3}$$